Titre: Title:	Solvent Evaporation-Assisted Three-Dimensional Printing of Piezoelectric Sensors from Polyvinylidene Fluoride and its Nanocomposites
Auteur: Author:	Sampada Bodkhe
Date:	2017
Type:	Mémoire ou thèse / Dissertation or Thesis
Référence: Citation:	Bodkhe, S. (2017). Solvent Evaporation-Assisted Three-Dimensional Printing of Piezoelectric Sensors from Polyvinylidene Fluoride and its Nanocomposites [Thèse de doctorat, École Polytechnique de Montréal]. PolyPublie. https://publications.polymtl.ca/2855/

URL de PolyPublie: PolyPublie URL:	https://publications.polymtl.ca/2855/
Directeurs de recherche: Advisors:	Daniel Therriault, & Frederick Gosselin
Programme: Program:	Génie mécanique

UNIVERSITÉ DE MONTRÉAL

SOLVENT EVAPORATION-ASSISTED THREE-DIMENSIONAL PRINTING OF PIEZOELECTRIC SENSORS FROM POLYVINYLIDENE FLUORIDE AND ITS NANOCOMPOSITES

SAMPADA BODKHE
DÉPARTEMENT DE GÉNIE MÉCANIQUE
ÉCOLE POLYTECHNIQUE DE MONTRÉAL

THÈSE PRÉSENTÉE EN VUE DE L’OBTENTION
DU DIPLÔME DE PHILOSOPIAE DOCTOR
(GÉNIE MÉCANIQUE)
DÉCEMBRE 2017

UNIVERSITÉ DE MONTRÉAL

ÉCOLE POLYTECHNIQUE DE MONTRÉAL

Cette thèse intitulée :

SOLVENT EVAPORATION-ASSISTED THREE-DIMENSIONAL PRINTING OF PIEZOELECTRIC SENSORS FROM POLYVINYLIDENE FLUORIDE AND ITS NANOCOMPOSITES

présentée par : BODKHE Sampada

en vue de l'obtention du diplôme de : Philosophiae Doctor

a été dûment acceptée par le jury d'examen constitué de :

M. ACHICHE Sofiane, Ph. D., président

M. THERRIUALT Daniel, Ph. D., membre et directeur de recherche

M. GOSSELIN Frédérick, Doctorat, membre et codirecteur de recherche

M. AJJI Abdellah, Ph. D., membre

M. VENGALLATORE Srikar, Ph. D., membre externe

DEDICATION

To everyone who motivated me to do this PhD.

ACKNOWLEDGEMENTS

My over four years of stay in Montreal during this Ph.D. have been a wonderful experience. I am indebted to my supervisors Prof. Daniel Therriault and Prof. Frederick Gosselin for accepting me as their student and for giving me an opportunity to work in the area of three-dimensional printing of smart systems. I have gained a lot of skills from them on technical, presentation, and management fronts. I am thankful to them for providing me with continuous appreciation, motivation and encouragement.

I would like to use this platform to express my gratitude to Dr. P.S.M. Rajesh who has been my colleague and best friend during the last few years. It has been a pleasure learning from and working with Dr. Rouhollah Farahani, Maxime Arguin, Nicolas Guerin, and Renaud Passieux. I would like to thank my collegues Kambiz Chizari, Xavier Cauchy, Ilyass Tabiai, Qinghua Wu, Yahya Abderaffai, Shibo Zou, Rui Tao and Hongqiu Wei. I thank Brijpal Singh Talwar, Aparajita, Mounika for providing all the necessary help during my first few days in this new country.

I acknowledge the help and assistance from Isabelle Nowlan, Benedict Besner, and Nour Aimene. I take this opportunity to thank the Meca support team at Polytechnique for their relentless help with software installations and other technical support. I am grateful to Lucile Moret, Nicolas Jayabhadran and Prof. Sirois from the laboratory of electrical energy for providing me with guidance on electrical side of my thesis and access to their laboratory; Prof. Annie Ross, Jean-Michel Attendu, Dr. Elsa Piollet, from the laboratory of acoustics and vibrations; Laurent Mouden, Dr. Bahareh Ghane-Motlagh, Prof. Sawan; Lucie Riffard, Adam Smith and Prof. Pascal Hubert from the laboratory of structures and composite materials at McGill university; Dr. Ramin Yousefzadeh Tabasi, Dr. HeliaSojoudi and Prof. Marie-Claude Heuzey for help with DSC and rheology; Nicolas Leduc-Savard and Prof. Tremblay from the department of Kinesiology at University of Montreal; and Dr. Marc-Etienne Lamarche and Prof. Jerome Vetel for allowing me the access to their laboratory and equipment. I thank my co-authors and undergraduate interns Gabrielle Turcot, Clara Noonan, and intern Sarah O'Rourke. I thank Nusrat Jahan for all the interesting discussions on piezoelectric materials.

I thank Prof. Therriault and Prof. Robert Shepherd for providing the opportunity to work at organic robotics laboratory at Cornell University during the spring of 2016. It was a pleasure working with Thomas Wallin and all the other colleagues at Cornell.

I shall also not forget the happy times I spent with my friends: Leticia, Kim, Sanaz, Mauricio, Celso, Isabel, Sandra, Thomas, Jesus, Adya, Sanchari, Emily, Nirmal, and their support during the bad times. Further, I am grateful to my brother, my parents, all my friends and my teachers for making me what I am today.

Sincerely,
Sampada

RÉSUMÉ

Les matériaux piézoélectriques sont connus pour générer des charges électriques lors de leur déformation. Leur capacité à transformer linéairement l'énergie mécanique en énergie électrique, et vice versa, est utilisée dans la détection, l'actionnement, la récupération et le stockage d'énergie. Ces appareils trouvent des applications dans les domaines de l'aérospatiale, de la biomédecine, des systèmes micro-électromécaniques, de la robotique et des sports, pour n'en nommer que quelques-uns. On retrouve la propriété de piézoélectricité dans certaines céramiques, roches, monocristaux et quelques polymères. Le poly(fluorure de vinylidène) (PVDF) est un polymère piézoélectrique qui présente un coefficient piézoélectrique très élevé par rapport aux céramiques, ce qui laisse présager des applications de détection et de récupération d'énergie. La facilité de fabrication, la flexibilité et la biocompatibilité du PVDF sont autant de qualité qui en font un très bon candidat pour ces applications. Les dispositifs actuels à base de PVDF commercial sont disponibles en films plats ou en fibres unidimensionnelles (1D). L'impression tridimensionnelle (3D) du PVDF peut amener à des sensibilités, souplesses et capacités de fabrication accrues des capteurs embarqués en cas d'impression multi-matériaux.

Le PVDF est un polymère semi-cristallin possédant cinq polymorphes, dont la phase β polaire qui présente les meilleures propriétés piézoélectriques. Malheureusement, le PVDF, provenant de la fusion ou de la dissolution, cristallise en une phase α non polaire thermodynamiquement stable. Diverses transformations physiques telles que le recuit, l'addition de charge, l'étirement ou le polissage sont effectuées pour transformer la phase α en phase β. En raison de la cristallisation inhérente du PVDF dans la phase α, il y a eu très peu de tentatives de fabrication de structures 3D à partir du PVDF. L'électrofilage en champ proche et la Déposition de Filament Fondu ont permis de fabriquer certaines structures 3D couche par couche avec du PVDF, soit avec l'application de hautes tensions électriques, soit avec la fusion à haute température du polymère. Et les deux nécessitent un traitement de polarisation pour conférer la piézoélectricité aux structures imprimés. Pour fabriquer des capteurs incorporés ou conformes, sur des substrats donnés, il est essentiel de ne pas avoir d'effets négatifs sur les matériaux adjacents à cause de la polarisation pendant le processus d'impression. Ainsi, dans ce travail, nous avons développé un procédé d'impression 3D qui crée des structures PVDF principalement en phase β, à température ambiante et sans application de tension de polarisation.

L'impression 3D assistée par évaporation de solvant a été utilisée pour imprimer des structures piézoélectriques à base de PVDF. Dans ce procédé, la solution de polymère est introduite dans une seringue qui est insérée dans un distributeur pneumatique. Le distributeur pneumatique est monté sur un bras robotisé commandé par un programme informatique. Le dessin à imprimer est introduit dans le programme d'ordinateur sous la forme d'une série de coordonnées cartésiennes. Le bras robotisé se déplace dans les directions x, y et z afin d'imprimer la forme désirée sur une plate-forme.

L'extrusion de la solution de PVDF à des pressions de l'ordre de 1 MPa contribue à convertir la phase α en en phase β. Pour accroître encore l'efficacité de cette conversion et la conserver des nanoparticules de titanate de baryum ($BaTiO_3$ NP) ont été ajoutées au PVDF. Trois méthodes de mélange différentes ont été étudiées afin d'incorporer les NP dans la matrice PVDF: broyage à billes, extrusion en phase fondue et ultrasonication. Après un ensemble de tests piézoélectriques, de spectroscopie d'impédance, de microscopie électronique à balayage, de diffraction à rayons X et de spectroscopie infrarouge à transformée de Fourier, on a conclu que le broyage par billes était la méthode la plus efficace pour améliorer le contenu de la phase piézoélectrique. La concentration optimale des NP pour atteindre ces propriétés piézoélectriques élevées a été trouvée à 10 wt.%. Pendant le processus de solidification, des agglomérats submicroscopique uniformément distribués des NP ont aidé à retenir la phase β créée pendant l'extrusion. Les films fabriqués en utilisant cette formulation ont donné un coefficient piézoélectrique de 18 pC N^{-1}, qui est comparable aux films PVDF commerciaux post-traités par étirage et polarisation. Des structures tridimensionnelles (e.g., cylindres, échafaudages) ont été fabriqués pour démontrer la capacité d'imprimer en 3D des composites du PVDF. Un capteur de contact 3D est présenté en tant qu'application du processus.

La création d'électrodes sur les surfaces inaccessibles est la principale contrainte pour imprimer des capteurs complexes. Pour surmonter cette limitation, un nouveau procédé, a été développé pour co-extruder du PVDF avec une peinture d'argent. Le paramètre le plus important pour la réussite du processus était d'atteindre des propriétés rhéologiques similaires dans les deux solutions. Lorsque les filaments co-extrudés sont cousus dans des tissus comme des gants, des supports de coude et de genou, etc., les filaments piézoélectriques aident à détecter les mouvements corporels. Ces tissus intelligents auto-alimentés pourraient éventuellement remplacer les capteurs passifs nécessitant une alimentation externe actuellement auss : utilisés dans les industries du sport et de la biomédecine. Le même processus est utilisé pour imprimer des capteurs 3D munis d'électrodes. L'impression 3D de ce composite co-extrudé est appliqué à la surveillance aérodynamique d'ailes battantes.

Pour étudier l'effet de la polarisation sur les capteurs imprimés en 3D, une technique a été développée pour polariser les structures simultanément en cours d'impression. Des champs électriques externes ont été appliqués entre la buse d'impression et un substrat métallique pendant le processus d'impression. La diffraction des rayons X, la spectroscopie infrarouge à transformée de Fourier et les essais effectués pour mesurer les charges générées ont déterminé que le champ électrique de polarisation le plus efficace était 1 MV m^{-1}.

Ainsi, la technique de fabrication développée peut être utilisée pour fabriquer en une seule étape des capteurs piézoélectriques 3D, incorporés dans la structure et de géométries complexes et prêts à l'emploi. Cela permet l'expansion des techniques d'impression 3D à la fabrication de dispositifs multi-composants et multifonctionnels entièrement fonctionnels en une seule étape.

ABSTRACT

Piezoelectric materials are known to generate electric charges upon deformation. Their ability to linearly transform mechanical energy into electrical energy and vice versa, is utilized in sensing, actuation, transducing, energy harvesting and storage. These devices find applications in aerospace, biomedicine, micro electromechanical systems, robotics and sports, to name a few. Piezoelectricity is found in some ceramics, rocks, single crystals and a few polymers. Polyvinylidene fluoride (PVDF) is a piezoelectric polymer that exhibits a very high piezoelectric stress coefficient as compared to the ceramics, making it the forerunner for sensing and energy harvesting applications. PVDF's formability, flexibility and biocompatibility, further reinforce its candidature. Present commercial PVDF-based devices come in flat films or one-dimensional (1D) fibers. Three-dimensional (3D) printing of PVDF leads to higher sensitivity, better compliance, and ability to print embedded sensors in case of multi-material printing.

PVDF is a semi-crystalline polymer possessing five polymorphs, of which the polar β-phase exhibits highest piezoelectric properties. Unfortunately, PVDF from melt or solution crystallizes into a thermodynamically stable non-polar α-phase. Various physical transformations like annealing, filler addition, stretching or poling are carried out to transform the α-phase into β-phase. Due to the inherent crystallization of PVDF into α-phase, there have been very few attempts in fabricating 3D structures from PVDF. Near-field electrospinning and fused deposition modelling have demonstrated some layer-by-layer 3D structures with PVDF, either with application of high electric voltages or high temperature melting of the polymer, respectively. Also, both these techniques require a poling treatment to impart the desired piezoelectricity to the printed features. To fabricate embedded or conformal sensors on given substrates, it is essential to not have any adverse effects on the adjacent or substrate materials due to poling during the printing process. Thus, in this work, we develop a 3D printing process, that creates PVDF structures that inherently crystallize in the piezoelectric oriented β-phase at room temperature without any applied voltages.

Solvent-evaporation assisted 3D printing is employed to print 3D piezoelectric structures of PVDF based solutions. In this process, the polymer solution is filled into a syringe which is inserted into a pneumatic dispenser. The pneumatic dispenser is mounted on a robotic arm that is controlled via a computer program. The design to be printed is fed into the computer program in

the form of a series of Cartesian coordinates. The robotic arm moves in the x, y and z-directions over a platform to fabricate the desired shape.

We demonstrate the ability to convert α-phase into the β-phase via extrusion of the PVDF solution at pressures around 1 MPa. To further increase the efficiency of this conversion and retain the hence realized β-phase, barium titanate nanoparticles ($BaTiO_3$ NPs) are added to PVDF. Three different mixing methods are studied in order to incorporate the NPs into the PVDF matrix: ball-milling, extrusion and sonication. After a set of piezoelectric tests, impedance spectroscopy, scanning electron microscopy, X-ray diffraction and Fourier transform infrared spectroscopy, it is concluded that ball-milling is the most efficient method to improve the content of the piezoelectric phase. The optimum concentration of the NPs to achieve these high piezoelectric properties is found to be 10 wt. % in PVDF. During the solidification process, uniformly distributed sub-micrometer sized agglomerates of the NPs aid in retaining the β-phase created during extrusion. The films fabricated using this formulation result in a piezoelectric coefficient of 18 pC N^{-1}, which is comparable to the commercial PVDF films post-processed via stretching and poling. 3D structures: cylinders, scaffolds etc. are fabricated to establish the ability to 3D print PVDF-based solutions. A 3D contact sensor is shown as an application of the process.

To study the effect of poling on the 3D printed sensors, a technique is developed to pole the structures simultaneously while being printed. External electric fields are applied between the printing nozzle and a metallic substrate during the printing process. X-ray diffraction, Fourier transform infrared spectroscopy and indigenously designed tests to measure the generated charges determine the most effective poling electrical field to be 1 MV m^{-1}.

Further, the major constraint to 3D print complex sensors is creating electrodes on the non-reachable surfaces. To overcome this limitation, a new process, is developed to coextrude PVDF with a silver paint. The most important aspect for this process is to attain similar rheological properties in the two solutions. Coextruded filaments could then be wound in the form of a spool. When sewed into fabrics like gloves, elbow and knee supports etc., the piezoelectric filaments help in sensing the bodily movements. These self-powered smart fabrics could eventually replace the externally powered passive sensors presently used in the sports and biomedical industries. The same process is used to 3D print sensors with simultaneously formed electrodes. 3D printing of this co-extruded ink is further applied in aero-elastic monitoring of flapping wings.

Thus, the newly developed fabrication technique can be used to fabricate conformal, embedded and complex shaped ready-to-use 3D piezoelectric sensors in a single step. This gives way to the expansion of 3D printing techniques beyond just prototypes or structural components to the fabrication of fully functional multi-component, multi-functional devices in a single step.

TABLE OF CONTENTS

LIST OF TABLES

LIST OF FIGURES

LIST OF SYMBOLS AND ABBREVIATIONS

3D	three-dimensional
$BaTiO_3$	barium titanate
DMA	dynamic mechanical analyzer
DMF	dimethyl formamide
DMSO	dimethyl sulfoxide
DMSO	dimethyl sulfoxide
DMSO	dimethyl sulfoxide
DPN	dip-pen lithography
FDM	fused deposition modelling
FTIR	fourier transform infrared spectroscopy
PLA	polylactic acid
PVDF	polyvinylidene fluoride
PZT	lead zirconium titanate
NC	nanocomposite
NFP	fountain pen nanolithography
NP	nanoparticle
SEM	scanning electron microscopy
SHM	structural health monitoring
SLA	stereolithography
XRD	x-ray diffraction
A_α	absorptions fraction of α-phase
A_β	absorptions fraction of β-phase
A	area (m^2)
C	capacitance (F)
D	polarization($C\ m^{-2}$)
d	direct piezoelectric ($pC\ N^{-1}$)
E	electric field ($V\ m^{-1}$)
F_β	fraction of β-phase
g	indirect piezoelectric coefficient ($m\ V^{-1}$)
Q	charge (C)

S	strain
T	stress (N m^{-2})
V	voltage (V)
α	alpha
β	beta
γ	shear rate (s^{-1})
ε^T	dielectric permittivity
ε_r	relative dielectric permittivity
ε_0	dielectric permittivity of free space (8.854 × 10^{-12} F/m)
η	viscosity (Pa s)
τ	shear stress (Pa)
v	velocity (m s^{-1})

CHAPTER 1 INTRODUCTION

Three-dimensional (3D) printing is the process of creating structures in a layer-by-layer fashion. As opposed to conventional fabrication methods of material removal (e.g., machining, laser ablation), the additive technology is based on a bottom-up approach enabling the creation of complex shapes required by most of today's technological applications. This fabrication approach offers huge potential for the production of intricate multifunctional (catering to several functions) 3D structures for the mechanical and aerospace industry and miniaturization of mechanical systems for the microelectronics industry. One of the 3D printing techniques, direct-writing (DW), involves controlled extrusion using a pneumatic dispensing system attached to a robotic arm capable of motion in x-, y- and z-directions to form 3D structures. Protocols have already been developed for organic inks [1], colloidal gels, UV curable gels [2] and thermoplastic solutions [3].

Solvent evaporation-assisted 3D printing [3], one of the direct-write technique, comes in with the advantages of fabricating structures from polymer solutions at room temperature. This technique has proven successful in 3D printing self-supporting and freeform structures of not only polymers but also their functional nanocomposites.

The polymer, polyvinylidene fluoride (PVDF) is well known for its inherent pyro, piezo and ferroelectric properties. It scores over other conventional ceramic piezoelectrics by possessing low density, ease of fabrication, good thermal conductivity and high electromechanical coupling with low dielectric constant. PVDF is used in various microelectronic applications like sensors [5], actuators [4] and transducers. Its biocompatibility and chemical inertness has made it a major contributor in tissue engineering and biomedical applications [1]. Engineers are further researching to produce self-powered devices with PVDF for lab-on-chip technology [2, 3].

Solvent evaporation-assisted 3D printing to fabricate piezoelectric devices using PVDF is proposed. Unlike polylactic acid (PLA), the low stiffness of PVDF poses difficulties in obtaining very small rigid self-supporting and freestanding features. The major challenge in this work is to attain high piezoelectric properties in the 3D printed PVDF and co-fabricate the electrodes, which usually requires cumbersome post processing. A detailed study of the printing parameters and their effect on the properties of PVDF and rigorous effort towards the development of an advanced process to print 3D structures of PVDF nanocomposites with high piezoelectric properties is carried out. The 3D printed piezoelectric structures may find applications as motion and pressure sensors and other energy harvesting devices in the sports, medicine, military, robotics and electronic applications.

Organization of the thesis

This is an article-based thesis consisting of three articles submitted to scientific journals.

Chapter 2 provides a literature review on piezoelectric materials, their applications and state of 3D printing techniques used to fabricate piezoelectric materials. The properties, characterization and present fabrication techniques used for the polymer under study: PVDF, are discussed in brief. The chapter also discusses the potential applications in wearable electronics and structural health monitoring. The core results of the work in the form of three articles, submitted to scientific journals are presented in Chapter 3 that enlists the research objectives and gives a brief description on the coherence of the articles. Chapter 4 focusses on developing a highly piezoelectric ink to be used for printing piezoelectric structures in 3D. Various material system and nanocomposite fabrication techniques are used to finally attain a piezoelectric material with properties comparable to that of commercially available PVDF based films. A working 3D sensor is also demonstrated for the first time. Chapter 5 includes the study of the effect of electric field on the piezoelectric properties of PVDF and its nanocomposite with barium titanate. Chapter 6 reports the fabrication of one-step sensors: piezoelectric material coextruded with silver electrodes. The limitation of forming electrodes on a complex shaped 3D piezoelectric structure are overcome by printing the piezoelectric material sandwiched between two electrodes. Application of this technique in the form of piezoelectric thread for smart textiles are demonstrated in the form of knee movement and breathing sensors, and 3D printed sensors for aero-elastic monitoring. Chapter 7 provides a general discussion and the big-picture of the entire thesis with the current state-of-the-art. Chapter 8 summarizes the conclusions of the work.

CHAPTER 2 LITERATURE REVIEW

2.1 Piezoelectricity theory

Piezoelectricity was discovered by Curie brothers in 1880 as a property of crystalline materials to develop electric charges upon application of mechanical stress [4]. The converse (indirect piezoelectricity) of this phenomenon that such materials exhibit mechanical deformation or strain on application of an electric field was also realized. Piezoelectricity was first observed in natural crystals like quartz and tourmaline and then in Rochelle salt. Bone, silk, enamel and wood are amongst some biological piezoelectric materials. Later, improved piezoelectricity was found in ceramics like barium titanate ($BaTiO_3$) and lead zirconium titanate (PZT) upon electrical poling. Poling, as shown in Figure 2.1(a), is the process of permanently aligning electric dipoles within a material with the application of high electric fields at elevated temperatures. Prior to poling these dipoles (the cause of piezoelectricity) are randomly scattered within the crystals of the material. Poling results in the generation of net polarization, also known as dipole moment, D in the crystal. Kawai et al. [5] found that polyvinylidene fluoride (PVDF) had highest piezoelectric constants as compared to other polymers. Piezoelectric materials are also known to possess ferroelectric and pyroelectric properties. Ferroelectricity is the ability of a material to be spontaneously polarized on the application of an electric field. This polarization can be reversed upon reversing the field. Pyroelectricity, like piezoelectricity, refers to the ability of the material to produce electric charges upon heating.

Direct piezoelectric effect: The application of compressive stresses T on a piezoelectric block creates a distribution of charges in the block (Figure 2.1(c)). This generates a polarization D, resulting in an electric potential E across the circuit. Various piezoelectric sensors and energy harvesters employ the direct piezoelectric effect. Any small mechanical deformation or strain in the material gives rise to electrical charges which could either be used to quantify the strain (sensing) or stored (power harvesting) in the form of electrical energy. The charges produced by piezoelectric materials are very low in magnitude and require amplification. Owing to high output impedance of piezoelectric materials, standard multimeters or oscilloscopes cannot be used to study the electrical output and thus require specialized high input impedance amplifiers. Also, these devices cannot be used for static measurements because the response of a piezoelectric material constitutes a fixed amount of charges which drain out due to imperfect insulation leading to continuous loss of electrons. Sensitivity of a piezoelectric device is calculated as the ratio of output voltage V to applied mechanical stress T.

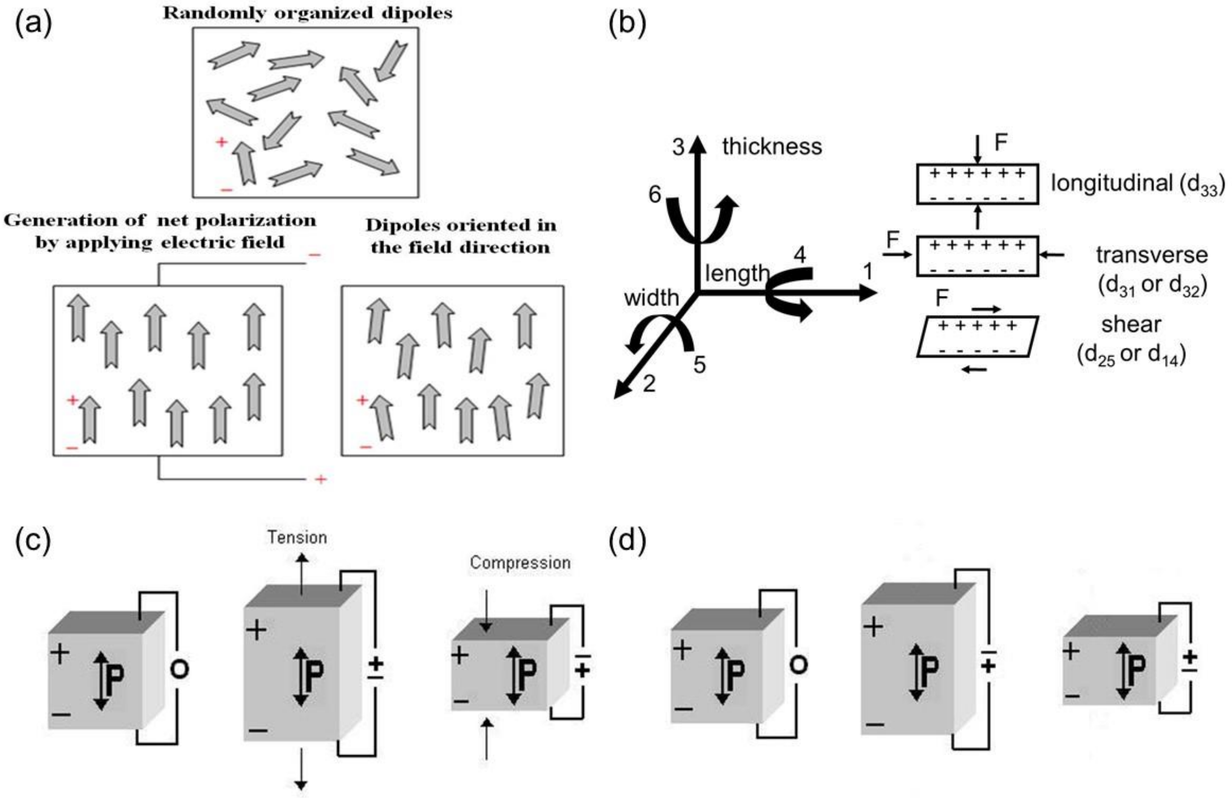

Figure 2.1: (a) Dipole orientation [3]; (b) Piezoelectric constants associated with different deformations; (c) Direct piezoelectric effect; (d) Indirect piezoelectric effect [6]

Indirect (converse) piezoelectric effect: Indirect piezoelectric effect (Figure 2.1 (d)) occurs when an electric field E is applied across the piezoelectric block, the block undergoes mechanical deformation (stretching or compression) resulting in change of shape. The converse piezoelectric effect is utilized in actuation. The strain in piezoelectric devices is usually very small, limited to few tenths of a percentage, thus requiring very high driving [6].

As per the IEEE standard 1987 on piezoelectricity, major constitutive relationships for piezoelectric materials are as follows [7, 8]:

In the direct piezoelectric effect, the electric displacement or polarization, D (C m^{-2}) produced upon application of a stress T(N m^{-2}) can be calculated as:

$$D = \in^{T} E + \boldsymbol{d}\, T \tag{1}$$

where $\in^{T}$ is the dielectric permittivity of the material at constant stress T, E is the electric field (V m^{-1}) produced due to the strain and d is the direct piezoelectric coefficient matrix. The same can be written in expanded notation as below:

$$\begin{bmatrix} D_1 \\ D_2 \\ D_3 \end{bmatrix} = \begin{bmatrix} \varepsilon^{T}{}_{11} & \varepsilon^{T}{}_{12} & \varepsilon^{T}{}_{13} \\ \varepsilon^{T}{}_{21} & \varepsilon^{T}{}_{22} & \varepsilon^{T}{}_{23} \\ \varepsilon^{T}{}_{31} & \varepsilon^{T}{}_{32} & \varepsilon^{T}{}_{33} \end{bmatrix} \begin{bmatrix} E_1 \\ E_2 \\ E_3 \end{bmatrix} + \begin{bmatrix} \mathbf{d_{11}} & \mathbf{d_{12}} & \mathbf{d_{13}} & \mathbf{d_{14}} & \mathbf{d_{15}} & \mathbf{d_{16}} \\ \mathbf{d_{21}} & \mathbf{d_{22}} & \mathbf{d_{23}} & \mathbf{d_{24}} & \mathbf{d_{25}} & \mathbf{d_{26}} \\ \mathbf{d_{31}} & \mathbf{d_{32}} & \mathbf{d_{33}} & \mathbf{d_{34}} & \mathbf{d_{35}} & \mathbf{d_{36}} \end{bmatrix} \begin{bmatrix} \mathbf{T_1} \\ \mathbf{T_2} \\ \mathbf{T_3} \\ \mathbf{T_4} \\ \mathbf{T_5} \\ \mathbf{T_6} \end{bmatrix} \tag{2.1}$$

In indirect piezoelectric effect, the strain S produced on application of polarization D is given by:

$$S = \boldsymbol{s}^{D} \mathrm{T} + \mathrm{g\,D} \tag{2.2}$$

where g is the indirect piezoelectric coefficient matrix (m V^{-1}) and s is the elastic compliance matrix (m^2 N^{-1}). The direct and indirect piezoelectric coefficients d and g are related as:

$$\boldsymbol{d}_{ij} = \in_{r} \in_{0} \boldsymbol{g}_{ij} \tag{2.3}$$

where $\in_{r}$ and $\in_{0}$ (8.854×10^{-12} F/m) are the relative dielectric permittivity of the material and dielectric permittivity of free space, respectively, and i and j are the direction of generation of polarization and direction of application of stress, respectively. Equation 2.1 describes the piezoelectric constants d_{ij} associated with different types of deformations. The stress and strain are 6 × 1 vectors (s is a 6 × 6 compliance matrix) while electric field and polarization are 3 × 1 vectors, hence, d_{ij} and g_{ij} are 3 × 6 matrices.

2.1.1 Comparison of various piezoelectric materials

Table 2.1 compares the properties of common piezoelectric materials: conventional ceramics (PZT and $BaTiO_3$), quartz crystal and the piezoelectric polymer PVDF. The d_{31} constant for PVDF is lower as compared to PZT and $BaTiO_3$ but the electromechanical coupling constant g_{31}

is much higher for PVDF. High g_{31} along with a very low acoustic impedance result in a very quick response time for PVDF compared to the conventional piezoelectric ceramic.

Table 2-1: Comparison of properties of PVDF and piezoelectric ceramics [7-9]

Properties	**PZT**	**$BaTiO_3$**	**Quartz crystal**	**PVDF**
Density (kg m^{-3})	7500	5700	2650	1780
Relative Permittivity ($\in_r$)	1200	1700	4.5	12
d_{31} constant (pC N^{-1})	110	78	2.3-4.6	23
g_{31} constant (mV m N^{-1})	10	5	18.2	216
Acoustic impedance (kg/m^2s)	30×10^6	30×10^6		2.7×10^6
Young's Modulus (N m^{-2})	$49 - 63 \times 10^9$	67×10^9	$0.07\text{-}0.1 \times 10^6$	2×10^9
Specific stiffness (N m kg^{-1})	$\sim 7.3 \times 10^6$	12×10^6	32	1.1×10^6

Also, PVDF's lower values of Young's modulus and density are added advantages for the fabrication of flexible and light structures.

2.2 Polyvinylidene fluoride (PVDF)

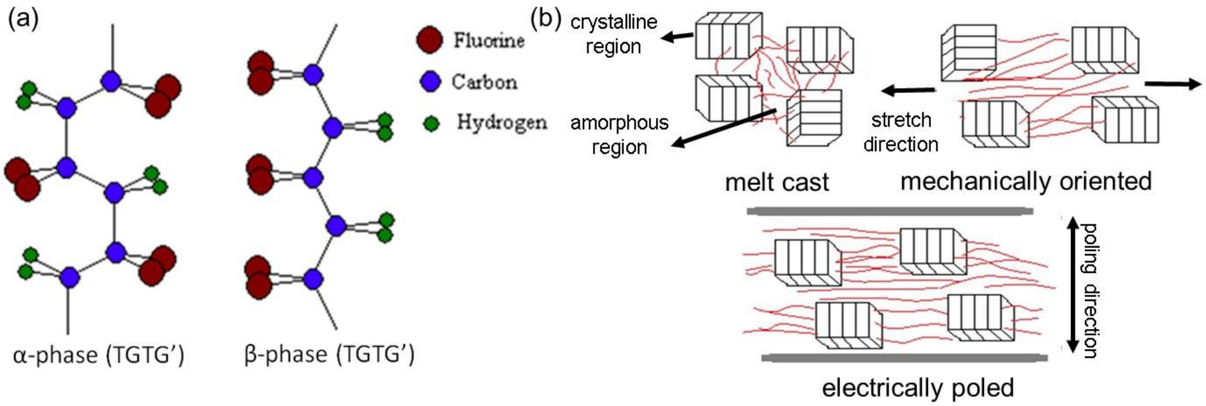

Figure 2.2: (a) Chemical structure of the 2 main forms of PVDF [18]; (b) Orientation of semi- crystalline PVDF by stretching and poling [3]

PVDF, a semi crystalline fluoropolymer, consists of five crystalline polymorphs (also known as phases or crystal structures) – α, β, ϒ, δ and ε as discovered by Lando et al. in 1968 [9]. Chemically, PVDF consists of polymer chains of repeating CF_2-CH_2 units. The arrangement of the fluorine and hydrogen atoms about the C-C backbone defines the phase of PVDF. The α and δ polymorph consists of a trans-gauche (TGTG') configuration, the β is found in an all trans (TTTT) planar zig-zag form [10] and ϒ and ε phases have T3GT3G' conformation. Figure 2.2(a) shows the chemical structures of α and β polymorphs of PVDF. The presence of fluorine atoms on one side and the hydrogen atoms on the other side generates a net dipole moment in the β-polymer chain. This dipole moment is exploited to attain higher pyro and piezoelectric properties. Except the α-phase, which commonly crystallizes upon solidification, all other phases are unstable in nature. These unstable phases, especially β-phase are fundamental for pyro, piezo and ferroelectric properties of PVDF. Kawai had discovered highest post-poling piezoelectric constant values (g_{31} = 150 mV m N^{-1}) for PVDF amongst similar polymers like polyvinyl fluoride, polyvinyl chloride [5] etc. The β and ϒ phases impart high dipole moment (7.58×10^{-28} C cm) [11], specific dielectric constant (10^{-10} cm^{-1}) and polarization (131 mC m^{-2}) to PVDF. The attainment of these phases requires a physical transformation and its retention (Figure 2.2(b)). Upon solidification the crystalline and amorphous phases of PVDF are randomly intermixed. Stretching helps in orienting the dipoles (formation of β-phase) and poling further imparts a permanent orientation of the crystalline dipoles in PVDF in the required directions. Application of high electric fields for long duration has proved highly effective in the formation of β and ϒ phases [11, 12]. Annealing [13], electrospinning [14, 15], and stretching [16] have also shown promising results in improving β and ϒ phases.

2.2.1 Fabrication techniques used for PVDF

PVDF has been used in the forms of films in most of its applications exploiting the d_{31} constant. Hence, most conventional film fabrication techniques like solution casting, spin coating, electrospinning, extrusion, immersion precipitation have been well studied and developed over the years. Fibers and 3D features of PVDF are the results of recent advances in the manufacturing sector. The advances include both modified versions of the classical techniques like near-field electrospinning and electric poling assisted additive manufacturing as well as novel lithography and ink-jet printing. Choice of a fabrication technique equally depends on the application and the characteristic properties of the final product. As some techniques are common to one or more fields, instead of classifying them according to 1D, 2D and 3D manufacturing techniques, only the techniques relevant to this work are explained in detail.

Extrusion

Extrusion produces PVDF fibers as well as films directly from molten PVDF, hence, can be considered to be both 1D and 2D fabrication technique for PVDF. PVDF powder or pellets are filled into the extruder and heated between 190-220 °C (Figure 2.3(a)). Drawing of PVDF at specific temperatures and draw rates transforms the crystallites from α to β form [17]. The ultrahigh shear induced processing in the extruder is the driving force behind this conversion. Fillers in powdered form can be directly mixed in PVDF before feeding into the extruder [18-21]. The temperature of extrusion and the speed of rotation of the screws have significant impact on the size and morphology of the extruded PVDF. The extruder can be roll mill type (forming films) [22] or a compact screw type (forming fibers) [19].

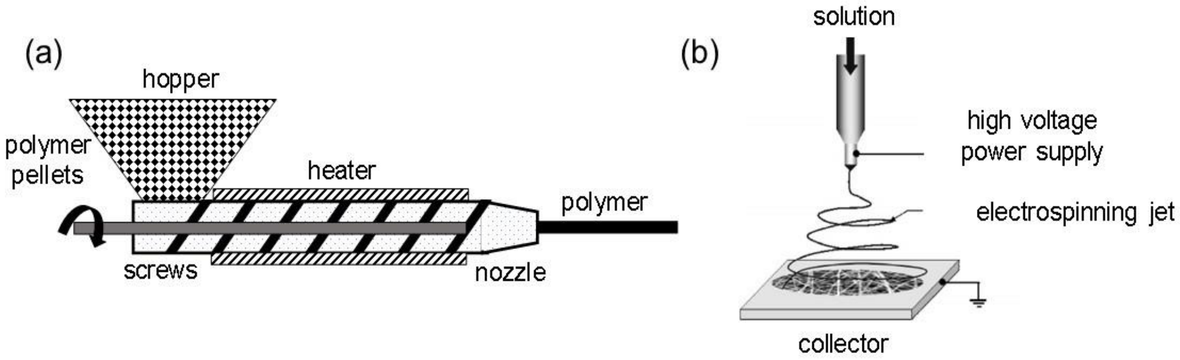

Figure 2.3: (a) Schematic of general screw-type extrusion process; (b) Schematic of electrospinning process with flat plate collector [25]

Electrospinning

Electrospinning was invented by Formhals in 1934 [23] and is used to produce both 1D fibers, 2D mats and membranes. Electrospinning is a process of fabrication of charged fibers of a polymer directly from the polymer melt or its solution. In this process of combined mechanical stretching as well as electrical poling, a low to medium viscosity PVDF solution is ejected through a charged syringe with a metal tip onto a grounded collector (Figure 2.3(b)) [24]. The collector can be a stationary, revolving or rotating – drum [25] or plate [26]; metal [14] or covered with aluminium foil [27]. PVDF droplets coming out from the syringe orifice form a

Taylor's cone is formed due to surface tension and the electrostatic attraction from the increasing voltage on the charged collector [28]. The electrostatic repulsion between the surface charges on dimethyl acetamide [25, 29] with acetone or other anti-solvents to aid faster evaporation.

the polymer jet results in the formation of continuous ultrathin fibers as the voltage overcomes the surface tension barrier. This voltage is termed "critical voltage". On their way to the collector, which is usually about 15-25 cm away from the syringe tip, the fibres solidify due to rapid solvent evaporation. The potential difference across the syringe tip and the collector is between 5-20 kV. The fiber diameter and the content of β-phase predominantly depend on PVDF concentration, feed rate of the polymer solution, distance and potential difference between the

syringe outlet and the collector, speed of the collector and the rate of evaporation of the solvent [30]. PVDF is dissolved in the solvents with a usual concentration of 15-20% weight by volume for spinability [31]. The solvents frequently used are N,N-dimethyl formamide (DMF) [29], N,N-

Near field electrospinning

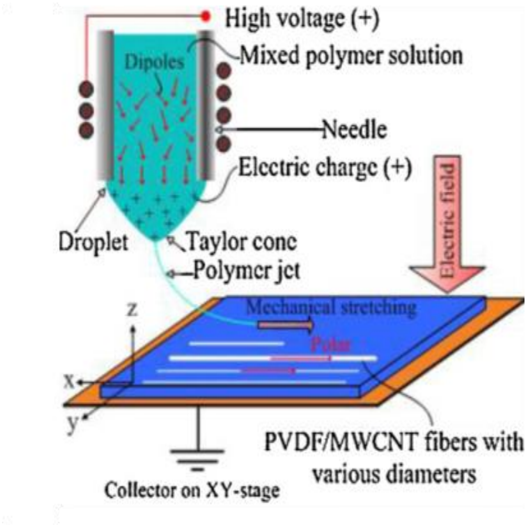

Figure 2.4: Schematic of NFES [35]

Near field electrospinning (NFES) is a modification over conventional electrospinning process (Figure 2.4). The name "near field electrospinning" comes from the reduction in the distance between the needle and the collector to obtain control over the orientation of the fibers. Here, the application of an additional electrode as collector facilitates unidirectional fiber fabrication. The oppositely charged collector electrodes result in the deposition of the fibers with oriented dipoles. These fibers find direct applications in piezoelectric actuators.

This technique developed in Lin's laboratory [32] was used by Pu et al. to successfully fabricate PVDF fibers with 2.6 µm diameter and 500 µm length for piezoelectric actuation [6]. They also obtained a high piezoelectric constant (d_{33}) of -57.3 pC/N. They reported that the fiber diameter decreased upon increasing the collector stage moving speed. Further, Liu et al. [33], considered the effect of adding multi-walled carbon nanotubes (MWCNT) (0.01, 0.03 and 0.05 wt.%) on the mechanical strength and piezoelectric properties of electrospun nanofibers. They could alter the intensity of polarization in the fibers through modification of the various process parameters. While the diameter of the fibers increased with increasing needle diameter and electric field, the diameter was found to reduce to about 8.5 µm with 0.05 wt.% MWCNT addition as compared to 12.5 µm without MWCNT. On similar lines, the β-phase content decreased with the addition of MWCNT. But β-phase was found to double upon doubling the voltage and increased by about 12.5% upon 2% increase in PVDF concentration.

Lithography

Like other MEMS device fabrication techniques, lithographic patterning finds widespread usage in fabrication of micro and nano-scale sensors [34], actuators [35] and other devices from PVDF films. Lithography helps in creating required features on PVDF films without a loss of its piezoelectric properties [36]. In lithography, PVDF films bonded on certain substrates are exposed to radiation. Specifically designed masks are used to protect the required PVDF regions from getting exposed to the radiation. The exposed weakened regions are removed via wet or dry etching [36]. N. An et al. [37] used similar technique to create 10 µm thick grooves on PVDF-TiO_2 composite films. The resolution of the structures produced with this technique is very high. It is convenient to pattern electrodes with thicknesses as low as 0.1 µm on PVDF using lithographic techniques [36, 38].

Soft lithography

Soft lithography or stamping of PVDF at high temperatures and pressures using polydimethoxysilane (PDMS), is used to form PVDF features on flexible substrates [1]. Perez et al. [1] fabricated various kinds of pillars, interconnected networks and freestanding structures with dimensions close to 5 µm as shown in Figure 2.5. Imprinted features (Figure 2.5(a)) were produced by imprinting spin coated PVDF films with PDMS (polydimethoxy silane) stamps at 70°C. Stamped continuous (Figure 2.5(b)) patterns were obtained by spin coating PVDF on the

PDMS mould at about 1000-2000 rpm. To attain the stamped discrete features (Figure 2.5(c)) the PVDF layer connecting the pillars was removed by shearing with a hot glass slide. A thin layer of polyvinyl alcohol was drop-coated on PVDF and removed after several hours of drying resulting in freestanding features (Figure 2.5(d)).

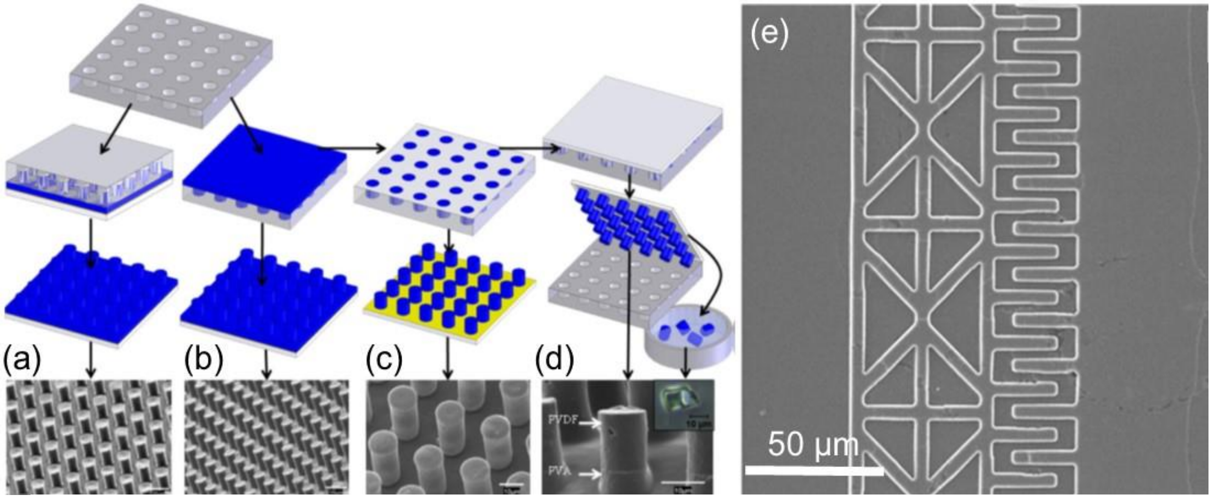

Figure 2.5: Fabrication illustrations for: (a) imprinted; (b) stamped continuous; (c) stamped discrete; and (d) freestanding microstructures [42]; (e) features imprinted on PVDF-TrFE-CFE using silicon stamp [43]

These features find widespread applications in microphones [35], tissue engineering and cell biology [1]. A similar approach of nano-imprinting (Figure 2.5(e)) was used by Shklovsky et al. [39] to create features with a resolution of 3.5 μm with silicon stamps. Limitations of these techniques are rounded corners and deformation of the structures due to high temperatures and pressures.

Electric poling-assisted additive manufacturing (EPAM)

EPAM is a recent advancement in the fabrication of PVDF, combining fused deposition modelling (FDM) with electric poling. Lee et al. [40] modified a conventional FDM machine by attaching electrodes to apply high voltage between the printing head and the bed (Figure 2.6(a)). As the PVDF filament comes out of the extruder, the electric field orients the dipoles creating a net dipole moment in PVDF. Fibers with thicknesses around 500 μm were produced using 1-3 MV m^{-1} of electric fields. Figure 2.6(b) shows networks of PVDF printed on an adhesive substrate. Figure 2.6(c) displays a freestanding device fabricated by EPAM.

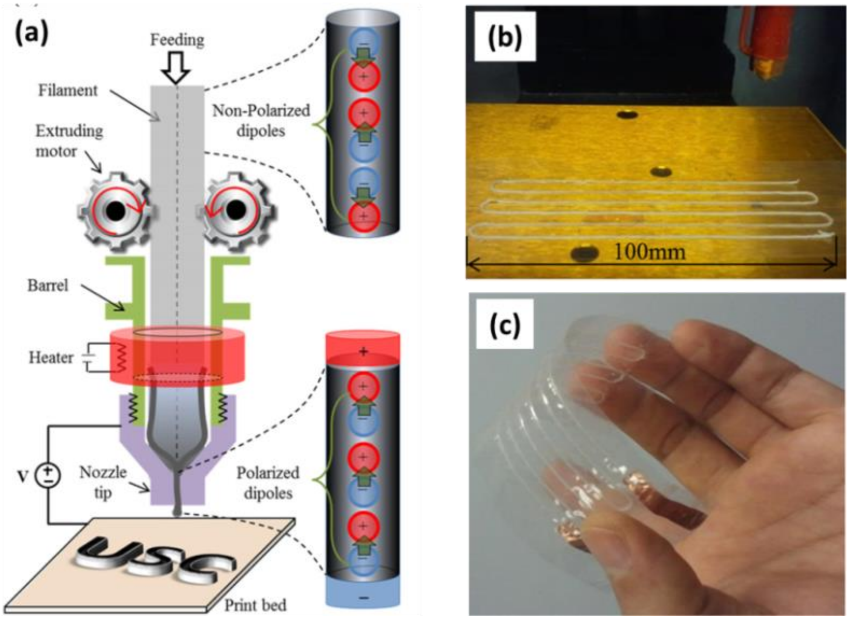

Figure 2.6: (a) Schematic of EPAM system; (b) PVDF networks printed on an adhesive layer; (c) free-standing PVDF sensor [44]

2.2.2 Techniques to characterize different phases in PVDF

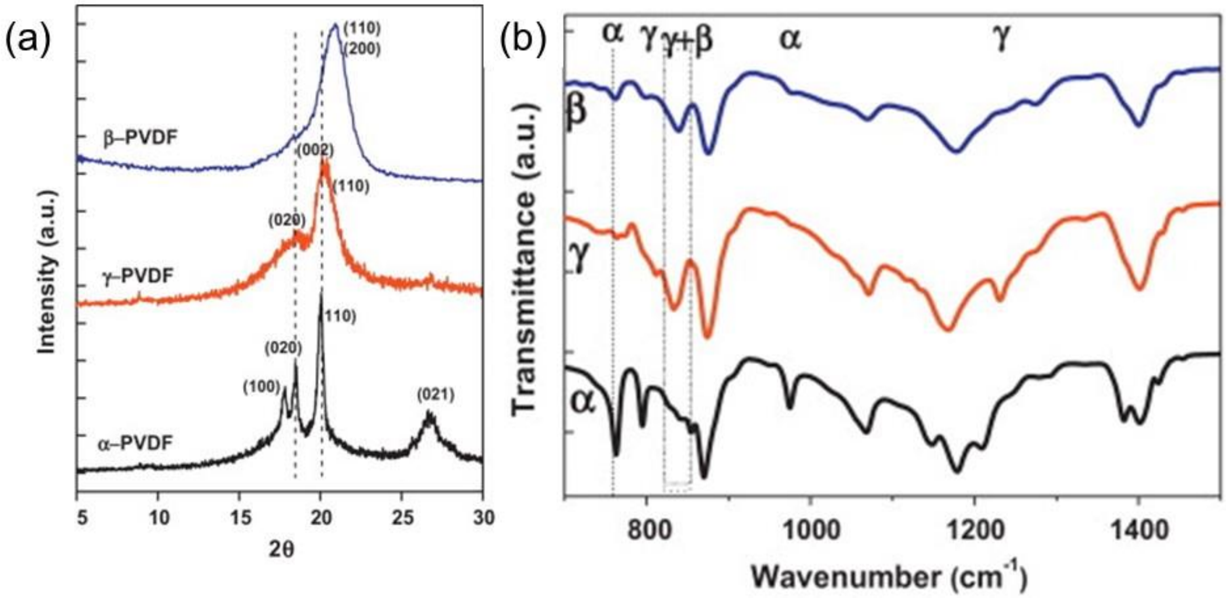

Figure 2.7: Characterization of various phases in PVDF: (a) XRD; (b) FTIR [44]

Characterization of different phases in PVDF involves studying its chemical structure at molecular level. This is usually done by using X-ray diffraction (XRD), Fourier transform infrared spectroscopy (FTIR), Raman spectroscopy, differential scanning calorimetry (DSC), thermogravimetric analysis (TGA), scanning (SEM) and tunnelling electron microscopy (TEM).

X-ray diffraction (XRD): XRD helps in the identification of various phases in PVDF. All the crystalline phases of PVDF have their distinctive peaks in its X-ray diffractogram (Figure 2.7(a)). Peaks corresponding to α-phase are 17.7, 18.4, 19.9 and 26.56° while that of γ-phase are at 20.04 and 26.8° [41, 42]. β-phase is characterized by a well-defined peak at 20.26° [41, 42], broadening of the α-peak at 20.1° and diminishing of α-peaks at 18.4 and 26.7° [43].

Fourier transform infrared spectroscopy (FTIR): FTIR provides the quantification of the phases within PVDF's crystalline domain. Though absorption bands at 840/833 cm^{-1} for β and γ-phase lie very close to each other, the bands at 1279 cm^{-1} are only present in the case of β-phase [42, 44] (Figure 2.7(b)). The characteristic absorption bands for α-phase are close to 615, 766, 855 and 974 cm^{-1} [44]. The amount of β-phase amongst α and β-phases of PVDF is calculated with the help of Beer-Lambert law, which relates the absorption to the concentration of the species. The modified Beer-Lambert law for obtaining the fraction of β-phase is given by the following equation [45]:

Fraction of β-phase,

$$F_\beta = \frac{A_\beta}{1.26A_\alpha + A_\beta} \tag{2.4}$$

where, A_α and A_β are the absorptions fractions of α and β-phases at 763 cm^{-1} and 840 cm^{-1}, respectively, and 1.26 is the ratio of absorption coefficients 7.7×10^4 and 6.1×10^4 cm^2/mol of β and α-phases, respectively.

Piezoelectric constant measurements: Piezoelectricity is a combination of dielectric constant and polarization. Dielectric constant is calculated from the impedance versus frequency sweep curves obtained from an impedance analyzer. The piezoelectric constants can be directly obtained by applying a known force and measuring the charge outputs (d_{ij} in C N^{-1}) or by applying an electrical signal and measuring the deflection (g_{ij} in V m^{-1}). Some specialized commercial devices like d_{33} meters [46] can also be used.

2.2.3 Attainment of β-phase in PVDF

As evident from the chemical structure of PVDF, β-phase is the most essential polymorph of PVDF which is a prerequisite for all the piezoelectric applications. As PVDF is natively formed in its α-phase, it is essential to convert this α-phase into β-phase. Formation of the polar β-phase involves treatments which can be provided separately or incorporated simultaneously during the fabrication of PVDF films or structures. Following is an account of a few such methods utilised in the physical transformation of PVDF into its β-phase.

Thermal Poling

Poling is a process of orienting the polar crystallites in PVDF. It helps in acquiring opposite charge distribution on the two surfaces of a film. This is facilitated by application of high electric fields at elevated temperatures to obtain a net dipole moment.

For a complete phase transformation to take place, the temperatures are usually near the Curie-temperature of PVDF (~120 °C) [47]. Thermal poling of PVDF is carried out in a dielectric medium (e.g., silicon oil which also helps to maintain uniform temperature). As shown in Figure 2.8, a high electric field is applied to metalized films for a few hours. DC fields ranging from 10 – 200 MV m^{-1} are used for poling of solution cast or drawn PVDF films. The field is usually kept on until the oil cools down to “freeze” the dipoles, thereby, preventing depolarization of (i.e., scattering back of the dipoles to their random state).

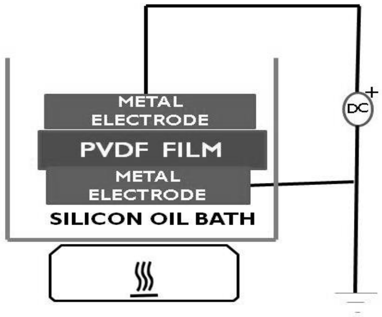

Figure 2.8: Schematic of the thermal poling [52]

Stretching

Mechanical stretching of PVDF films as well as fibers transforms the non-polar α crystallites into polar β combined with orientation of dipoles in the stretch direction [48]. Both uniaxial and biaxial stretching are carried out depending on the application. A typical stretching apparatus resembles a universal tensile testing machine. The film is held between grips at both the ends and is stretched at a constant strain rate [49]. The strain rates and draw ratios vary with thickness of the films as well as their application. Typical draw ratios from 4.5 to 6 [22, 48] and strain rates between 25 to 50 cm min^{-1}[49, 50] in a specific temperature range yield higher β-phase. The entire set up is usually placed inside a temperature controlled airtight chamber. Again, stretching at higher temperatures yields higher orientation of dipoles due to increased mobility. Mohammadi et al., obtained about 86.5% β-phase with a stretch rate of 50 mm min^{-1} [49].

Filler Addition

Fillers like carbon nanotubes [33, 51], clay [52], cellulose [53], magnetic [27] and piezoelectric nanoparticles [54] have proven to be very effective in β-phase retention. Fillers are incorporated into PVDF via ultrasonication [55] or mechanical stirring [56] to obtain a homogenous dispersion and their adherence to the PVDF chains. These fillers bearing heavy molecular chains adhere to the polar crystallites in PVDF and prevent their disorientation. Electrospinning of PVDF with 1% $BaTiO_3$ particles, upon treatment with 3% tetraiso-pentyl ammonium chloride (TIPAC), resulted in about 100% β-phase [57].

2.3 Advantages of 3D structures over 2D piezoelectric structures

The extension of the sensing capabilities of planar piezoelectrics into the third dimension is of prospect owing to improved electromechanical response extractable from 3D designs. Such an improvement stems from the augmentation of both accessible strain and coupling between associated piezoelectric coefficients. Yiin-Kuen et. al, carried out a comparison between the piezoelectric properties of a flat sheet (2D) and a rolled over version of the device with the same dimensions into a cylinder as shown in Figure 2.9 [58]. The device consisted of a layer of PVDF micro/nano fibers (MNFs) sandwiched between electrodes and packaged in PDMS. The devices in the form of sheets were manually rolled into cylinders with different diameters to study the advantages of the third dimension. They demonstrated over 2-fold increase in the output of the cylindrical device (4.1 V/295 nA) with 0.34 cm diameter over the unrolled device (1.9 V/ 140 nA). The authors address this increase in output power to the following reasons: (i) increased compliance along the out-of-plane directions and (ii) electromechanical interaction between the contacts of the PVDF fibers. The power output further depends on the diameter of the rolled cylinder. They also observed that the output voltage decreased with an increase in the diameter from 0.34 to 0.48 cm. This implicates that the geometry of the 3D structures plays an important role in determining power conversion.

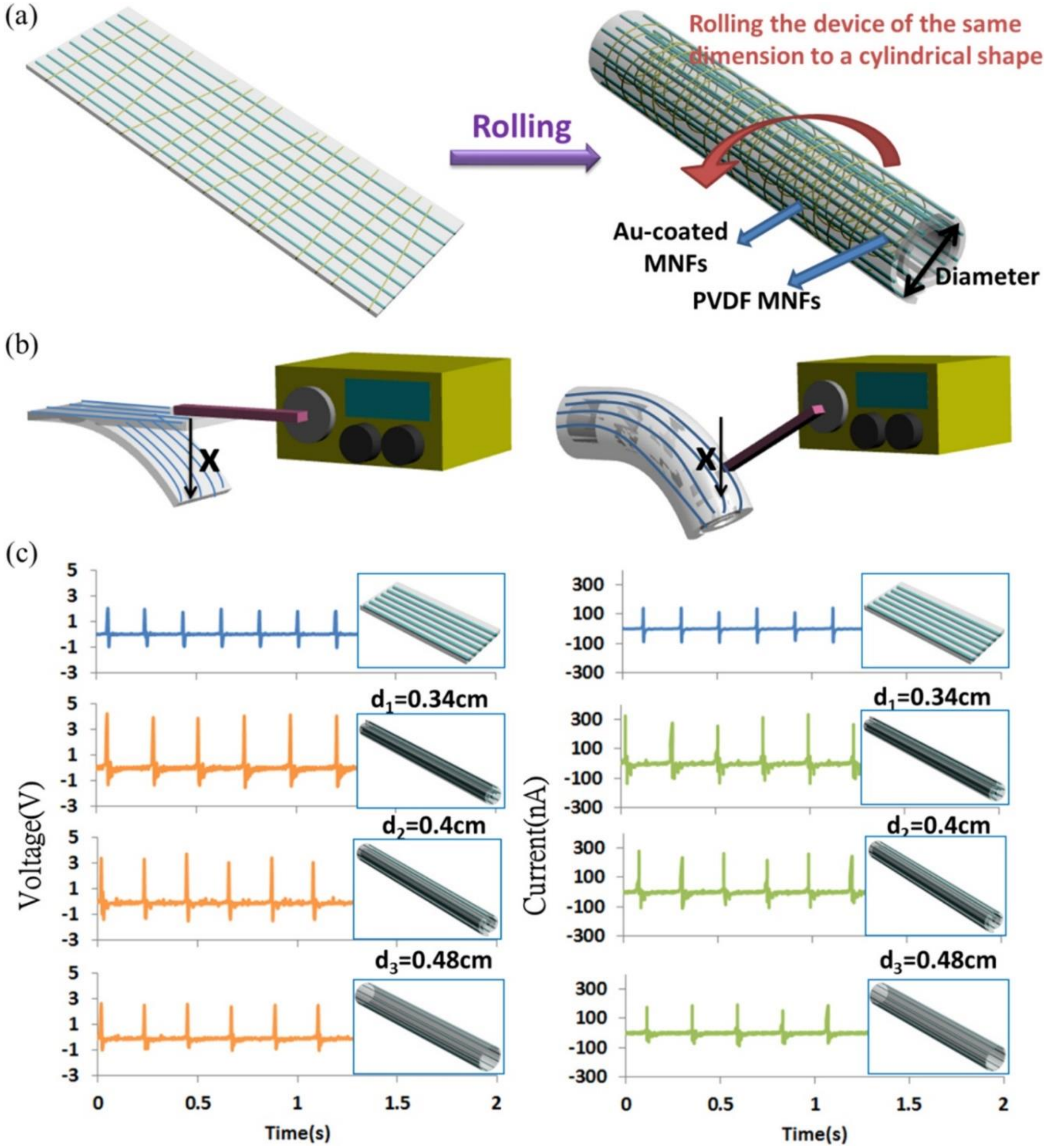

Figure 2.9: (a) Schematic diagram of a flat piezoelectric sensor and a rolled device of the same dimension in the form of a cylinder with varying diameters. (b) Schematic of the test setup. (c) Output voltage and current for stretching and releasing at 5 Hz [58]

2.4 Three-dimensional printing

Three-dimensional (3D) printing is a bottom-up approach involving computer-aided fabrication of 3D structures via material addition. The main advantages of 3D printing compared to conventional fabrication techniques are rapid prototyping, miniaturizing, and fabricating 3D structures on versatile substrates. Functional and structural materials ranging from ceramics, metals and polymers to biomaterials can be fabricated via 3D printing. According to Hon et.al. [59], 3D printing techniques to develop 3D structures for microelectronics, aerospace, automotive and biomedical applications, can be largely classified into four categories: droplet-based, energy-based, tip-based and flow-based techniques as shown in Figure 2.10 [59].

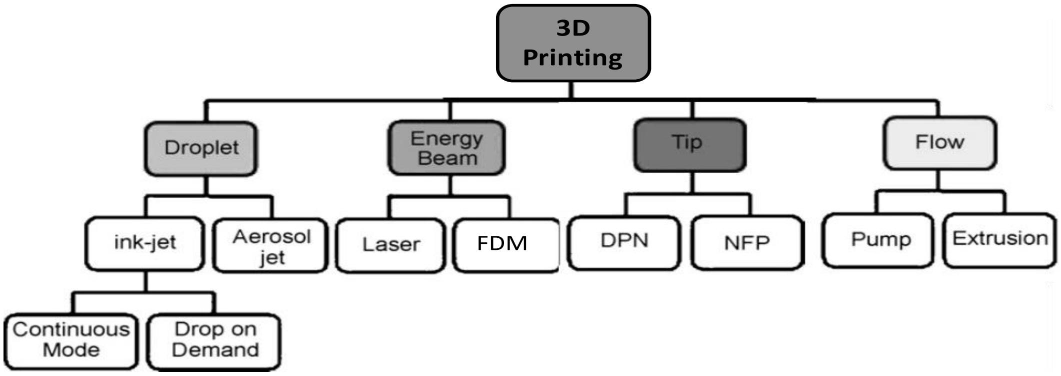

Figure 2.10: Classification of 3D printing techniques [65]

Droplet-based techniques use extremely low viscosity solutions to create patterns on a substrate. The principle of printing is very similar to 2D inkjet printing. Droplet-based processes include continuous and intermittent or drop-on-demand deposition of fluids [59] and aerosols [59] on the substrates using an actuator-nozzle system.

Energy-based approaches use high energy sources such as laser, photon or electron beam to ablate, polymerise, sinter or sputter materials and obtain the required shapes. Energy based processes are mainly classified into – laser assisted chemical vapour deposition (LACVD), laser induced forward transfer (LIFT), fused deposition modelling (FDM) [60], focussed ion beam deposition (FIBD), multi-photon polymerisation (MPP) and others. Tip-based DW techniques use tips of atomic force microscope (AFM) and are better known as dip pen nanolithography (DPN).

Flow-based techniques, employ a mechanical force or pressure to extrude materials from syringe barrels and deposit them on the substrates [59]. Flow based techniques print inks, pastes, colloids, dispersions and solutions onto the required substrates at programmed speeds and flow-rates at micron as well as sub-micron range [61]. Previous work demonstrated the layer-by-layer printing of structures using colloidal suspensions [62], fugitive inks [63], silver nanoparticles inks [64], UV-curable epoxy [65] and many more. Solidification of these materials is a result of either their coagulation in a reservoir, suppression of repulsive forces or UV polymerization. Methods have also been developed to fabricate structures with more than a single kind of ink, thereby facilitating co-fabrication of different materials [66]. Out of these flow based techniques, UV-assisted 3D printing is known to possess the capabilities to form 3D self-supporting as well as freeform structures (without any support features) from UV curable epoxies at room temperature [67].

Recent advances in solvent-cast 3D printing have also shown to create freeform structures [68]. Solvent-cast 3D printing involves the fabrication of structures of polymers by using their solutions with low boiling point solvents. This technique opens a new realm of fabricating self-supporting and freestanding structures of polymers at low costs.

2.5 3D printing of piezoelectric materials

3D printing of piezoelectric materials can result in superior properties along with the possibility to form multi-layered and complex architectures [69, 70]. Apart from NFES technique explained in section 2.3.2, various methods, both light and extrusion based, have been used till date to print piezoelectric materials: ceramics, polymers as well as composites in 3D.

2.5.1 Direct-write (DW)

3D printing of piezoelectric materials was first attempted in 2004, by Smay et. al, using DW. DW technique, as seen in Figure 2.11(a), is a flow based technique that involves extrusion of a solution under mechanical or pneumatic pressure by a moving robotic arm. As discussed in the previous section the material solidifies once it exits the nozzle. Linear and annular arrays were fabricated from a colloidal solution of PZT [71]. After printing the parts were bisque-fired and sintered for rigidity.

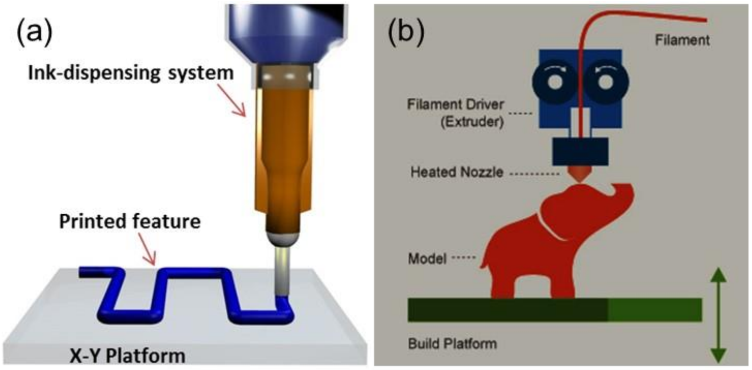

Figure 2.11: (a) Schematic of flow-based DW technique [69]; (b) Schematic of FDM [78]

2.5.2 Fused deposition modelling

Fused deposition modelling (Figure 2.11(b)) is a very common 3D printing technique for thermoplastics. PVDF or its copolymers are fed into an extruder using polymer spools. As the names suggests, the polymer is melted by passing through an extruder that deposits it layer-by-layer on a platform creating the required 3D structure. The polymer filament coming out of the extruder solidifies as it prints the desired shape. The polymer can be poled while printing [72] or post-printing [73]. Suaste-Gomez et.al., fabricated a prosthetic ear to sense both pressure and temperature [73]. Corona poling at 15 kV was used to polarize the PVDF ear.

2.5.3 Selective laser sintering

Selective laser sintering is a process primarily used to form 3D structures from ceramics and their composites. As seen from Figure 2.12 (a), it involves the deposition of a layer of ceramic powder on a bed. A moving laser then sinters the profile according to the required design. Once the first layer is completed, the bed moves down and a roller feeds in another layer of the ceramic powder and the process is repeated until the completion of the part. SLS has been used to print $BaTiO_3$ [74], composites of PVDF with PZT [75] and nano-sized bio-glass [76] in the form of cubes and scaffolds (Figure 2.12(b)).

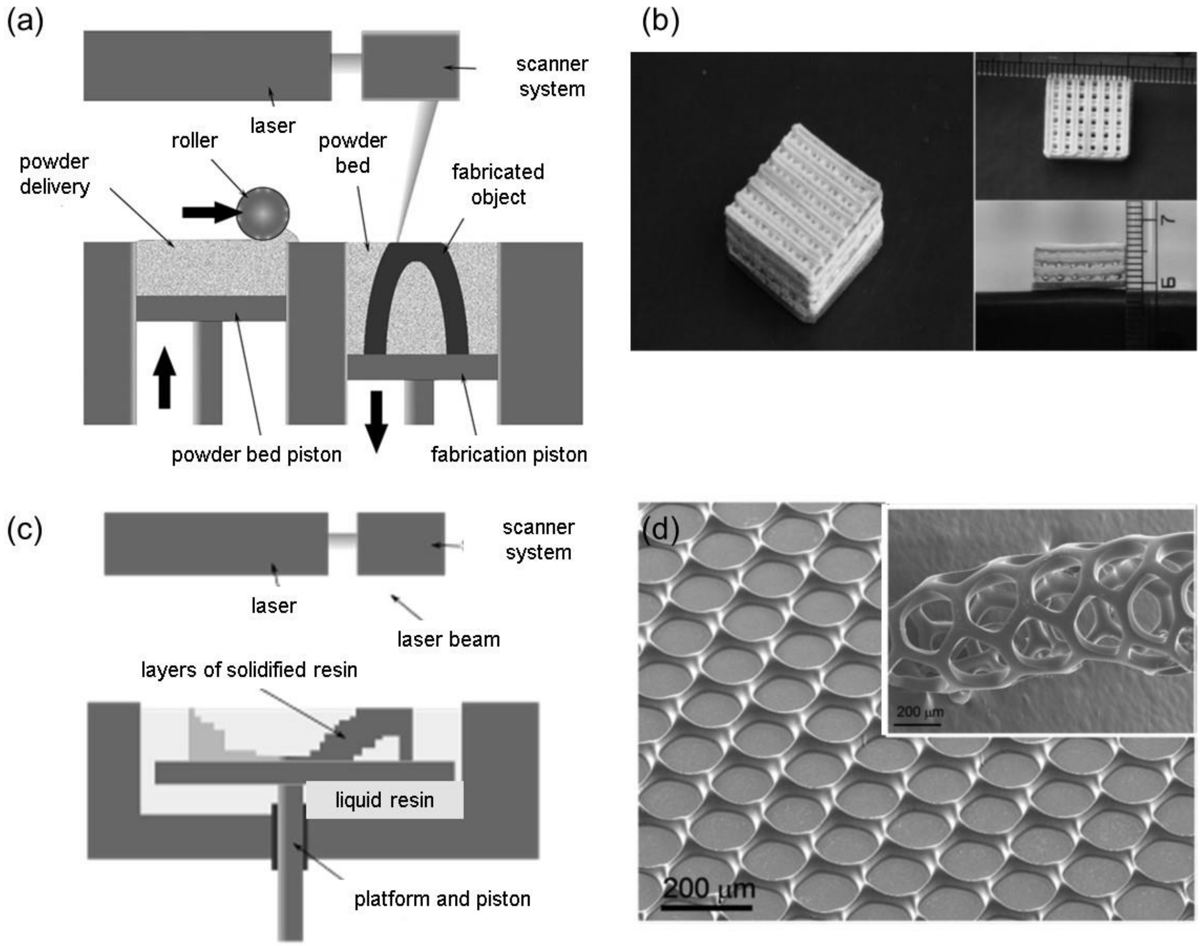

Figure 2.12: (a) Schematic of selective laser sintering process [84]; (b) 3D printed cube [83]; (c) Schematic of stereolithography [78]; (d) SEM image of a stereolithography printed structure, inset: printed layer upon detaching from the substrate and rolling [75]

2.5.4 Stereolithography

As opposed to the powder based SLS, stereolithography (SLA) involves the curing of monomer (pure or with fillers) by a laser. A tank is filled with a resin as seen in Figure 2.12(c), a laser beam selectively scans the polymer surface as per the drawing submitted to the printer. Similar to SLS, once the first layer is cured the platform moves down and the process repeats. High resolution structures can be fabricated by this method. Modifications of this method include an array of mirrors to simultaneously cure an entire layer or replacement of the laser by light with different wavelengths (dynamic optical projection stereolithography, DOPsL). Kim et. al used DOPsL to fabricate fine microstructures: dots, square and honey comb arrays etc. using nanocomposites of $BaTiO_3$ nanoparticles in photoliable polymers. As seen from figure 2.12(d) the microstructures had very high resolution and once released from the substrates they could further form freeform structures as in the inset [69]. Similar method has also been used to print mesoscale honeycomb capacitors using silver coated PZT particles [77] and ultrasonic sensors using $BaTiO_3$ nanoparticles in photocurable resins [78].

The structures fabricated by both SLA and SLS need to be poled at high voltages after sintering.

2.5.5 Solvent evaporation-assisted 3D printing

Solvent evaporation-assisted 3D printing involves the dispersion of a polymer or its nanocomposite into a rapidly evaporating solvent to print self-supporting as well as freestanding structures [68]. A concentrated solution of the polymer is poured into a syringe and extruded with the help of pneumatic pressure onto a robotically controlled stage to acquire the required shape. As seen in Figure 2.13(a, b), the fast evaporation of solvents imparts rigidity to the printed shape.

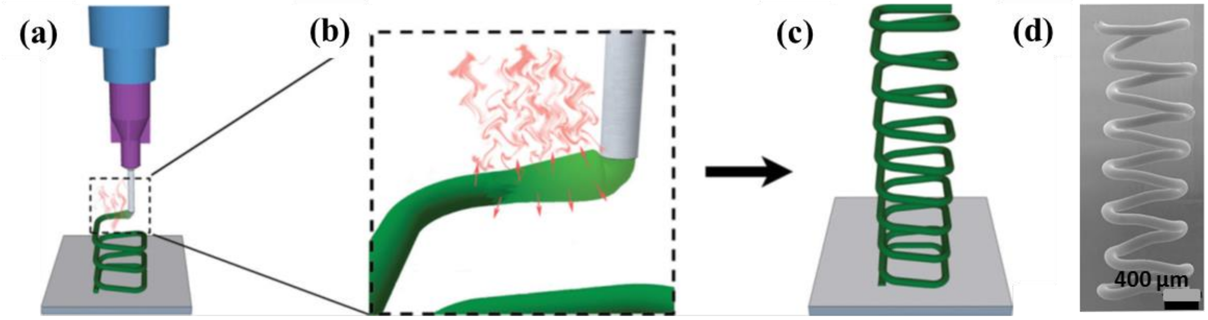

Figure 2.13: Solvent cast 3D printing technique to fabricate 3D freeform square spiral. (a) Schematic of solution extrusion; (b) solvent evaporation; (c) freeform 3D structure; (d) SEM image of the 3D printed polylactic acid (PLA) spiral [74]

The ability to 3D print freestanding structures requires a thorough investigation of the effect of polymer concentration, extrusion pressure, velocity of the stage, diameter of the needle and the distance between the needle and the stage [79]. Self-supporting scaffolds as well as freeform square spiral (Figure 2.13(c, d)) and circular spirals were produced [68].

2.6 Applications of piezoelectric materials

PVDF is a versatile material with applications ranging from filtration membranes to energy harvesters. While filtration membranes and coatings exploit its chemically inert nature;

electronics utilise its pyro, piezo and ferroelectric properties. Its biocompatibility is further advantageous for bone implants, sutures and tissue culture. PVDF sensors, actuators and energy harvesters at macro, micro and nano levels find widespread applications in tons of electronic devices. Being a polymer with high elasticity adds its growing demand for flexible electronics. The following subsections give an overview of PVDF's sensing applications relevant to this thesis.

2.6.1 Sensing applications

Microprobes made from PVDF strips are used to detect cell forces [80, 81] as small as 50 µN [80]. Motion sensors made from PVDF films find applications in insect locomotion, automotive tire deformation measurements [82] and autonomous underwater vehicles [83]. Huang et al. [83], obtained a water pressure sensitivity of 0.071 mV Pa^{-1} for a set of PVDF films to monitor the motion of a robotic fish. The sensitivity of the strain sensors increases with increase in area. PVDF strain sensors find applications in modal testing [84], structural health monitoring [85].

2.6.2 Smart textiles

Smart textiles are clothing with woven electronics that can sense, react and adapt to various stimuli [86, 87]. Depending on whether the clothing can react or not, it can be classified into active or passive. Further if the clothing adapts to the stimuli or environment it is termed as ultra-intelligent. The components: electronics and materials with multi-functionality, that make the clothing intelligent can be either embedded, woven in the textiles or even directly embedded into the fibers themselves (Figure 2.14). Basically, smart textiles have been used to light LEDs, heat the garments and provide biometric data.

The major requirements for the smart fabrics are: water resistance, light-weight, comfortability and the ability to withstand impact, sweat, washing machines [88]. Table 2.2 is a short overview of the smart textile industry over the past decade.

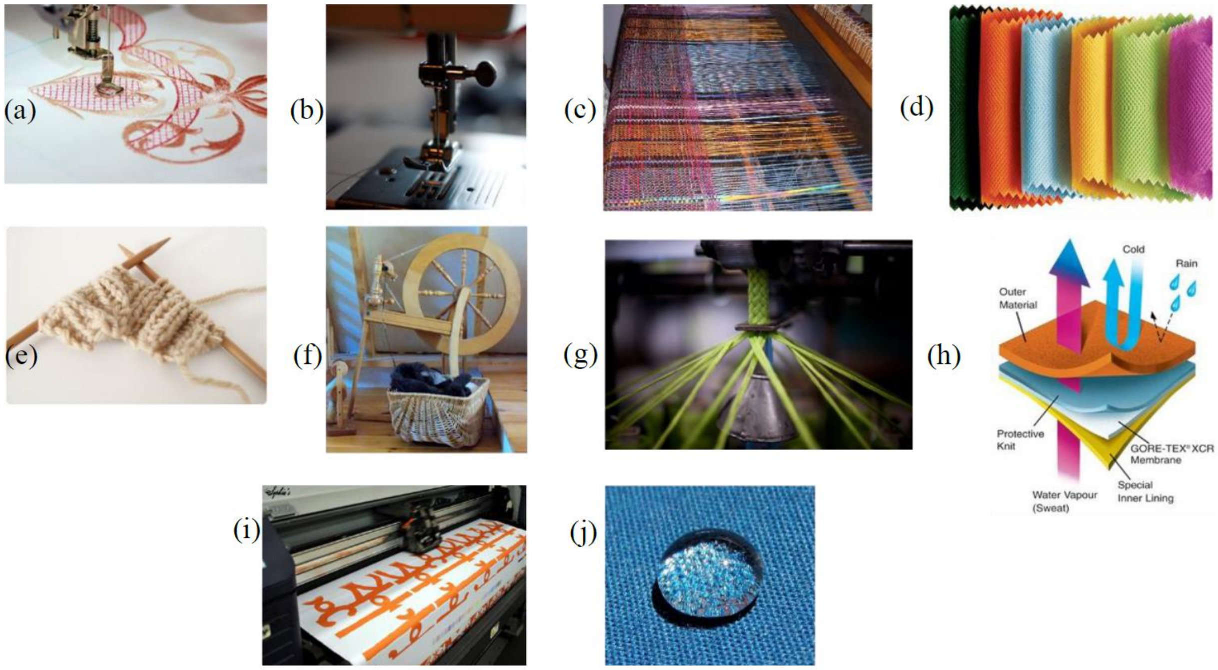

Figure 2.14: Different kinds of fabric/textile manufacturing and treatments (a) embroidery; (b) sewing; (c) weaving; (d) non-woven; (e) knitting; (f) spinning; (g) breading; (h) coating/laminating; (i) printing and (j) chemical treatment. [96]

Table 2-2: Overview of smart textile industry over past decade [97]

Company	Function (technology)	Garment type	Advantages	Limitations
Sefar	heating (conductive wire)	jacket	• waterproof • light weight	• need to turn on heat manually • battery powered
Therm-IC	heating	gloves, socks, jackets, shoe insoles		• durability • battery powered
Clothing+	biometric monitoring	sport bras	• impact-proof • machine washable	battery powered

Table 2-2: Overview of smart textile industry over past decade [97]

AiQ Smart Clothing	lighting, heating, biometric monitoring (stainless steel yarn)	gloves, jackets	• waterproof • light weight • machine • washable • soft • radiation shielding	battery powered
Om Signal	effort level, calories burned, steps taken, sweat levels, and heart rate	designer workout outfit		expensive
Hexoskin	biometric monitoring	Shirt	long lasting batteries (~ 14 h)	expensive
Leo	measure the body’s lactic acid, hydration, muscle coordination, technique, balance and intensity	not exactly a textile	low cost	
Wearable Life Science	stimulates muscles (electronic muscle stimulation pads)	long pants, compression shorts, t-shirts, calf guards, wings and tank tops	seamless	need for an electronic, plastic booster in the clothing: non-washable

Table 2-2: Overview of smart textile industry over past decade [97]

Wearable experiments	guiding postures directions	tights, jackets	• invisible • waterproof • durable • integrated GPS	
Pauline Van Dongen	charging portable electronics (solar panels and flexible electronics)	shirts, jackets	• self-powered • invisible • waterproof	expensive
Anouk Wipprecht	monitor the space around the wearer, body-sensors check in on stress levels	dress	•	expensive

Though there has been more than a decade of pioneering research in the field of smart textiles, they are still limited to extreme sports, fitness and entertainment only. The major limiting factors are the durability, high price, battery replacement or recharging requirements and the shorting of the conducting wires in the garments. These limitations can be overcome by using a sustainable material technology consisting of self-powered sensors, which could eliminate batteries and lower the costs and make smart textiles affordable to everyone.

2.6.3 Research in the field of wearable sensors for healthcare

Wearable electronics are increasingly sought after in medicine to replace the bulky ambulatory diagnostic equipment. Application of wearable electronics in clinical procedures will enable real-time diagnosis of physical and physiological parameters in patients. Figure 2.15 shows various sensors to detect temperature, strain, pressure, wound-healing and many such parameters on and inside human body. Sensors developed mainly rely on three major technologies: piezoresistive, piezoelectric and capacitive.

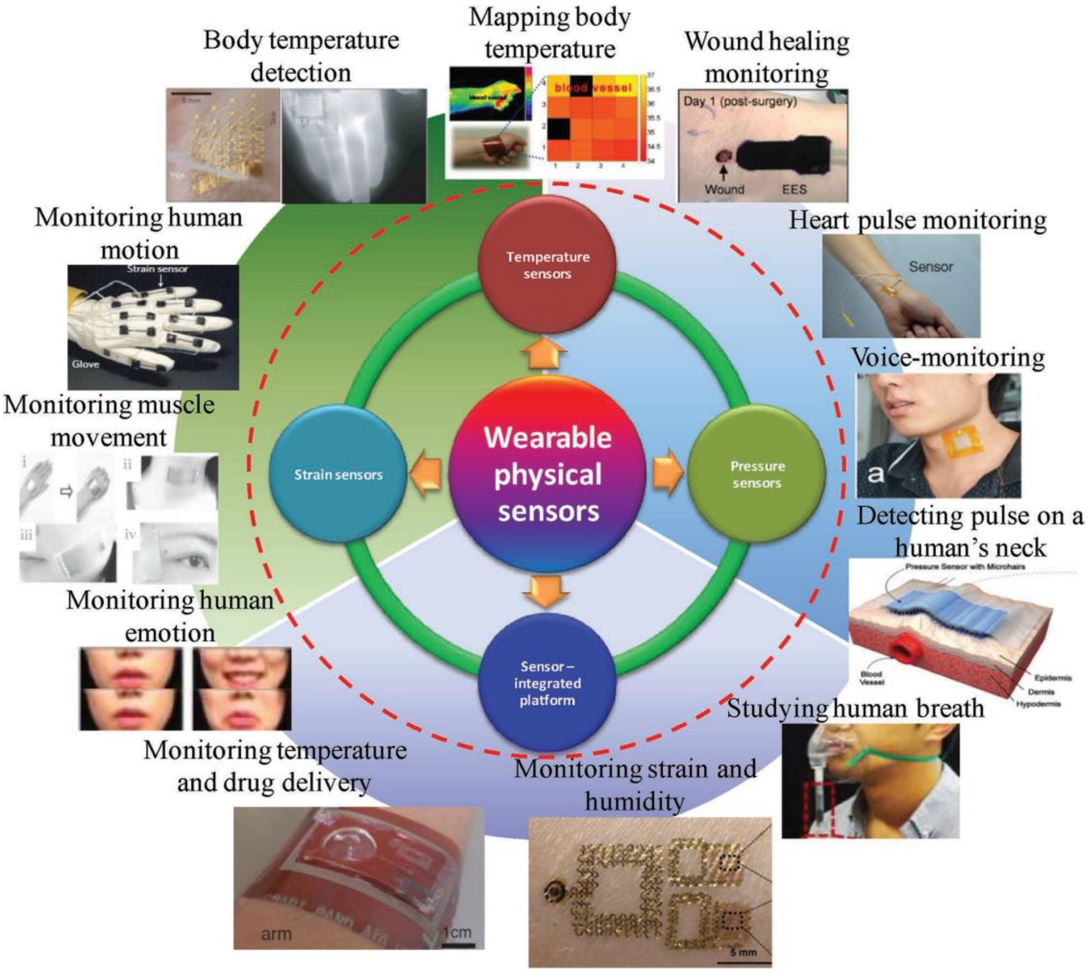

Figure 2.15: Characteristic properties of recently developed wearable physical sensors for monitoring human activity and personal healthcare [98]

Both piezo-resistive and capacitive sensors are passive in nature i.e., they need to be externally powered by batteries whereas piezoelectric sensors are self-powered and hence active.

2.6.4 Motion sensing

Flexible strain sensors measuring the deformation of human body during various activities like breathing, bending movements of limbs and spine, running, walking have been developed using both passive and active technologies as seen in Table 2.3.

A highly stretchable (strain of 280%) piezoresistive strain sensor developed using sparsely spaced and vertically aligned single-walled carbon nanotube (SWCNT) films is shown in Figure 2.16(a and b) [89]. The sensors were laminated into clothes to be in contact with the skin. Change

Table 2-3: Summary of strain sensors in detecting human motion

Active materials	**Sensing mechanism**	**Flexibility (F) / Stretch-ability (S)**	**Quantity sensed**	**Ref.**
P(VDF-TrFE)/transistor	Piezoelectric	F[0.25%]	finger and wrist bending	[90]
MWCNTs/PU composite	Piezoresistive	S [400%]	knee bending while cycling	[91]
Aligned SWCNT films	Piezoresistive	S [280%]	throat, knee and finger movements	[89]
Hybrid SWCNTs and PEDOT:PSS/PU	Piezoresistive	S [100%]	facial emotions	[92]
CB/PDMS composite	Piezoresistive	S [80%]	finger bending	[93]
CB/PDMS composite	Piezoresistive	S [150%]	wrist movement	[94]
CVD-graphene	Piezoresistive	S [7.1%]	finger movement	[95]
Graphene woven fabric	Piezoresistive	S [30%]	expression, respiration, pulse	[96]
Graphene nanosheet composite	Piezoresistive	S [100%]	Finger movements	[97]
PEDOT:PSS-PVA	Piezoresistive	F [1.2%]	Finger bending	[98]
AgNWs composite	Piezoresistive	S [70%]	Finger bending	[99]
ZnO NW/PS nanofiber	Piezoresistive	S [50%]	Finger movement	[100]
Ag nanoparticles	Piezoresistive	S [20%]	Finger and wrist bending	[101]
CNTs/PDMS/CNTs	Capacitive	S [300%]	Finger folding and breathing	[102]
AgNWs/Ecofl ex/ AgNWs	Capacitive	S [50%]	Thumb and knee movements	[103]

in resistance of the sensor placed on a knee-ball-joint when deformed during extending, flexing, marching, squatting, and jumping is shown in Figure 2.16(c and d).

An active sensor to monitor elbow joint movements was recently demonstrated using a fiber made from zinc oxide (ZnO) nanowires deposited on an electrode coated core fiber [104]. The fiber with ZnO nanowires was covered with deposited PVDF to impart flexibility to the sensor. The final electrode was then dip coated on the PVDF layer as seen in Figure 2.17 (a). Figure 2.17(b) shows the laminated fiber sensor attached on an elbow with tape. The voltage and the current outputs upon folding and releasing the elbow are also presented (Figure 2.17(c).) In another attempt, PVDF microfibers were deposited on Cu coated PVC substrates via NFES (Figure 2.18(a) [105]. These sensors were used to measure the knee-joint movements as seen in

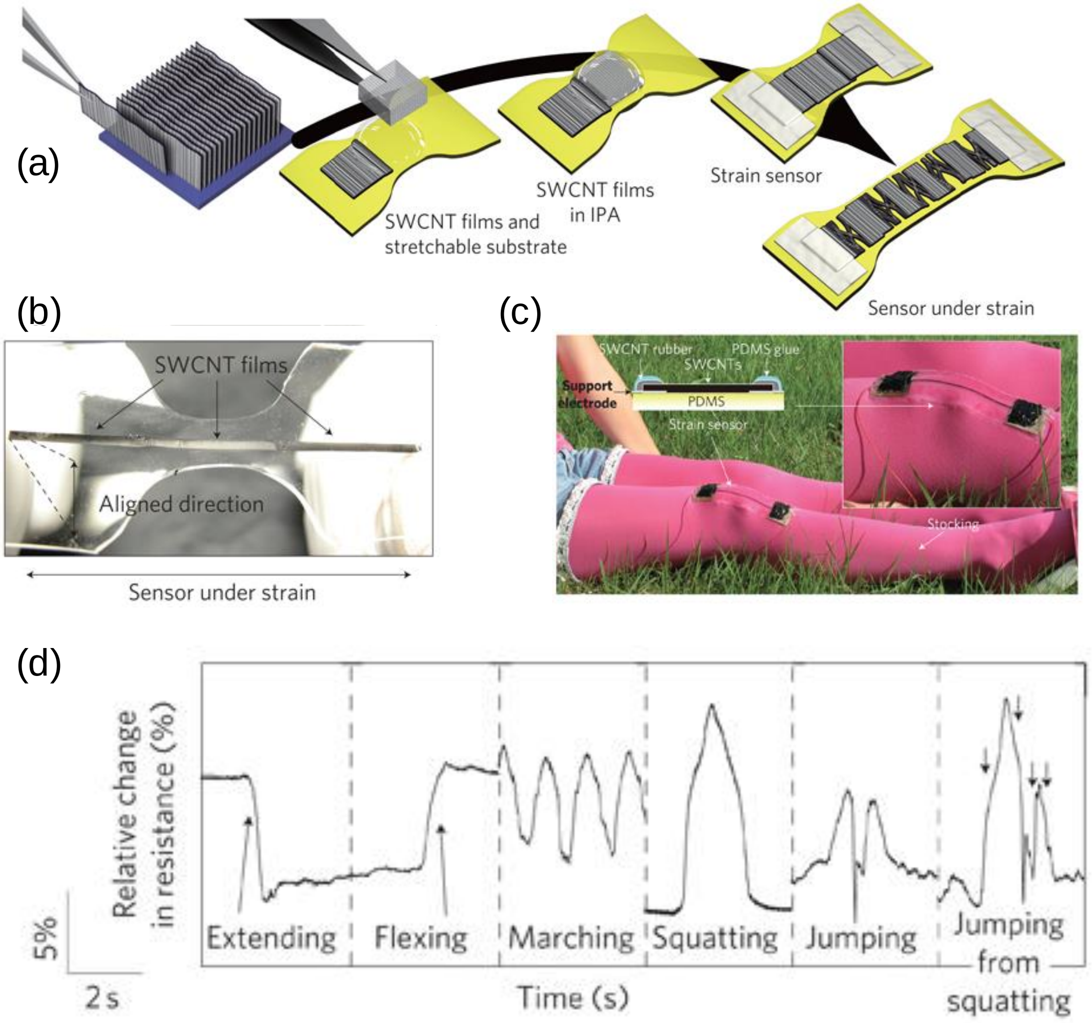

Figure 2.16: (a) Key steps in fabricating the SWCNT strain sensor; (b) photograph of the sensor; (c) strain sensor attached to a stocking on the knee-joint; (d) relative changes in the resistance of the strain sensors due to various motions [101]

Figure 2.18(b and c). Both the above-mentioned sensors and most others used today are either coated in PDMS or other flexible polymers and attached to the human body via gluing, taping or bandaging. This not only leads to clumsy contacts but also causes a lot of discomfort to the users.

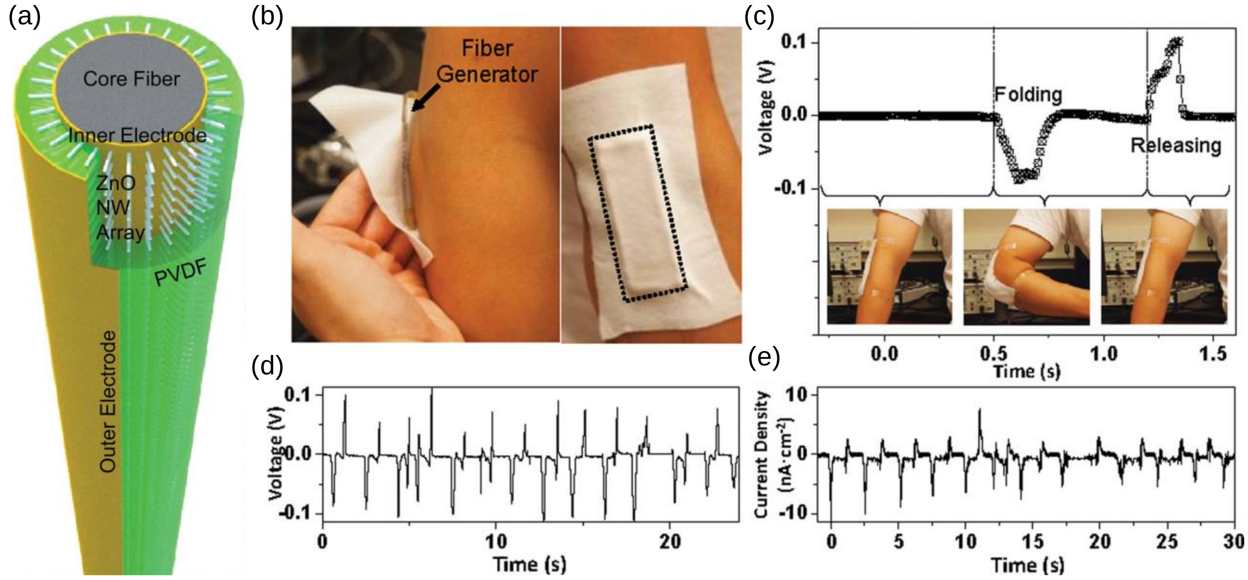

Figure 2.17: (a) Schematic of the hybrid nanogenerator; (b) Optical images of the hybrid-fiber device attached on an elbow on a plane PS substrate and covered with PDMS; (c) Open-circuit voltage output of a fiber device while folding and releasing of the elbow; Open-circuit (d) voltage and (e) current outputs of a fiber device during multiple folding-releasing events of the elbow [104]

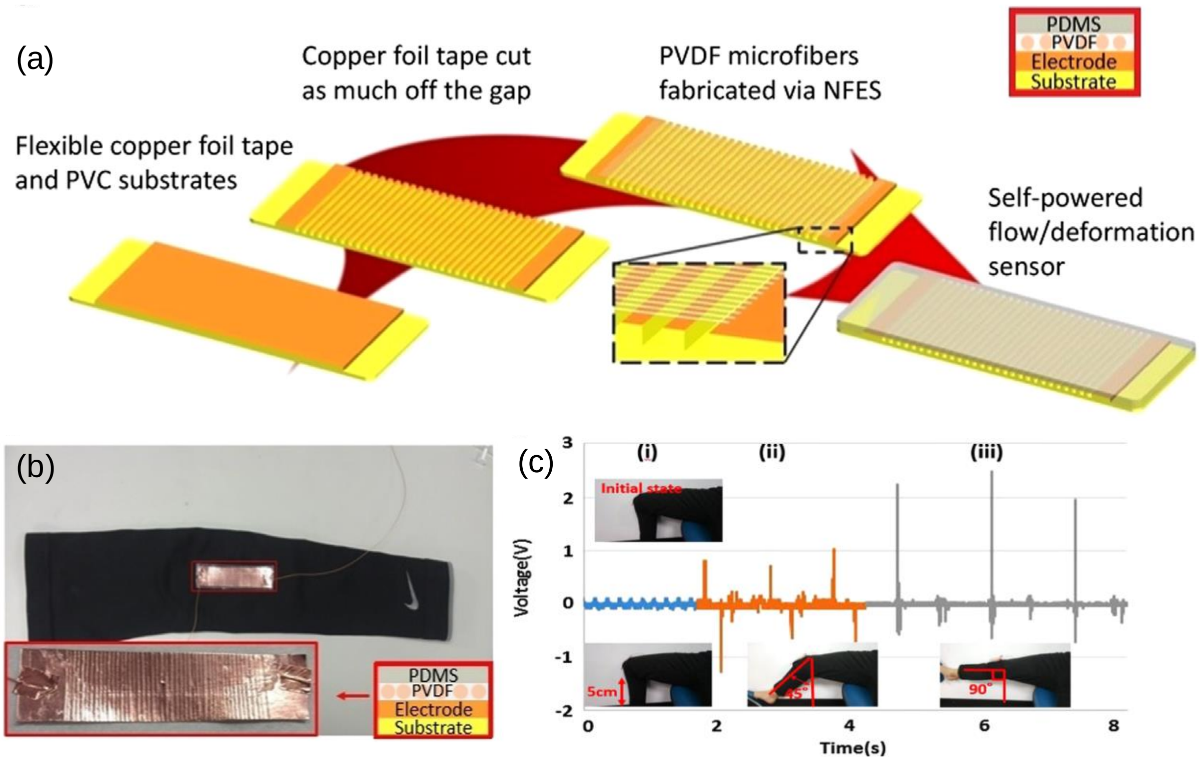

Figure 2.18: (a) Crucial steps in fabricating the self-powered strain sensor. (b) Photographic image of the PVDF fiber-based micro-cantilever attached on the garment. The inset shows the top-view and related cross-section of the PVDF fiber-based micro-cantilever device (c) Photograph of the pants with sensor attached to the knee region; initial state, bent at various angles and return to the initial state along with the output voltage [105]

2.6.5 Respiration sensing

Respiration is a physiological phenomenon involving the expansion of the chest cavity during inhalation and contraction during exhalation. A respiration cycle consists of one inhale and one exhale, and the number of the respiration cycles determines the respiration rate. For normal breathing at rest the respiration rate is around 12-20 cycles per minute [106]. Kumar et. al, carried out a detailed study to find the most convenient location to place capacitive respiration monitoring sensors. Their study presented that the frontal and posterior abdomen was the optimum position to place the electrodes, which along with the body in between would then form a capacitive sensor. As the body expanded and contracted during breathing, the change in the distance between the two electrodes was recorded as the change in capacitance. This change in capacitance with different kinds of breathing exercises is shown in Figure 2.19.

An example of an active piezoelectric breathing sensor is a PVDF sensing film embedded in a PDMS module as shown in Figure 2.20 [107]. The shape of the sensor was optimized to avoid the noise. The location of the sensor and its response compared with a commercial respiratory sensor under sitting and walking conditions is shown in Figure 2.21.

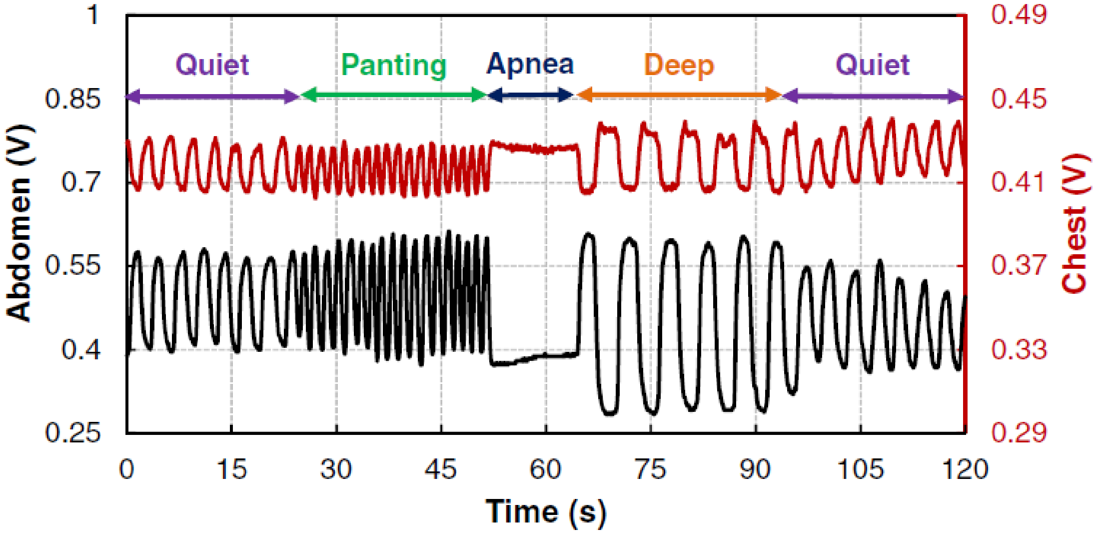

Figure 2.19: Respiration signals measured using abdomen and chest electrodes using wearable respiratory sensor set up [116]

Figure 2.20: Photograph of sensor patch (transparent = PDMS and opaque = PVDF) [117]

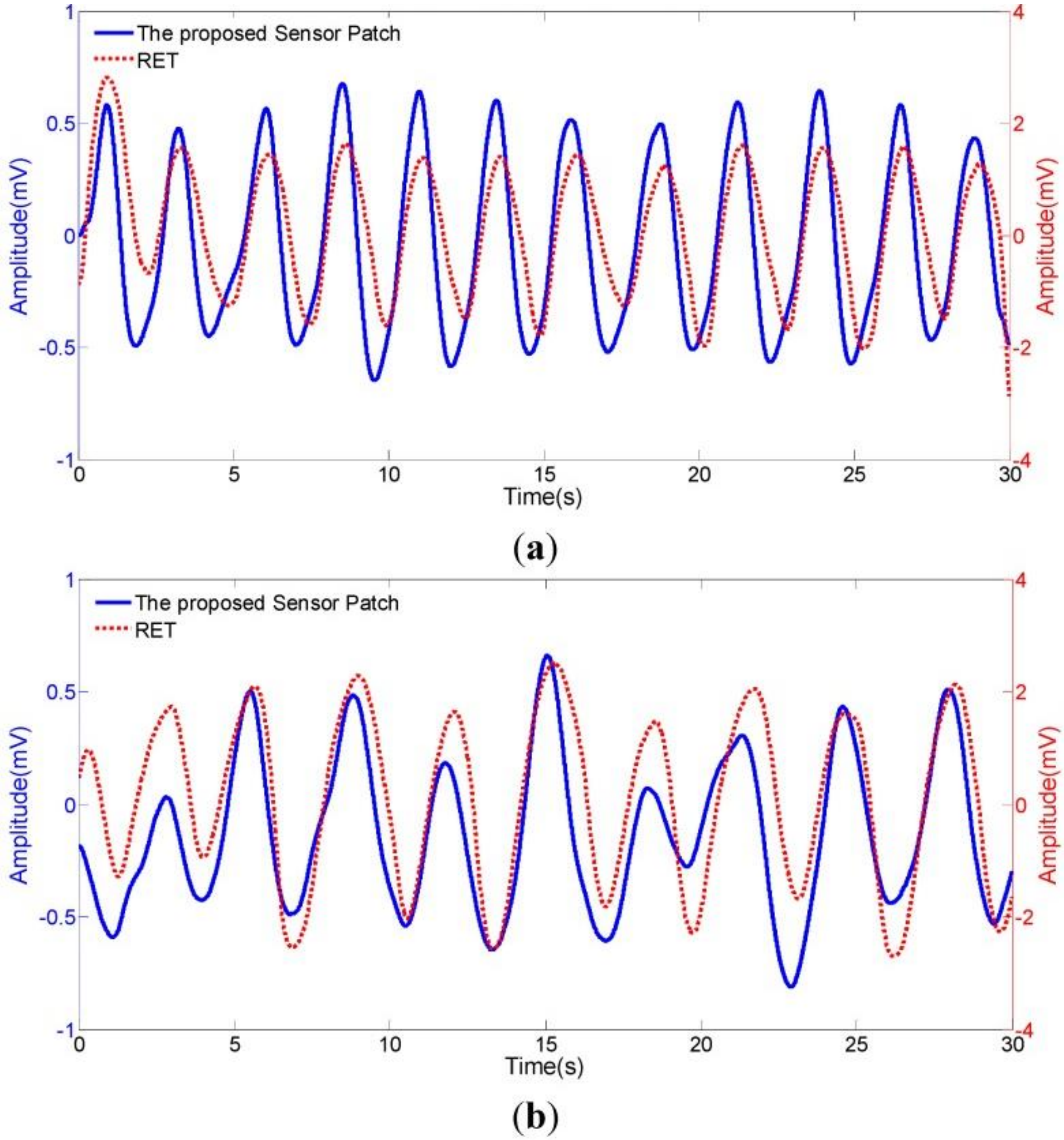

Figure 2.21: Comparison of the electrical signals acquired from the sensor patch and a commercial respiratory effort transducer (RET) under (a) sitting and (b) walking conditions [117]

2.6.6 Structural health monitoring

Structural health monitoring (SHM) is defined as the process of real-time damage detection in structural components of aerospace structures, wind turbines [108], bridges [109], buildings [110] and automobiles. The application of SHM goes beyond just the service life of the product into online monitoring during cure, repairs and post its design life [111]. The requirements for the sensors to qualify for SHM are: (i) robustness, (ii) resistance to service environment, (iii) accuracy and reliability, and above all (iv) low price and low power consumption. When the sensor is bonded to the substrate the sensor output becomes directly proportional to the surface displacement. Strain gauges are the most common SHM sensors, where the strain is measured as a variation of the resistance during operation. But their high power consumption is luring the SHM industry towards self-powered piezoelectric sensors. Utilization of PVDF further enables shape sizing and conforming the structure along with the ability to be used in high strain conditions as compared to the ceramics. PVDF’s low acoustic impedance and flat response over wide range of frequencies further supports its applicability.

SHM sensors can be glued or embedded into the structure as seen in Figure 2.22 [112]. Sensor incorporation into the structure though adds in more complexity into the fabrication process but improves the robustness and life of the sensor. One disadvantage with embedded sensors can be their replacement upon damage.

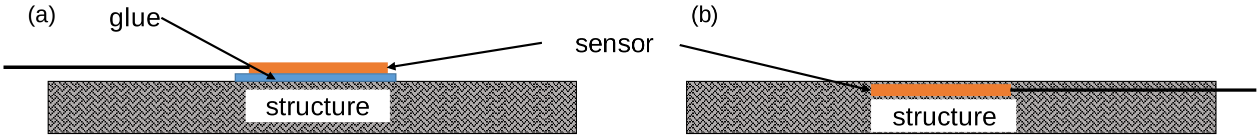

Figure 2.22: Schematic of SHM sensor placement: (a) sensor glued on the structure surface post-fabrication; (b) sensor incorporated into the structure during fabrication.

PVDF sensors in SHM

Traditionally PVDF sensors used for composite monitoring are embedded during the hand-layup process [112] or glued on top. An importance aspect to consider while using conductive structures is to well-insulate the leads from the PVDF sensor in order to avoid any short-circuit in the structure. Table 2.4 is a brief insight into the ways towards PVDF sensor incorporation and a whole lot of sensed physical quantities. Most of the applications use commercially available PVDF films. The application of 3D printing to embed or attach PVDF sensors on top of structures is not found to date.

Table 2-4: List of applications of PVDF sensor for SHM

Material	Sensor incorporation technique	Sensed quantity	Damage detection of:	Ref.
PVDF film (MEAS)	gluing	strain	buildings	[110]
PVDF film (spin coated)	pasted and embedded into the wing	lift	micro-air vehicles	[113]
PVDF film (Tokyo Sensor co.)	gluing	strain	civil structures (metals and concrete)	
PVDF film (MEAS)	(i) glued; (ii) embedded	elastic properties through natural frequency	aerospace structures	[112]
PVDF-TrFe sheet (Piezotech)	An array of sensors was attached on the surface of the cylinder	acoustic pressure	pressure vessels	[114]
PVDF film	bonded using epoxy	strain	aircraft structures	[111]

3D printing of SHM sensors

3D printing of SHM sensors comes with the advantages of ease of integration of the sensors with the sensed structures, reduction in manufacturing steps and the ability to place the sensors on both flat and curved features. To date only resistive sensors have been integrated into the structures via additive manufacturing techniques. In earlier attempts, Polyjet printing was used to fabricate "print-stick-peel" piezoeresistive silver ink based strain sensors [115]. Conductive silver nanoink based sensors are printed on PTFE/ PFA substrates and sintered to reach the desired conductivity. The sensors were stuck to the 3D printed structures mid-way during the print and then the printing was continued. This method was evolved to avoid the effect of sintering parameters on the 3D printed part to be monitored. Yao *et.al* [116], used carbon fiber as the resistive sensing element and simultaneously as a strengthening element for PLA in the fabrication via FDM

(Figure 2.23a) claiming a 26% weight reduction. Carbon fibers were readily embedded in the fingers of a PLA robotic arm (Figure 2.23b). The finger was placed in a tensile test set up and Figure 2.23c shows the change in resistance as the force is ramped from 0 to 200 N.

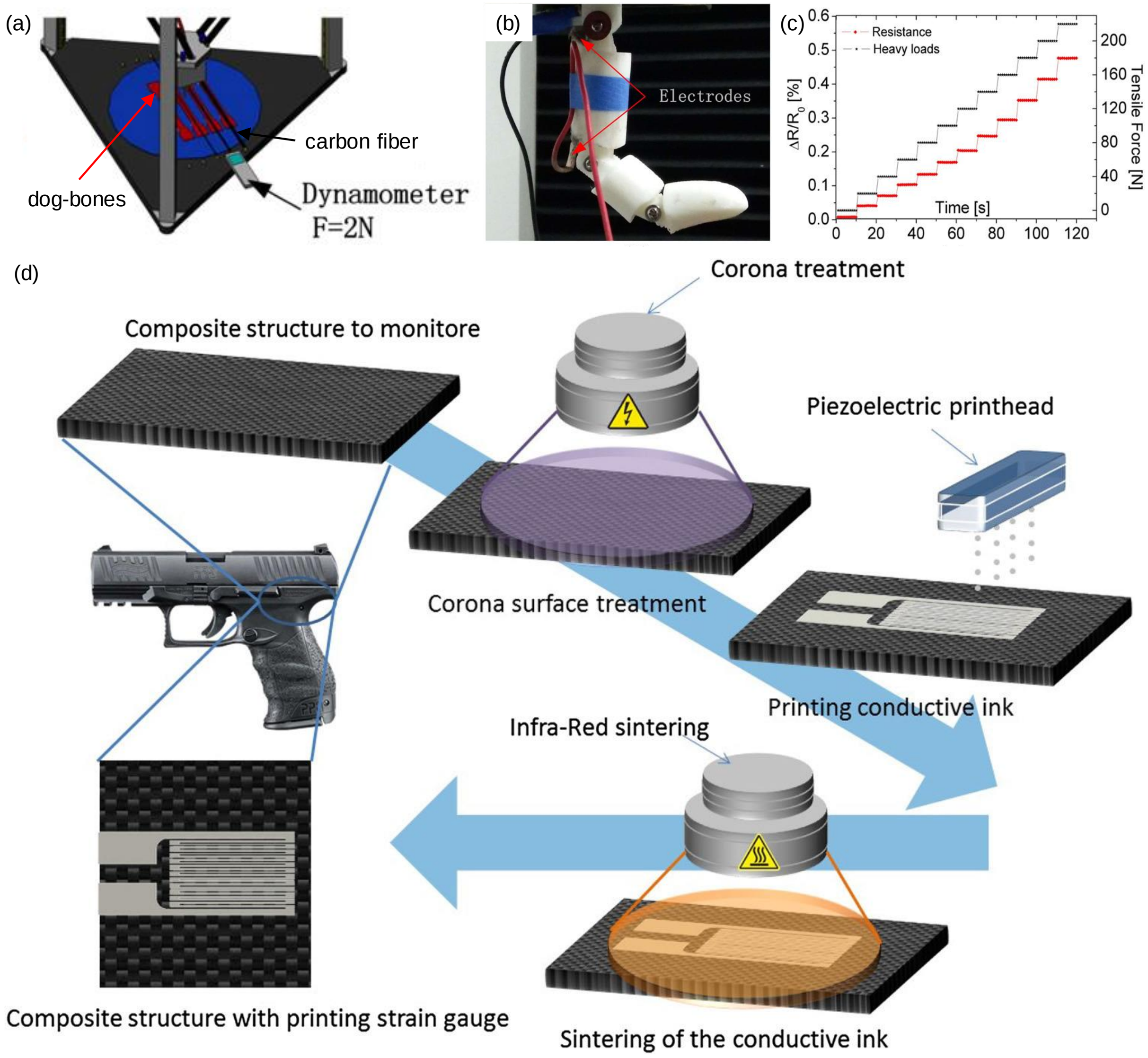

Figure 2.23: (a) Schematic of carbon-fiber placement and 3D printing dogbones via FDM; (b)a robotic finger fabricated via the technique shown in (a); (c) fractional change in the resistance as the tensile force applied on the finger is increased in steps [126]; and(d) ink-jet printing of silver ink based sensor near the trigger of a hand-gun [117]

In another attempt, silver ink based sensors were ink-jet printed at the gripping point of a hand-gun to monitor the pressure during a firing cycle [117] (Figure 2.23d). The 3D printed sensor outperformed a commercial strain sensor in acoustic pressure detection when compared with a microphone.

2.7. Summary of literature survey

PVDF is a promising piezoelectric polymer with advantages of high electromechanical coupling, flexibility and low density as compared to ceramics. Presently, PVDF is fabricated in the form of piezoelectric films or mats. There are a few processes catering to fiber fabrication but only at a very small scale. Poling at high voltages and addition of $BaTiO_3$ nanoparticles has shown to completely convert α-PVDF into β. Also, most steps in attaining higher degree of β-phase and polarization are quite inconvenient. This restricts the shapes that can be used for PVDF's applications to simple architectures. There is a need to fabricate 3D structures of piezoelectric materials with different sizes to cater to all the available frequencies of vibration in the vicinity of the energy harvesters [118]. Microscopic structures of PVDF, produced through conventional microfabrication techniques, have been restricted to layered features merely consisting of set of lines and simple planar architectures. Though there have been reports on the production of unidirectional filaments of PVDF, the methods used (e.g., near field electrospinning, melt-extrusion) are cumbersome and relatively expensive. It is proven that the smart properties of PVDF are better realized in extruded structures than solution cast films. If the concentration is placed just on the fabrication of 3D structures, it is impractical to carry out the post-processing steps required to achieve higher piezoelectric properties. This would restrict the application of PVDF to just a structural polymer. Therefore, there is a need to develop a system to fabricate multifunctional PVDF and its nanocomposites in a single step with electrodes and the required piezoelectric properties.

CHAPTER 3 RESEARCH OBJECTIVES AND COHERENCE OF ARTICLES

3.1 Research objectives

The principal objective of this research is to develop a single step process for the fabrication of 3D piezoelectric structures. This new process will expand the horizons of solvent-cast 3D printing approach to fabricate permanent dipole oriented PVDF structures along with electrodes to be directly used in microelectronics as sensors, actuators and power harvesters.

3.1.1 Specific objectives of the research

(i) **Adapt solvent-cast 3D printing technique to PVDF and its nanocomposites.** Prepare PVDF ink. Characterize rheological, morphological, mechanical properties and the β-phase in PVDF. 3D print PVDF. Prepare PVDF/$BatiO_3$ nanocomposites. Study the effect of PVDF concentration, extrusion pressure, rate of evaporation and filler concentration, nanocomposite fabrication techniques on the piezoelectric properties of the nanocomposites. Demonstrate a working 3D printed piezoelectric device.

(ii) **Improve the piezoelectric properties of the nanocomposite via simultaneous poling during printing.** Apply electric field during the printing process. Study the effect of different electric fields on PVDF and its nanocomposites on the piezoelectric properties of PVDF. Fabricate a working application of the technique in the form of gait monitoring sensors and demonstrate their ability to detect different kinds of gait.

(iii) **Develop advanced 3D printing capability for piezoelectric PVDF.** Co-fabricate electrodes using conductive inks to obtain piezoelectric devices in a single step. Develop working applications of this novel process. Use the co-extruded ink to 3D print sensors on substrates to be sensed.

3.2 Presentation of articles and coherence of research objectives

Chapter 4, 5 and 6 form the crucial back-bone of this thesis and are presented here in the form of accepted (Chapter 4) and submitted (Chapter 5 and 6) peer-reviewed journal articles accompanied by two peer reviewed conference proceedings (Proceeding papers, Appendix). These articles complete the research objective: 1, 2 and 3 stated in section 3.1 as described below in detail.

Chapter 4 presents the first article, "*One-Step Solvent Evaporation-Assisted 3D Printing of* Piezoelectric PVDF Nanocomposite Structures", published in Applied Materials and Interfaces (**DOI:** 10.1021/acsami.7b04095) (impact factor = 7.145). This journal was chosen because of its interdisciplinary nature and focus on innovative materials, interfacial processes and their affects on the applications. This paper was submitted on March 22, 2017 and was first published online on May 29, 2017. The work in this publication covers the first objective stated in 2.1. 3D printability was achieved for both PVDF and its nanocomposite with $BaTiO_3$ nanoparticles. The novel nanocomposite formulation fabricated in this work via ball-milling the nanoparticles with PVDF and extrusion at high pressures resulted in high piezoelectric properties enabling 3D printing of PVDF without the need for additional poling step. This furthers the 3D printability of PVDF by enabling the formation of embedded sensors in multimaterial 3D printing processes. The capabilities of this technique were demonstrated with a 3D cylindrical sensor that generates ten times higher voltage as compared to a film sensor with the same electrode area. Ms. Bodkhe designed and carried out the experiments, analyzed the data, and drafted the article under the supervision of Prof. Therriault and Prof. Gosselin. Ms. Turcot fabricated all the films and carried out the process-viscosity tests.

Chapter 5 presents the second article, "*In-situ Poling-assisted 3D Printing of Piezoelectric PVDF Nanocomposite Sensors for Gait Analysis,*" submitted to Journal of Materials Chemistry A (impact factor = 8.87). This journal was chosen as it publishes research production of materials related to energy storage and sensing, their modification and fabrication aspects. This article was submitted on 8th November 2017. The article corresponds to the second research objective of the thesis. Hence, it deals with the improvement in the piezoelectric properties of PVDF and its nanocomposites when 3D printed with simultaneous poling. Poling voltages from 0.1 to 1 $MV\ m^{-1}$ are used to study the impact of the applied electric field on the orientation of the dipoles in the polymer matrix. It is observed that both nanoparticle addition and electric poling enhanced the piezoelectric properties in PVDF. Poling-assisted 3D printing is demonstrated on a curved surface for the first time. Optimal selection of PVDF and the nanocomposite concentrations in the solvent system for the fabrication of 1D, 2D and 3D systems are explored. Application of this process is shown in the form of sensors directly printed on shoe insole for gait monitoring. Mr. Ponnada and

Ms. Bodkhe came up with the idea. Mr. Ponnada designed the set up for in-situ poling and helped in drafting the article. Ms. Bodkhe fabricated the all the sensors and the structures, designed and carried out the tests, analyzed the data and drafted the article under the supervision of Prof. Therriault and Prof. Gosselin.

Chapter 6 presents the third article, "*Coextrusion of Multifunctional Smart Sensors*", submitted to Nature Materials (impact factor = 39.74). This journal was chosen because of its multi-disciplinary nature and being at the edge of scientific research. This paper was submitted on 8th November 2017. This article includes the work satisfying the objective 3 of this thesis. PVDF nanocomposite developed in article 1 is coextruded with commercially available silver paint. Sensors are 3D printed with this system on various fused deposition modelling parts to show the applicability in multi-material printing. Applications of the sensors are presented in the form of piezoelectric thread for smart textiles and as integrated sensors for aero-elastic monitoring of miniature flapping wings. Ms. Bodkhe devised the new method, fabricated all the sensors and the structures, designed the experiments, carried out the experiments, analyzed the data and drafted the article under the supervision of Prof. Therriault and Prof. Gosselin. Ms. Noonan carried out the wearable sensors tests with the help of Ms. Bodkhe.

CHAPTER 4 ARTICLE 1: ONE-STEP SOLVENT EVAPORATION-ASSISTED 3D PRINTING OF PIEZOELECTRIC PVDF NANOCOMPOSITE STRUCTURES

Sampada Bodkhe, Gabrielle Turcot, Frederick P. Gosselin, and Daniel Therriault*

Laboratory for Multiscale Mechanics, Department of Mechanical Engineering, Centre for Applied Research on Polymers and Composites (CREPEC), Polytechnique Montreal, C.P. 6079, succ. Centre-Ville, Montreal, QC H3C 3A7, Canada, Applied Materials and Interfaces, May 29 2017.

Abstract

Development of a 3D printable material system possessing inherent piezoelectric properties to fabricate integrable sensors in a single-step printing process without poling is of importance to the creation of a wide variety of smart structures. Here, we study the effect of addition of barium titanate nanoparticles in nucleating piezoelectric β-polymorph in 3D printable polyvinylidene fluoride (PVDF) and fabrication of the layer-by-layer and self-supporting piezoelectric structures on a micro- to millimeter scale by solvent evaporation-assisted 3D printing at room temperature. The nanocomposite formulation obtained after a comprehensive investigation of composition and processing techniques possesses a piezoelectric coefficient, d_{31}, of 18 pC N^{-1}, which is comparable to that of typical poled and stretched commercial PVDF film sensors. A 3D contact sensor that generates up to 4 V upon gentle finger taps demonstrates the efficacy of the fabrication technique. Our one-step 3D printing of piezoelectric nanocomposites can form ready-to-use, complex-shaped, flexible, and lightweight piezoelectric devices. When combined with other 3D printable materials, they could serve as stand-alone or embedded sensors in aerospace, biomedicine, and robotic applications.

Keywords

3D printing, barium titanate nanoparticles, piezoelectric, polyvinylidene fluoride, sensors

4.1 Introduction

Polyvinylidene fluoride (PVDF) is the most piezoelectric polymer. Although PVDF's piezoelectric properties are lower than those of ceramics, it scores over them in terms of the inherent advantages of biocompatibility, toughness, flexibility, formability, and higher fatigue life [1]. Among the various crystalline phases of PVDF, the electroactive β-phase (all trans) with a planar zig-zag form [2] imparts the highest dipole moment, resulting in higher piezoelectric and ferroelectric constants. Unfortunately, PVDF commonly crystallizes into the thermodynamically stable non-polar α-phase upon solidification, which does not possess the desired piezoelectric properties. The attainment of β-phase thus requires either one or more physical transformations via application of heat (annealing) [3], large mechanical strain (stretching) [4-6], large electric fields (poling) [7, 8], or filler addition [9, 10]. Fillers like carbon nanotubes [11, 12], clay [13], cellulose [10], magnetic [14] and piezoelectric nanoparticles (NPs) [15] have proven to be very efficient in preventing the reversion of β-phase to α-phase upon solidification. Addition of eco-friendly and biocompatible [16, 17] piezoelectric ceramic filler - barium-titanate ($BaTiO_3$ NPs) [18-22] into PVDF has also shown to improve the ferro- and piezoelectric properties of PVDF without compromising its flexibility or strength. The incorporation of $BaTiO_3$ NPs into PVDF has been attempted so far via sonication [21, 23, 24] and ball-milling [25, 26] approaches.

Commercially available piezoelectric sensors essentially possess flat or fiber-like configurations and hence are limited to the use of single piezoelectric coefficient only for electromechanical coupling. Three-dimensional (3D) printing of piezoelectric materials benefits from improved electromechanical response extractable from 3D designs. Such an improvement stems from the synergistic augmentation of both accessible strain and coupling between both the in-plane and out-of-plane piezoelectric coefficients, thereby increasing the voltage output and consequently the sensitivity of the device [27].

For a piezoelectric sensor to be efficient, it will have to be integrated into the end-component. A multimaterial 3D printing process can result in elimination of the additional manufacturing step of sensor attachment, thereby serving as a long-term solution. In all the previously developed techniques for 3D printing of piezoelectric polymers such as fused deposition modelling of PVDF [28], optical printing of barium titanate ($BaTiO_3$) in a photoliable polymer [29], near-field electrospinning of PVDF [30, 31], poling still dominates as an obligatory treatment. Further, the requirement of poling can be envisaged as a hindrance to achieve simultaneous integration of piezoelectric sensors during a multimaterial 3D printing process. The concern is aggravated when the adjacent material or substrate properties are adversely affected by the poling conditions (e.g., degradation or melting of the polymer structure). Therefore, the removal of the poling step will not only simplify the printing process but also at the same time allow: (i) multimaterial printing, (ii) conformal printing on sensitive materials or systems, (iii) new opportunities for creating piezoelectric structures with complex configurations.

In this work, we engineered a nanocomposite formulation to attain a combination of printability and piezoelectric properties close to that of commercial PVDF films without the requirement of poling. To achieve the nanocomposite formulation, we compared three different methods: ball-milling, extrusion mixing, and sonication, to incorporate varying concentrations of $BaTiO_3$ NPs in PVDF. The ability of the nanoparticles to nucleate and further retain the β-phase in PVDF is studied through custom designed piezoelectric tests and available characterization techniques: scanning electron microscopy (SEM), X-ray diffractometry (XRD), Fourier transform infrared photo-acoustic spectroscopy (FTIR-PAS), and impedance spectroscopy. The formulation showing the best piezoelectric properties is then utilized to form micro- to millimeter scale 3D features via solvent evaporation-assisted 3D printing. The process involves the dissolution of the nanocomposite into a highly volatile solvent followed by extrusion through a small nozzle under applied pressure [32, 33]. The rapid evaporation of the solvent results in retention of the desired shapes: layer-by-layer, self-supporting, and even freestanding structures [32]. The application of our work is highlighted in the form of a ready-to-use millimeter scale 3D contact sensor fabricated in a single printing step.

4.2 Experimental Section

Methods

A mixture of acetone (BDH) and dimethylformamide (DMF; Alfa Aesar) was chosen as the solvent system for polyvinylidene fluoride (PVDF; Sigma-Aldrich). DMF is considered the least hazardous among the solvents used for PVDF and has a boiling point of about 153 °C.[139] On the other hand, acetone has a low boiling point (~56 °C) but cannot dissolve PVDF. The ratio of DMF:acetone was experimentally optimized to 40:60 to minimize the amount of DMF while facilitating a quicker shape retention during printing. Dimethyl sulfoxide (DMSO; Sigma-Aldrich; 65 g L^{-1}) was added as a β-phase initiating agent [35]. PVDF (2 g) was sonicated with DMF (4 mL), acetone (6 mL), and DMSO (0.6 mL) for 20 min to form a 0.2 g mL^{-1} solution for printing. A similar solution was also used to fabricate a solution cast film for comparison.

Barium titanate nanocomposite preparation (0.2 g mL^{-1} nanocomposite in the solvent mixture)

Ball-mill mixing: A mixture of Barium titanate NPs ($BaTiO_3$; 99.9% purity, 100 nm; Nanostructured & Amorphous Materials Inc.; 0.2 g) and PVDF (2 g) was sonicated in DMF for 2 h. The solution was then mixed in a high energy shaker ball-mill (SPEX SamplePrep 8000 Series Mixer/Mill) at a rate of 1080 cycles per minute for 20 minutes. The number of zirconia balls for milling was chosen to match the weight of the solution. The solution was dried in a vacuum oven at 60 °C for 12 h to remove all the DMF. The dry nanocomposite (2 g) was later sonicated with DMF (4 mL), acetone (6 mL), and DMSO (0.6 mL) until complete dissolution of the nanocomposite was achieved. For apparent viscosity tests and printing 3D structures, 2.5 g and 3.0 g of the nanocomposite were dissolved to form 0.25 and 0.3 g mL^{-1} solutions, respectively.

Extrusion mixing: A mixture of $BaTiO_3$ NPs (0.2 g) and PVDF (2 g) was fed into a 5 mL twin screw microextruder (Xplore) at 185 °C and mixed for 5 min. A temperature of 185 °C was maintained above the melting point of PVDF (T_m = 171 °C) [36] at both the inlet and exit of the extruder. The screw speed was 200 rpm. The mixture of PVDF and the NPs (2 g) obtained in the form of the filaments from the extruder was sonicated with a mixture of DMF (4 mL), acetone (6 mL), and DMSO (0.6 mL) until complete dissolution of the nanocomposite was achieved.

Sonication: $BaTiO_3$ NPs (0.18 g) were added to DMF (4 mL) and sonicated for 3 h to achieve complete dispersion. PVDF (1.8 g) was completely dispersed separately in acetone (6 mL) via sonication. The two solutions were mixed, and DMSO (0.6 mL) was added and sonicated for 20 min.

Solvent evaporation-assisted 3D printing

PVDF and its nanocomposite solutions were poured into a syringe (3 mL) and placed into a pneumatically operated dispensing system (HP-7X, EFD) to apply precise pressures for printing, as depicted in Figure 4.1a. This dispensing system was mounted on a robotic head (I&J2200-4,

I&J Fisnar Inc.) controlled by a commercial software (JR Points for Dispensing, Janome Sewing Machine) that further enabled the deposition of the inks on a movable stage. The geometry of the profile to be printed was communicated to the robotic arm as a series of coordinates through the software. The air pressure from the dispenser forced the material out of the syringe through a nozzle. As the material escaped the nozzle, the evaporation of the solvents provides rigidity to retain the designed geometry. To fabricate one-dimensional (1D) filaments, two-dimensional (2D) films, and 3D layer-by-layer and self-supporting structures, different solution concentrations (0.2, 0.25, and 0.3 g mL^{-1}) were used with a metallic nozzle (inner diameter = 100 µm) and varying extrusion pressures, P (0.1 to 2 MPa) and robot speeds (0.5 – 20 mm s^{-1}). While fabricating films, the concentration of nanocomposite in the solvent mixture was kept at 0.2 g mL^{-1} and the printing parameters were as follows, unless mentioned otherwise: nozzle inner diameter = 100 µm; P ~ 1 MPa; robot speed = 20 mm s^{-1}.

Characterization

To fabricate the sensors, a thin conductive electrode layer was painted on both sides of the printed nano-composite films and the internal and external surfaces of the 3D cylinder with commercially available conductive silver paste (Sigma-Aldrich). Electrical connections were made using a conducting aluminum tape (3M).

To determine the linearity of the sensors, a dynamic mechanical analyzer (DMA; Q800; TA instruments) was further used in a single frequency (45 Hz) tension mode with a multi-stress force ramp of 0.1 N until fracture (rate of 0.5 N min^{-1}). The sensors consisting of films (20 × 5 × 0.1 mm) with electrodes (10 × 5 mm) were used with a grip separation of ~ 10 mm. Three samples were tested for each concentration of 5, 10, and 15 wt.% of NPs in the nanocomposites. Piezoelectric charges obtained from all the sensors were converted into voltages using a charge amplifier (Piezo lab amplifier, MEAS Specialties) in charge mode acquired with an NI-9239 data acquisition system attached to a USB carrier NI-9162 (National Instruments) and recorded using a LabVIEW interface.

To obtain the diffractogram patterns of the films, a Philips X'pert diffractometer was used with scan angles from 10° to 50°. A scan rate of 0.4 ° min^{-1} was used with a Cu target and K_α radiation of 50 kV and 40 mA. FTIR-PAS (FTS 6000 spectrometer, Biorad) was used to obtain the absorption spectra of PVDF and its nanocomposite films in the range of 500 – 4000 cm^{-1}. 128 scans were conducted on each sample with a resolution value of 8 cm^{-1}.

For viscosity characterization, five identical filaments were printed (nozzle diameter = 100 µm; speed = 0.5 mm s^{-1}; printing time =120 s) at different pressures (0.1 – 2 MPa) using 0.20, 0.25, and 0.30 g mL^{-1} of ball-milled PVDF/ $BaTiO_3$ nanocomposite in the solvent mixture. End effects were neglected as the length to diameter (*L/D*) ratio of the nozzle was greater than 50 [142]. The weights of the filaments were determined after 48 h to ensure complete evaporation of solvents. Mass flow-rates were calculated by reverting to the original mass before solvent evaporation. The apparent viscosity calculation details are provided in the Supporting Information and in Bruneaux et al [38].

To image structures printed with the nanocomposites, optical microscopy (BX-61 Olympus microscope; Image-Pro plus V5, an image processing software from Media Cybernetics) was used. The morphology and cross-sections of the 3D printed films and structures were observed using a field emission scanning electron microscope (FE-SEM; JEOL JSM-7600TFE). A SEM (JEOL JSM 840) was used to obtain the images of the 3D printed structures at lower magnifications. Both SEMs were operated at an accelerating voltage of 10 kV. For viewing the cross-sections, the fibers and films were fractured in liquid nitrogen. All of the structures and films were gold-coated before imaging.

4.3 Results and Discussion

Figure 4.1(a) is a schematic of the one-step solvent evaporation-assisted 3D printing of a piezoelectric nanocomposite contact sensor. The 70-layer cylindrical sensor shown in Figure 4.1b was printed with 0.25 g mL^{-1} of 10 wt.% $BaTiO_3$ NP ball-milled nanocomposite solution. The programmed diameter and height of the cylinder were 5 and 7 mm, respectively. After solvent evaporation, the printed cylinder shrunk to ~ 3.1 mm in both height and outer diameter. The 3D contact sensor was used right after printing without the need for a poling step. The sensor was gently tapped with a forefinger (Figure 4.1(b)) five times consecutively, and the generated signal can be seen in Figure 4.1(c). The sensor produced a consistent maximum voltage output of ~ 4 V for touching and ~ -2 V upon releasing (see Figure 4.12 for the detailed mechanism). The 3D sensor produced voltage approximately ten times higher than that of a film sensor of the same electrode surface area (Figure 4.15). The high voltage outputs from the 3D sensor presented here result from the improved inherent piezoelectric properties of PVDF by extrusion-based printing and the addition of $BaTiO_3$ NPs. The contribution from interfacial charges to the response of the 3D sensor can be neglected as both the filler and the polymer used in this case are dielectrics [39], and nanoscale particles have a negligible contribution towards Maxwell-Wagner effects [40]. Literature also suggests that addition of pristine $BaTiO_3$ nanoparticles to PVDF does not result in interfacial polarization [41].

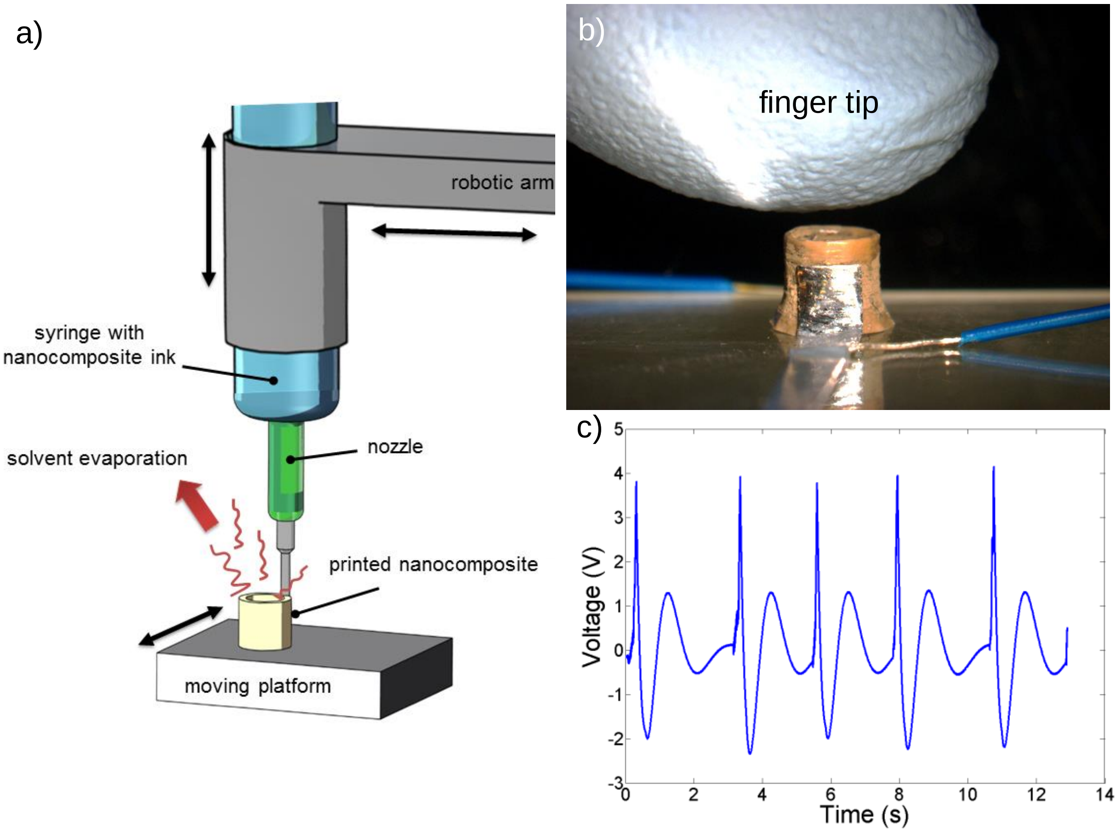

Figure 4.1: (a) Solvent evaporation-assisted 3D printing process for PVDF nanocomposite-based 3D structures. (b) Photograph of the 3D cylindrical sensor during a finger-tap test. (c) Piezoelectric voltage output of the 3D cylindrical sensor upon five consecutive finger taps

In the following paragraphs, the effect of four parameters on the piezoelectric properties of PVDF are investigated: (i) extrusion-based printing, (ii) filler addition, (iii) processing techniques, and finally (iv) filler concentration. We use XRD and FTIR-PAS to study the effect of solvent evaporation-assisted 3D printing of PVDF on the conversion of its α-phase into β-phase [42]. The XRD patterns of solution-cast and 3D printed PVDF films prepared by using 0.20 g mL^{-1} PVDF in the solvent mixture can be observed in Figure 4.2(a). Peaks pertaining to the α-phase of PVDF at 18.70º, 20.04º and 26.50º are clearly visible in case of the film fabricated via solution casting route [13, 43], whereas a single distinct peak at 20.26º corresponding to the β-phase confirms the effect of the extrusion pressures in the attainment of β-phase. As the polymer chains come out of the nozzle, the extrusion pressure of ~1 MPa leads to the significant phase transformation, and the passage through the relatively long slender nozzle (12.7 mm; *L/D* ratio = 127) can align the polymer chains. We then carried out FTIR on the two kinds of films discussed above. Bands at 763 and 974 cm^{-1} are known to represent the presence of α-phase, and those at 512, 840, and 1279 cm^{-1} the β-phase in PVDF [44-46]. As seen from a large drop in absorbance at ~763 cm^{-1} in Figure 4.2(b), the fraction of β-phase, *F(β),* considerably increased upon 3D

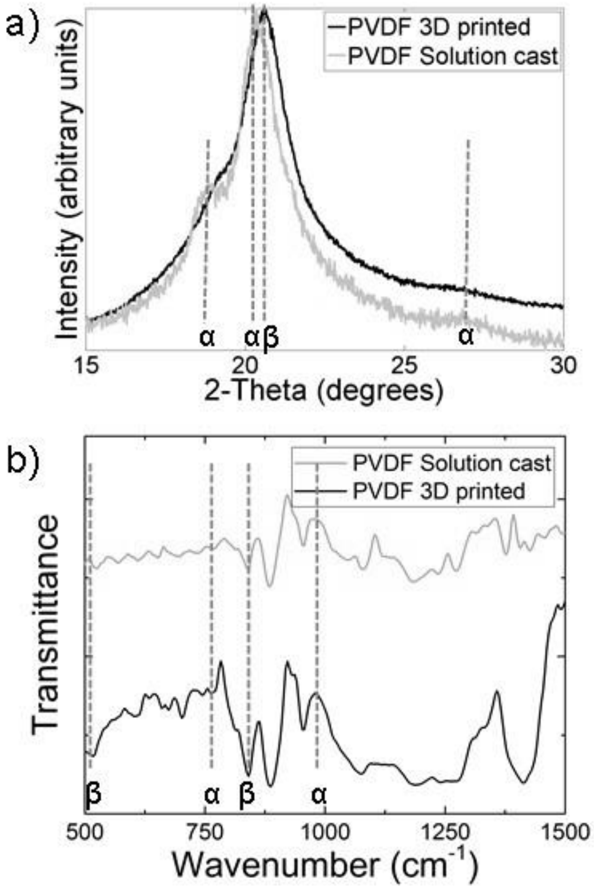

Figure 4.2: (a) X-ray diffractogram and (b) FTIR curves of 3D printed and solution-cast neat PVDF films (0.2 g mL^{-1} of PVDF in solvents). The characteristic peaks of the two phases of PVDF are labeled with their respective symbols α and β (printing parameters: ~1 MPa at 20 mm s^{-1} with a 100 µm nozzle)

printing. The *F(β)* in the 3D printed film (64%), calculated using Beer-Lambert's law (Equation 4.2), was found to be ~30 % higher than that in the solution-cast film (49%).

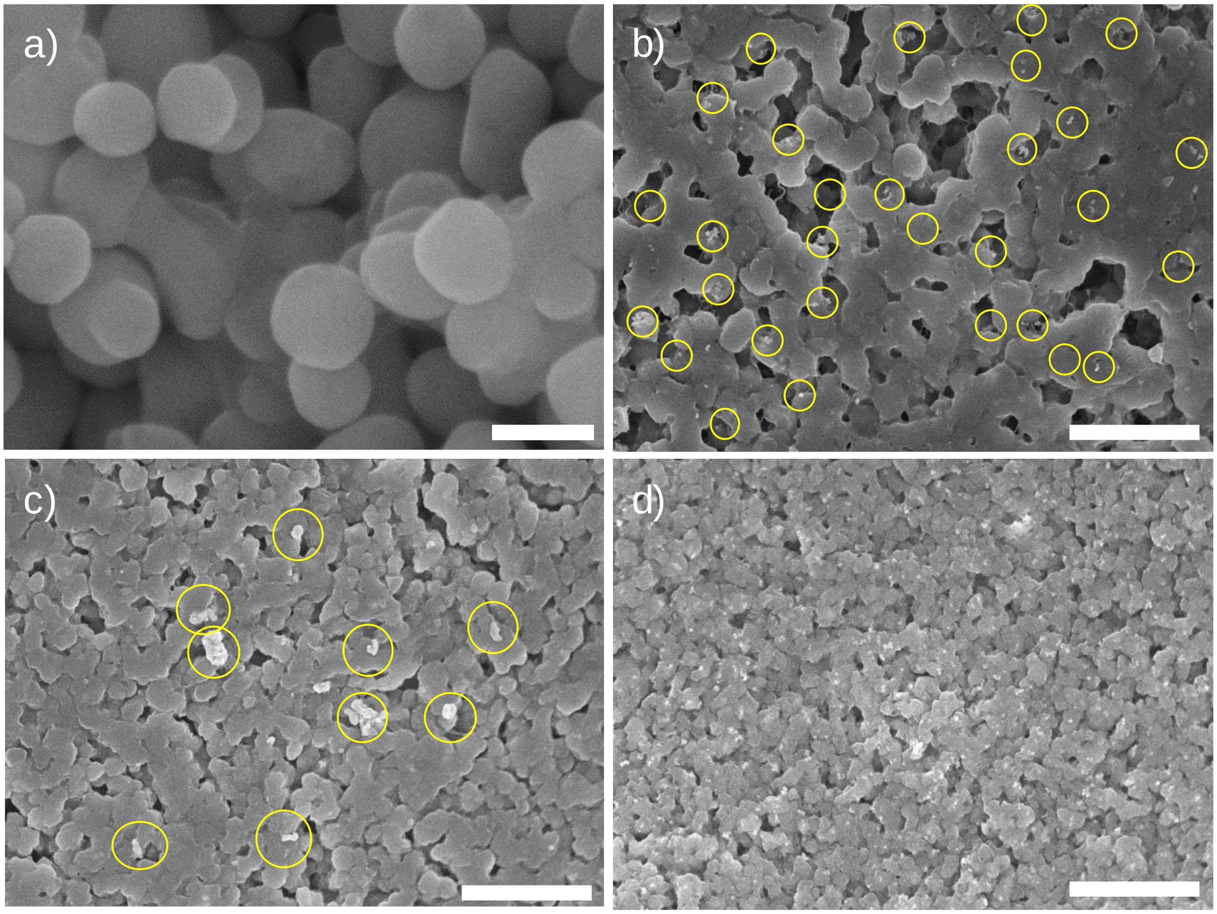

Figure 4.3: (a) SEM image of BaTiO3 NPs (scale bar = 100 nm). SEM images of surfaces of films fabricated from the 0.2 g mL-1 solutions of nanocomposites prepared by (b) ball-milling, (c) extrusion, and (d) sonication (scale bars = 5 µm). Yellow circles highlight the $BaTiO_3$ NP agglomerates (printing parameters: ~1 MPa at 20 mm s^{-1} with a 100 µm nozzle)

To further improve the *F(β)* in PVDF, we incorporated 10 wt.% $BaTiO_3$ NPs into the PVDF matrix. We compared three mixing methods—ball-milling, extrusion, and sonication—to determine which one had the most favorable impact on the piezoelectric voltage outputs resulting from the application of a dynamic mechanical load using the DMA. As the film-based sensors were subjected to longitudinal loads (direction 1), charges were generated across the thickness (direction 3) of the film (Figure 4.11c). The maximum voltage output was obtained with the sensors fabricated from the ball-milled nanocomposites (Figure 4.12a). For these sensors, the peak-to-peak voltage saturated at 6 V for frequencies higher than 35 Hz. In comparison, the sensors fabricated by extrusion and sonication failed to give outputs distinguishable from the noise. In addition, there was no voltage output from a sensor fabricated by ball-mill mixing of 10 wt.% $BaTiO_3$ NPs with polylactic acid (PLA), which ascertains the fact that this process works due to the enhancement of β-phase in PVDF and not due to the piezoelectric properties of the NPs. Additionally, $BaTiO_3$ is ferroelectric in nature and rendered piezoelectric only upon electric poling. This strengthens the fact that the piezoelectric response obtained in our material is purely from PVDF and has no contribution from the nanoparticles [47].

We employed SEM and XRD characterization to understand why solely the ball-milled nanocomposites exhibited piezoelectricity. Figure 4.3(a) shows SEM image of $BaTiO_3$ NPs. The size of the NPs varies between 80 and 100 nm. The SEM images in Figure 3b-d show the morphology of the nanocomposites films. In the case of ball-milled nanocomposites (Figure 3b), large crystallites and pore sizes reveal higher crystal growth; a uniform dispersion of nanoparticle agglomerates (highlighted by circles) is also seen. It has been reported that dispersed agglomerates of NPs lead to an increased space charge density which in turn leads to higher piezoelectric properties [48]. Non-uniformly distributed NP clusters are observed in the extruded nanocomposite (Figure 4.3(c)). There is more nucleation of crystallites in the sonicated nanocomposite (Figure 4.3(d)) as smaller spherulites are evident. Higher nucleation prohibits the growth of crystallites [9]. The uniform dispersion of nanoparticles (seen as tiny white dots) in the sonicated nanocomposite is possibly the reason for this higher nucleation. Large micrometer-sized pores are present throughout the surface (Figure 4.3(b)) and cross section (Figure 4.13) of ball-milled nanocomposite films, whereas internal pores are very small or absent in the extrusion-mixed and sonicated nanocomposites. The highly porous structure of ball-milled nanocomposites resulted in lower modulus as found by the mechanical tests (Figure 4.10b). Increased flexibility allows for soft sensor applications and reduced interference with sensed structures.

Figure 4.4(a) shows the X-ray diffractogram of the $BaTiO_3$ NPs with characteristic peaks of $BaTiO_3$ at 22.15º, 31.53º, 39º and 45º [49]. The splitting of peaks belonging to the (200) and (002) planes at ~45º indicates the presence of tetragonal crystal structure, which is essential for spontaneous polarization and thus, piezoelectricity [21, 47,50]. Figure 4.4(b) shows the X-ray diffractogram of PVDF nanocomposites prepared by ball-milling, extrusion, and sonication. In the nanocomposite prepared by the ball-milling approach, the peaks at 18.70º, 20.04º and 26.50º belonging to α-phase of PVDF are absent [13, 43]. The presence of a single broad peak at 2-theta value of 20.26° corresponding to the (200) and (110) planes of β-phase underscores the inference that nanocomposite films prepared by ball-milling approach crystallized only in β-phase. In the case of the samples prepared by sonication, visible α-peaks are found at 18.7° [13, 43]. A prominent α-peak at 40° and a γ-peak close to 26° is seen in the extrusion-mixed sample [156-158]. Uniformly dispersed individual nanoparticles in sonicated films were probably not as efficient as the agglomerates present in the ball-milled nanocomposites in preventing the reversion to α-phase during the crystallization process. High temperature shear during extrusion shifted the $BaTiO_3$ tetragonal peak at 45°, depicting a change from the tetragonal structure of $BaTiO_3$ to a non-piezoelectric cubic structure [54, 55]. This may be linked to the temperature used for melt-mixing, i.e. 185 °C, which is higher than the $BaTiO_3$'s Curie temperature of 120 °C.

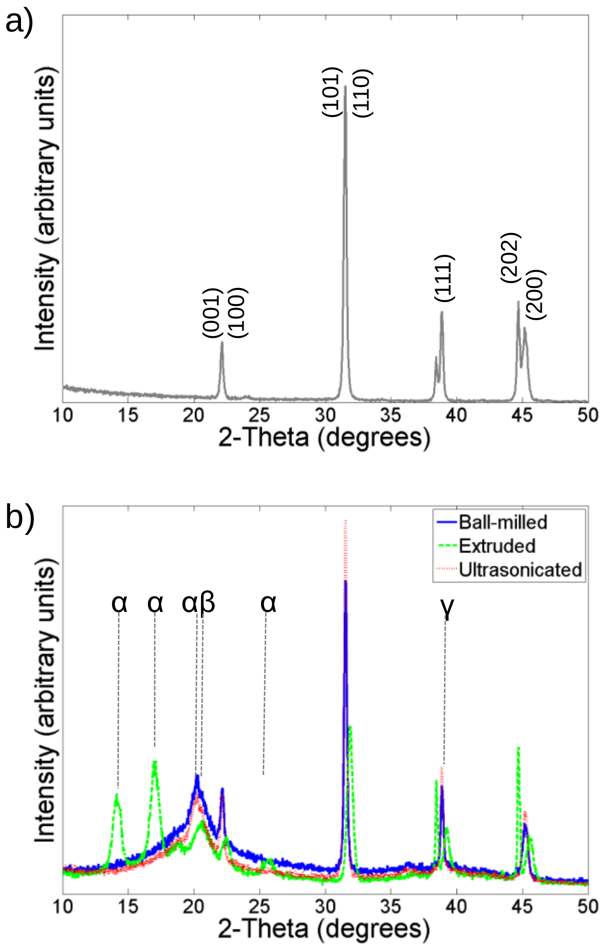

Figure 4.4: X-ray diffractogram of (a) $BaTiO_3$ NPs and (b) nanocomposites of 10 wt.% $BaTiO_3$ NPs and PVDF prepared by ball-milling, extrusion and sonication (printing parameters: ~1 MPa at 20 mm s^{-1} with a 100 μm nozzle)

[56]. As there is a change from non-centrosymmetric to a symmetric crystal lattice, the melt-mixed nanocomposites could not exhibit piezoelectricity. The properties of $BaTiO_3$ NPs seem to be unaltered by the ball-milling process as no change in their peak locations is observed.

After determining that ball-milling is the most appropriate mixing method in terms of piezoelectric properties, three different nanoparticle loadings (5, 10, and 15 wt.%) were investigated to determine the optimum filler weight fraction to fabricate 3D sensors. The voltage responses from the single frequency scans observed in Figure 4.5 are linear with the force until fracture, as should be the case with piezoelectric materials. The voltage outputs initially increased from 5 wt.% of $BaTiO_3$ to 10 wt.%. However, the nanocomposite sensors with 15 wt.% of the fillers exhibited no considerable output. A maximum peak-to-peak voltage around 2.8 V was obtained at a force of 2.7 N for the sensor with 10 wt.% fillers.

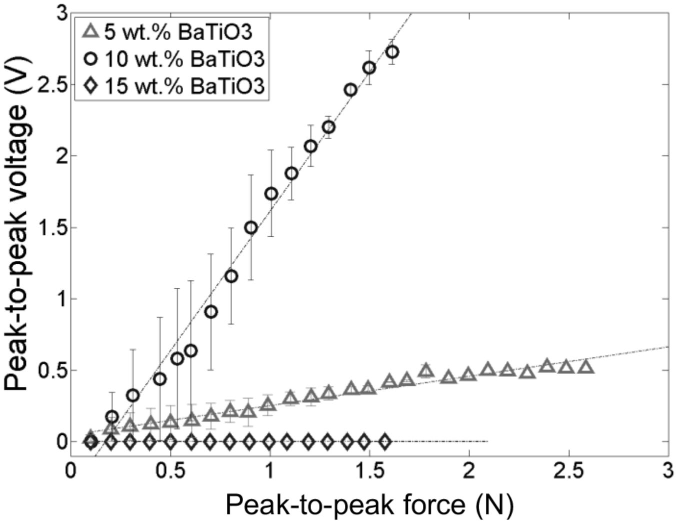

Figure 4.5: Peak-to-peak voltage as a function of peak force at an excitation frequency of 45 Hz for 5, 10, and 15 wt.% of $BaTiO_3$ NP addition to PVDF via ball-milling

Impedance spectroscopy was used to calculate the dielectric constants of the sensors. The nanocomposites with 10 wt.% NP loading possessed the highest dielectric constant of ~210 (Table S4.2). The piezoelectric coefficient is the ratio of electric field produced in a piezoelectric material to the applied stress. Average piezoelectric coefficients d_{31} = 2.5 and 18 pC N^{-1} were obtained for ball-milled nanocomposite sensors with 5 and 10 wt.% $BaTiO_3$ NPs, respectively (calculated using the voltage values as in Figure 4.5 and Equation 4.1). The value of 18 pC N^{-1}, obtained here without any poling is comparable to that of typical commercial stretched and poled PVDF-based film sensors (23 pC N^{-1}) [57].

We further use the results from SEM, XRD, and FTIR to understand the performance of our ball-milled nanocomposites. Figure 4.6(a-c) are SEM images of 5, 10, and 15 wt.% of $BaTiO_3$ NPs in PVDF via ball-milling. Fewer number of agglomerates are found in the case of the 5 wt.% loading compared to that found in the 10 wt.%. Although the number of agglomerates is increased in the 15 wt.% loading, their average size is almost halved in comparison to the 10 wt.% loading. This establishes that there has to be an optimum size and number of agglomerates to effectively prevent the reversion to α-phase. The XRD results (Figure S4.5) depicted that the films prepared with 10 wt.% NP loading exhibited no other phases than β-phase, while the other two films crystallized additionally in α- or γ-phase or both.

FTIR-PAS was employed to explain the difference between the piezoelectric constants of the 5 and 10 wt.% nanocomposites. Figure 4.6d shows the FTIR spectra of the 5 and 10 wt.% ball-milled nanocomposite films. A clear decrease in the content of α-phase can be observed in the curve pertaining to 10 wt.% nanoparticle loading. Beer-Lambert's law was used to quantify this difference in the amount of the two phases in the nanocomposites. The $F(\beta)$ present in the 5 and 10 wt.% ball-milled nanocomposites was 68 and 78%, respectively (Equation 4.2). The higher value of $F(\beta)$ in the 10 wt.% nanocomposites explains the improved response and higher piezoelectric coefficient value. The Beer-Lambert law could not be applied to the 15 wt.% loaded nanocomposite (data not shown) due to the presence of additional γ-phase as seen from the XRD (Figure 4.14).

Piezoelectric fillers do not contribute to the overall piezoelectricity of the nanocomposite when used in very small quantities, which was the case until 10 wt.% loading [58]. Hence, the increased presence of β-phase in PVDF upon the addition of 10 wt.% NPs via ball-milling is attributed to the mechanical activation of the NPs and their dispersed agglomerates, leading to an increased dipole moment [26, 48]. Further, given that the piezoelectric coefficients of the filler and the polymer have different signs, poling in a single direction would cancel out the d_{31} coefficients [59].

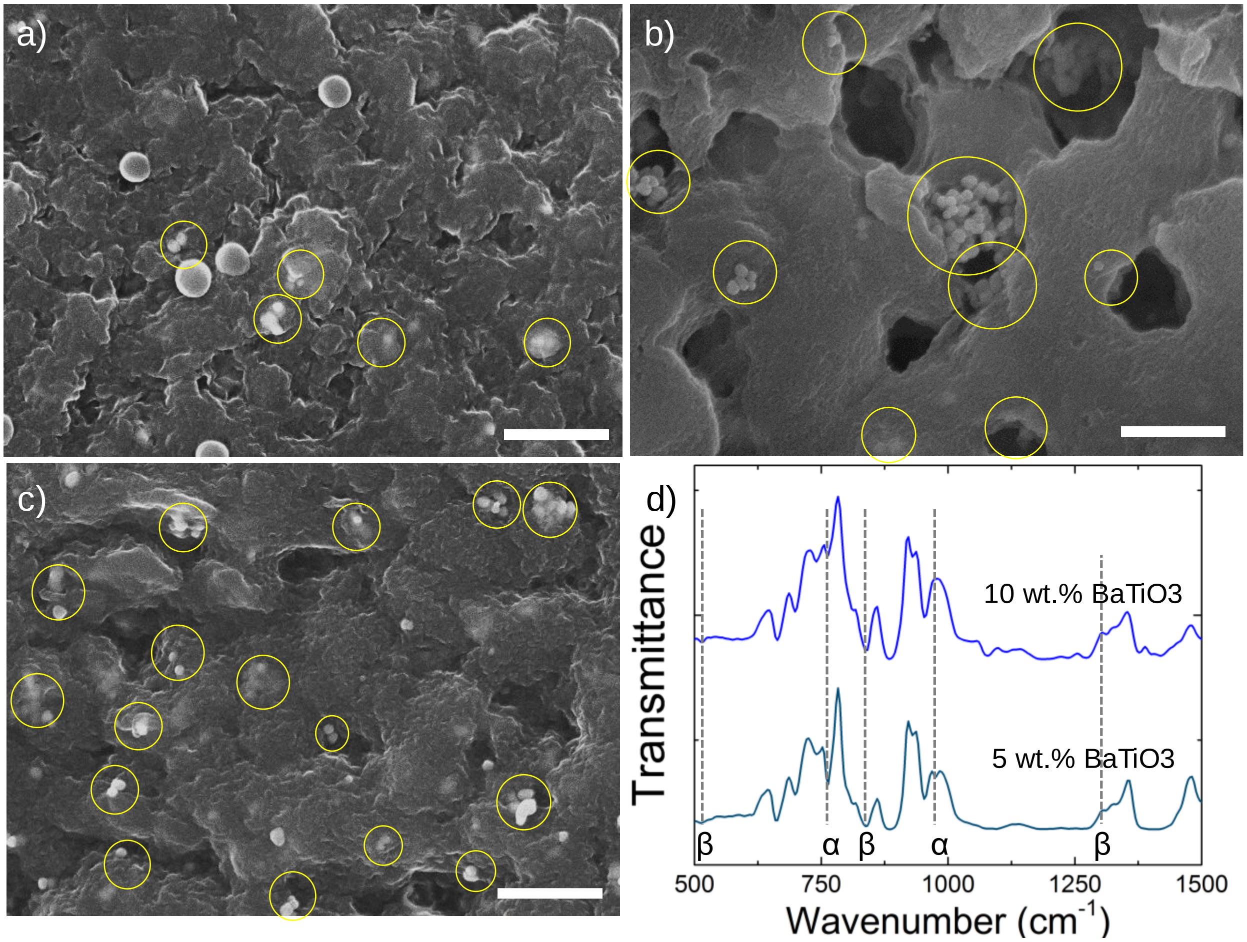

Figure 4.6: SEM image of surfaces of films fabricated from the 0.2 g mL-1 ball-milled nanocomposite solutions of (a) 5 wt.% $BaTiO_3$/ 95 wt.% PVDF, (b) 10 wt.% $BaTiO_3$/ 90 wt.% PVDF, (c) 15 wt.% $BaTiO_3$/ 85 wt.% PVDF (scale bar = 1 µm). Yellow circles highlight $BaTiO_3$ NP agglomerates; (d) FTIR curves of 5 wt.% $BaTiO_3$/ 95 wt.% PVDF and 10 wt.% $BaTiO_3$/ 90 wt.% PVDF (printing parameters: ~1 MPa at 20 mm s^{-1} with a 100 µm nozzle)

Hence, our approach to orient dipoles without the application of any electric field serves to improve the inherent piezoelectric properties in PVDF at low mass fraction. Lower effective Young's modulus in the case of the ball-milled nanocomposites as compared to that in the other two nanocomposites (Figure 4.10b) resulted in increased sensitivity.[60] However, as the process relies on improving the inherent piezoelectric properties of the polymer, factors such as humidity, temperature, print directions, speeds, and pressures can have a strong effect on the properties and hence reproducibility. Thus, efforts are being made to optimize these parameters and will form a part of our future work.

We propose the following hypothesis to summarize the process of formation of aligned β-phase chains during 3D printing. As seen in Figure 4.7, the addition of $BaTiO_3$ NPs to PVDF via ball-milling led to increased activation sites [61,62] on the NPs acting as β-phase nucleating sites because of the strong O–H···F–C hydrogen interaction at the PVDF/$BaTiO_3$ interfaces [63]. These interactions combined with the dipolar interactions of polar DMF and PVDF resulted in CH_2–CF_2 dipoles as in the case of all trans structure of β-phase. Moreover, the dipole alignment in our work is attained through mechanical means and not from conventional electrical poling [64]. The extensional flow of the solution resulted in the required chain and dipole alignment [65, 66]. Indeed, the high pressures (~1 MPa) during the passage through the fine nozzle with a

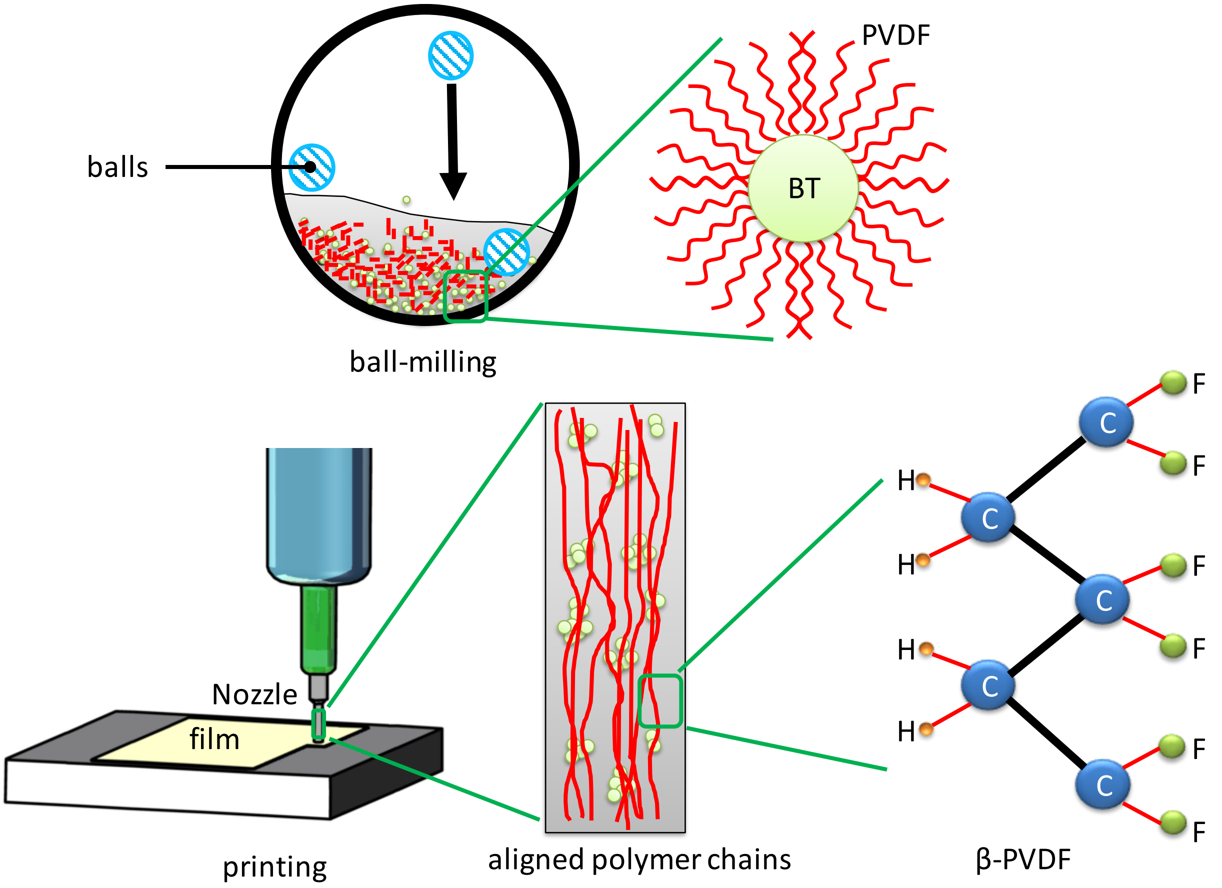

Figure 4.7: Schematic of the proposed process leading to increase in β-phase fraction in PVDF due to filler addition. Ball-mill mechanically activates the $BaTiO_3$ NPs (BT), which provides adhesion sites for PVDF chains. The polymer chains crystallize into aligned β-phase upon extrusion through the nozzle. The NP agglomerates arrest the PVDF chains in the β-phase upon solidification, thus leading to improved piezoelectric properties

high *L/D* ratio (~120) and post-extrusion stretching due to higher velocities of the robotic motion (~20 mm s^{-1}) contributed to align the PVDF polymer chains. The sub-micron sized agglomerates further prevented any chances of reversion to α-phase [40]. In the absence of electric poling, the ferroelectric $BaTiO_3$ NPs could not contribute to the improved piezoelectricity.

The shape and thickness of the extruded material from the nozzle during the printing process predominantly depends on the relationship between the applied pressure and the relative velocity of the robotic arm over the stage. Thus, to attain the required geometry, it is essential to arrive at the optimal relationship between the extrusion pressure and the velocity of the arm movement via a rheological analysis [33]. Rheological characterization allows us to establish the dependence of apparent viscosity on the extrusion pressure and the printing speed. The former is proportional to the shear stress at the wall, whereas the latter relates to the shear rate during the printing process.

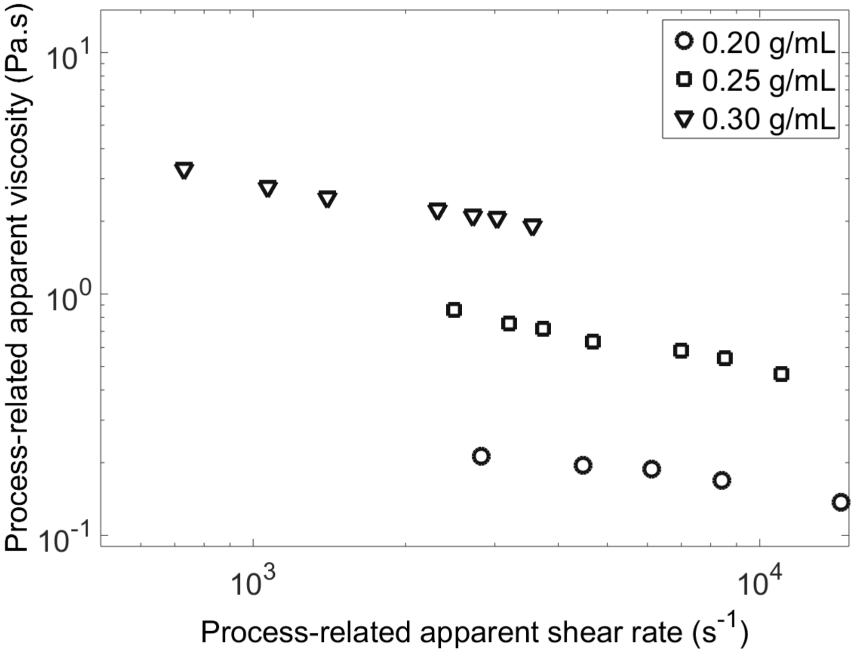

Figure 4.8: Viscosity as a function of shear rate during the printing process for 0.20, 0.25, and 0.30 g mL^{-1} of the ball-milled nanocomposite with 10 wt.% BaTiO3 NPs (printing parameters: 0.5 mm s^{-1} with a 100 µm nozzle)

Figure 4.8 shows the process-related viscosity as a function of the applied shear rates. The viscosity range for the three different concentrations (0.2, 0.25, and 0.3 g mL^{-1} of ball-milled PVDF/ $BaTiO_3$ nanocomposite) is found to be between 0.1 and 2.7 Pa s. The viscosity decreases with increasing shear rate, characteristic of a shear thinning behavior [67]. This property is essential for a material to be employed in extrusion-based printing processes. The optimal viscosity for a material is low enough to be extruded out of the small nozzle but at the same time high enough for shape retention after extrusion [68]. Thus, the rheological properties of the inks are well-suited for 3D printing. Moreover, it can be observed that the viscosity of the inks significantly increases with the concentration of the nanocomposites in the solutions aiding the fabrication of 3D self-supporting structures due to the increased rigidity.

The viscosity study aided in determining the optimum concentrations of the ball-milled PVDF nanocomposite required to obtain 1D, 2D, and 3D shapes, as shown in Figure 4.9. We can see a SEM image of the cross-section of a 1D filament (Figure 4.9(a)) extruded using 0.3 g mL^{-1} nanocomposite solution with a 100 µm nozzle at ~2.6 MPa. The average diameter of the fiber after complete evaporation of the solvents was about 56 ± 6 µm. The reduction in diameter of the fiber and the rough surface upon extrusion is attributed to evaporation of the solvents post-extrusion. A loading of 0.2 g mL^{-1} of nanocomposite in the solution mixture was observed to be optimal for printing 2D films and patterns without voids or gaps. A 2D pattern (LM2, Figure 4.9(b); the abbreviation of our laboratory) was printed using 0.2 g mL^{-1} solution with a pressure of ~0.11 MPa and robot velocity of 10 mm s^{-1}. A concentration of 0.25 g mL^{-1} facilitated the formation of 2.5D layer-by-layer structures: a circular cylinder (Figure 4.9(c)) printed at ~0.48 MPa and 1 mm s^{-1}. The cylinder has 70 layers and a programmed diameter and height of 5 and 7 mm, respectively. The concentration of 0.3 g mL^{-1} of the nanocomposite was best to print spanning or self-supported structures such as 3D scaffolds. A 9-layer scaffold (Figure 4.9(d)) was printed at ~1.3 MPa and 13 mm s^{-1} using a 100 µm nozzle with clearly distinguishable self-supporting filaments and individual layers. The spanning distance between two consecutive parallel filaments is 10 mm.

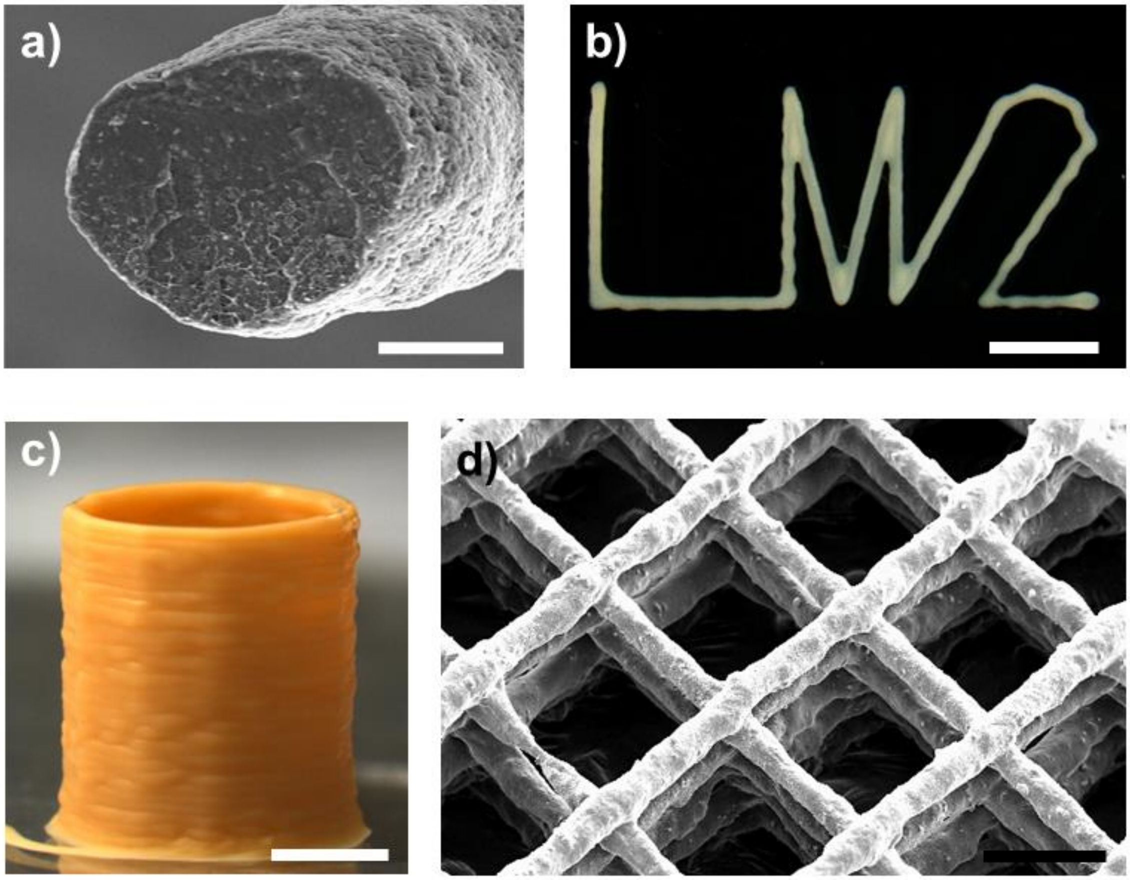

Figure 4.9: Structures fabricated using 10 wt.% $BaTiO_3$ ball-milled nanocomposite solution. (a) SEM image of cross-sectional view of a 1D fiber (scale bar = 25 µm). (b) Optical microscopy image of a 2D structure reading “LM2” (the abbreviation of the Laboratory for Multiscale Mechanics; scale bar = 2.5 mm). (c) Photograph of inclined side view of a 2.5D 70-layer circular cylinder (scale bar = 2 mm). (d) SEM image of inclined top-view of a 3D spanning 9-layer scaffold (scale bar = 0.5 mm)

4.4 Conclusion

Fusion of the solvent evaporation-assisted 3D printing and our piezoelectric material results in two critical achievements: (i) genesis and stabilization of electroactive β-phase, leading to remarkable sensing and actuation characteristics at room temperature, and (ii) optimized rheology to fabricate self-supporting structures with satisfactory mechanical robustness, all without the need for additional electromotive (poling) treatment. High dielectric and piezoelectric properties were obtained via 3D printing of a nanocomposite solution of 10 wt.% $BaTiO_3$ NPs ball-milled with PVDF due to the prevalence of β-phase. A piezoelectric coefficient of 18 pC N^{-1} comparable to that found in commercial PVDF sensors was obtained. A fully functional 3D printed sensor generating a maximum voltage output of up to 4 V upon finger tapping was fabricated and demonstrated. The one-step 3D printing of piezoelectric materials opens up a new demographic of sensor designs that is more integrable, conformable, scalable, versatile, and application-oriented. Apart from sensing, 3D piezoelectric scaffolds fabricated by the shown process could be used as electroactive scaffolds in tissue engineering [69], providing a biomimetic environment for cell culture. Given the limitation of the conventional electrode deposition techniques (forming planar electrodes), there is a need to develop a hybrid process to print the electrodes along with the polymer, thereby, delivering the entire sensor in a single step. The sensors produced in the single step could be used as hair-like sensors for aerodynamics, as embedded sensors in aerospace or biomedical prosthesis, and as filaments for smart textiles.

4.5 Acknowledgements

The authors acknowledge the financial support from NSERC (Natural Sciences and Engineering Research Council of Canada) and Canada Research Chair. The authors thank the Structures and Composites Materials Laboratory at McGill University for providing access to their DMA apparatus.

4.6 Mechanical tests with DMA

A dynamic mechanical analyser (DMA, Q800; TA instruments) was used in tension mode (Figure 4.10a) to investigate the maximum strain to be used for dynamic tests. Quasi static stress-strain tests with a controlled ramp force of 0.5 N min^{-1} were carried out on nanocomposite films (10 mm (grip separation) × 5 mm × 0.1-0.2 mm) prepared by the three mixing methods. Five samples were tested for each type of nanocomposite. The stress versus strain behaviour of each nanocomposite was determined to investigate the material stiffness and strength.

Figure 4.10b shows the averaged stress-strain curves for the three nanocomposites and neat PVDF films. Addition of fillers to PVDF resulted in decreased strength and strain at break. Nanocomposite samples prepared by both extrusion and sonication resulted in higher tensile strength as compared to ball-milled nanocomposites. The highest strength (8 MPa) and Young's

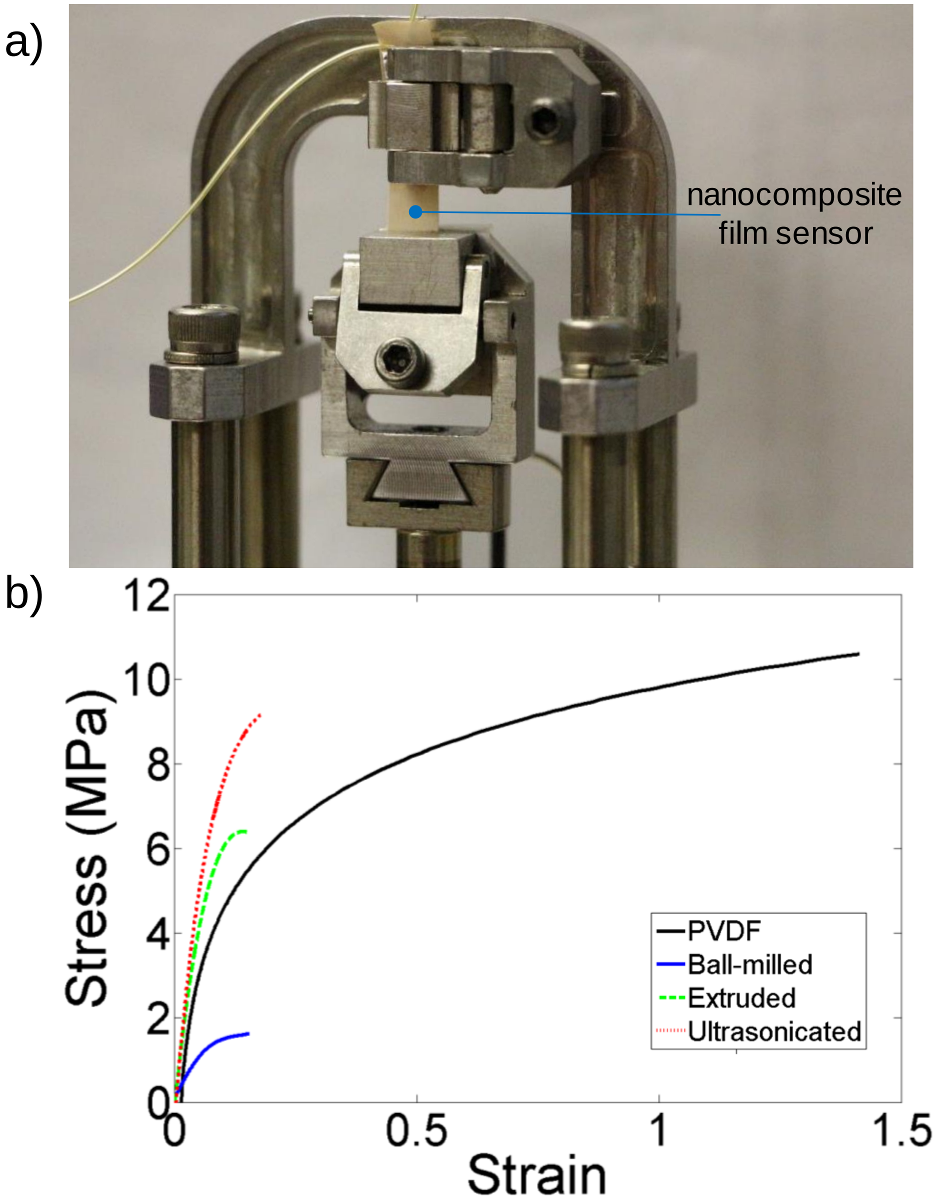

Figure 4.10: (a) Picture of the DMA used in tension mode with the nanocomposite test specimen. (b) Stress versus strain curves the nanocomposites prepared via ball-mill, extrusion and sonication mixing. The curve for PVDF can be seen in the inset

modulus (110 MPa) was obtained for the sonicated films attributed to the well-dispersed nanoparticles. Extrusion-mixed nanocomposites possessed intermediate properties (strength ~ 6.4 MPa, modulus ~ 98 MPa). The ball-milled nanocomposites in turn exhibited significantly lower strength (even lower than that of PVDF) of 1.8 MPa with a low Young's modulus of 23 MPa. The porous nature of the ball-milled nanocomposites lead to lower effective Young's modulus [60]. With a lower modulus, a material can have higher deformation for a specific stress and thus, allows the fabrication of sensors with lower structural influence on the sensed component they are placed upon, thereby increasing the strain transfer from the component to the sensor.

4.7 Multi-frequency piezoelectric tests with DMA

A thin electrode layer (as shown in Figure 4.11) was painted on both sides of the printed films with commercially available conductive silver paste (Sigma Aldrich) to fabricate a sensor. The thickness of the painted silver electrode was about 15-20 µm and that of the nanocomposite films ranged from 150-200 µm as seen from the SEM image in Figure 4.11. Painting of silver instead of printing aided in achieving a comparatively thinner layer of silver (hence flexible) as the high viscosity of the silver paste limited its printability.

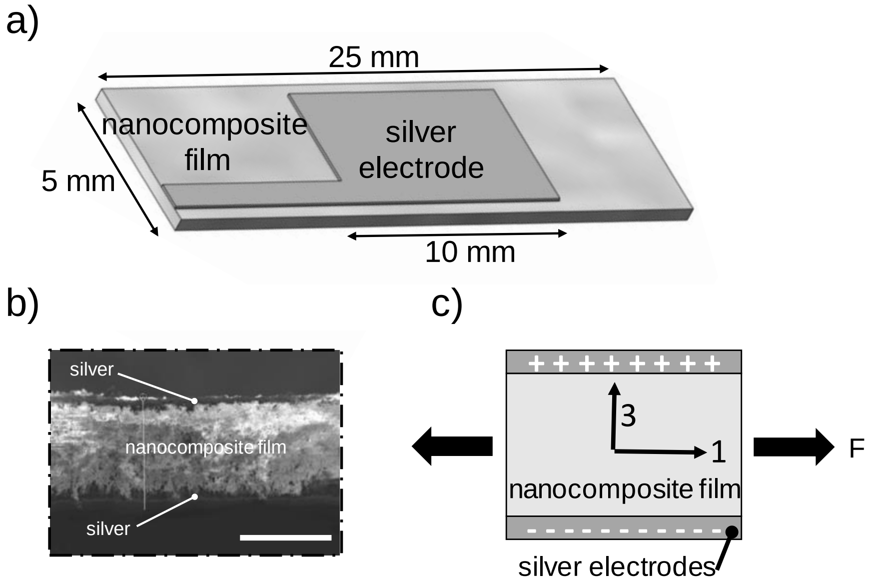

Figure 4.11: (a) Schematic of the sensor fabricated by painting silver electrode on the surfaces of the films. (b) SEM image of the cross-section of a representative nanocomposite sensor (scale bar = 200 µm). (c) Schematic of the phenomenon of charge generation in the sensor when subjected to forced excitation

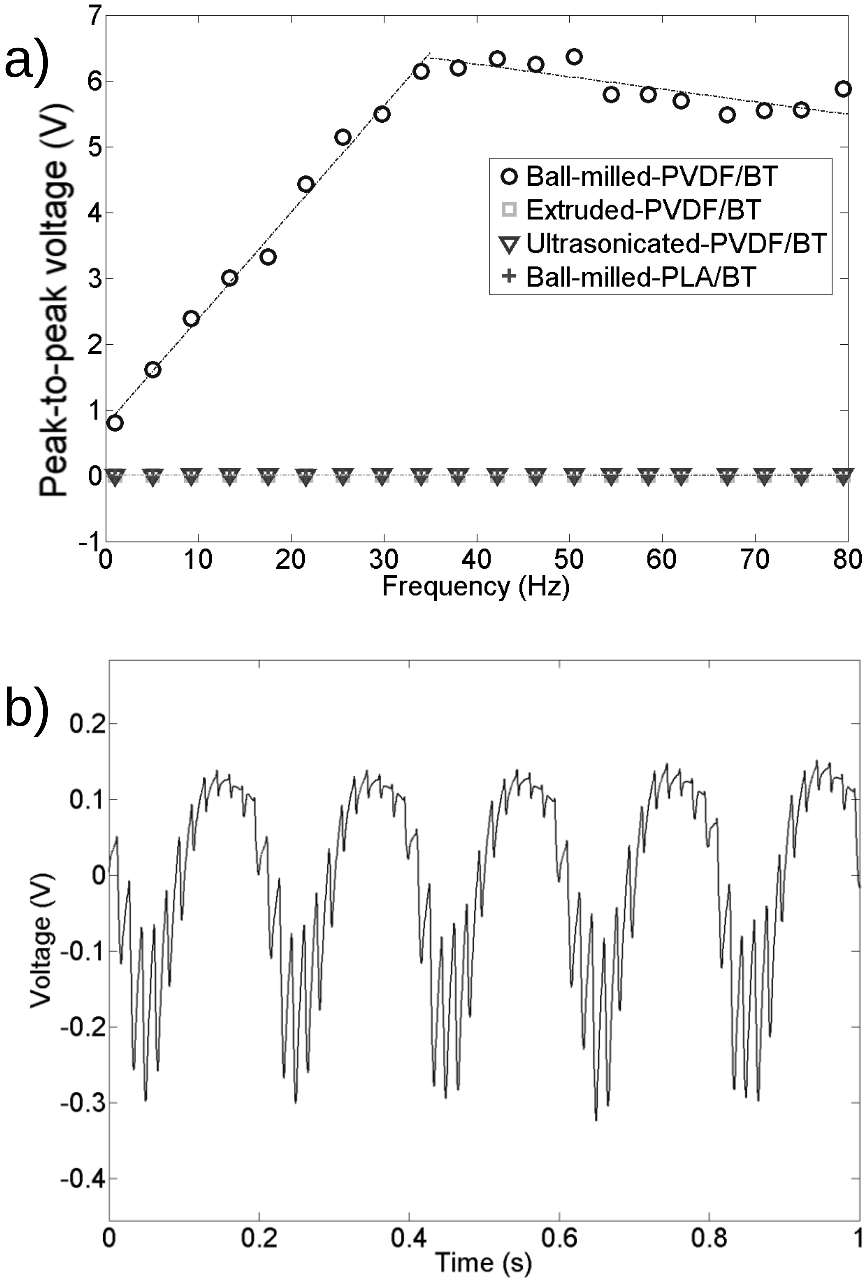

Figure 4.12: Peak-to-peak voltage output as a function of frequency for the three nanocomposite sensors with 10 wt.% BaTiO3 NPs (BT) prepared by: ball-milling, extrusion and sonication and the PLA sensor (applied sinusoidal displacement from 0 to 50 µm). (b) Representative signal of sensor fabricated from the ball-milled nanocomposite with 10 wt.% BaTiO$_3$ nanoparticles at 5 Hz (filtered signal: Butterworth filter, band pass 1-10 Hz)

For the multi-frequency piezoelectric tests, the DMA was used in tension mode with a displacement amplitude of 50 µm (selected from the results of the quasi static tests). Tests were conducted on the films sensors (three samples for each processing technique with 10 wt.% filler loading) with average dimensions 6 × 20 × 0.1 mm. Rectangular electrodes (10 × 5 mm) were silver painted on each side of the sensors (see schematic Figure S4.12a). The scans were carried out from 1 to 80 Hz in 20 steps. Piezoelectric charges obtained from the sensors were converted into voltages using a charge amplifier (MEAS specialties) and acquired with a data acquisition system: NI-9239, attached to a USB carrier NI-9162 (National Instruments) and recorded using a LabVIEW interface. Figure 4.12a shows that the maximum voltage output was obtained with sensors fabricated from the ball-milled nanocomposites whereas films fabricated from the other two methods failed to give outputs distinguishable from the electrical noise. The response of the sensor, although linear with respect to the force, shows a gradual increase until a frequency of 35 Hz and then stabilizes around ~6 V as the force reaches a plateau. This mismatch in the early region of the voltage versus stress curve can be attributed to the internal dipole alignment in the sensors owing to the repeated stretching during the test.[70, 71] Additionally, to study whether the exhibited piezoelectricity was due to the PVDF or the NPs, nanocomposites were prepared by ball-milling 10 wt.% of NPs in polylactide (PLA) and dicholoromethane (solvent for PLA). The fabrication process was similar to that used for the ball-milled PVDF nanocomposites. There was no voltage output in case of the PLA based nanocomposites; instigating the fact that the given process works because of the improved β-phase in PVDF and to attain the piezoelectric properties from the NPs, poling treatment would be a necessity.

A representative low frequency (for easier representation) voltage versus time output of the ball-milled sensors at 5 Hz is shown in Figure 4.12b. The curve resembles closely to the sinusoidal input of the DMA at 5 Hz.

4.8 Additional information on piezoelectric coefficient calculations

The d_{31} coefficients were calculated using the IEEE standard on piezoelectricity [72] from the curves in Figure 4.5. The simplified version of the constitutive equations in terms of d_{31} for in plane stretching, can be written as[176]:

$$V = \frac{Q}{C} = \frac{T_1 d_{31} t}{\varepsilon_r} \tag{4.1}$$

where V is the potential difference at the output, T_1 is the applied stress in 1-direction, t is the thickness of the film and ε_r the dielectric constant of the film at the given frequency. Here, 3 is the thickness direction of the film (charge collection/ voltage measurement direction) and 1 is the direction of application of force.

4.9 Scanning electron microscopy

SEM images of the cross-sections of the films fabricated from the nanocomposite prepared by the three mixing methods are shown in Figure 4.13. Micro-pores can be observed in the films of the ball-milled nanocomposite while the pores in case of the other two kinds of nanocomposites are very small as compared to those in ball-milling.

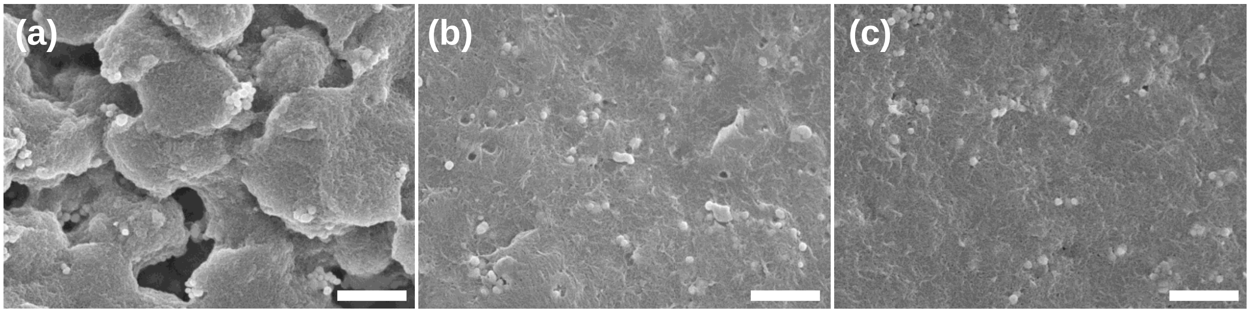

Figure 4.13: SEM images of fractured cross-sections of the films fabricated from the 0.2 g mL-1 nanocomposites (10 wt.% of $BaTiO_3$) in the solution prepared by (a) ball-milling; (b) extrusion and (c) sonication (scale bar = 1 µm)

4.10 X-ray diffractometry

Figure 4.14 shows the diffractogram patterns of films printed from the nanocomposites prepared by ball-mill mixing of 5, 10 and 15 wt.% $BaTiO_3$ NPs with PVDF. Again, 10 wt.% $BaTiO_3$ nanocomposites crystallized completely in β-phase whereas the other two concentrations possessed peaks of α and γ-phases close to 18.7 and 40°, respectively. The decrease in piezoelectric properties further in case of 15 wt.% filler addition can also be a result of decrease in β-phase as well as the overall crystallinity of the nanocomposite at higher particle loadings.[63, 73, 74] The degree of this decrease is again dependant on the particle shape and size, which is beyond the scope of this study.

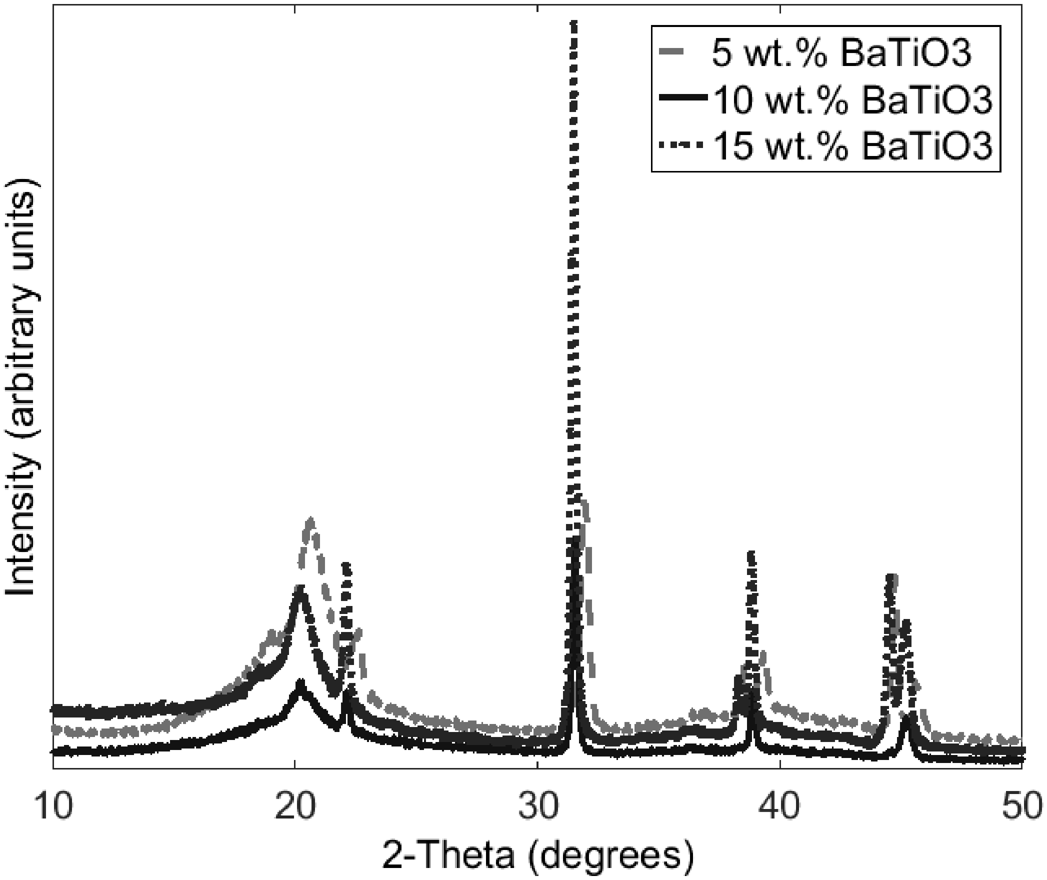

Figure 4.14: X-ray diffractogram of nanocomposite films prepared by ball-mill mixing with 5, 10 and 15 wt.% BaTiO3 nanoparticles in PVDF

4.11 Fourier Transform Infrared spectroscopy (FTIR)

The amount of β-phase amongst α and β-phases of PVDF is calculated with the help of Beer-Lambert law, which relates the absorption to the concentration of the species. The modified Beer-Lambert law for obtaining the fraction of β-phase is given by the equation below [75].

Fraction of β-phase,

$$F_\beta = \frac{A_\beta}{1.26A_\alpha + A_\beta} \tag{4.2}$$

where, A_{α} and A_{β} are the absorptions fractions of α and β-phases at 763 cm^{-1} and 840 cm^{-1}, respectively, and 1.26 is the ratio of absorption coefficients 7.7×10^4 and 6.1×10^4 cm^2mol^{-1} of β and α-phases, respectively.

4.12 Ferroelectric characterization of PVDF nanocomposites

Sensors for the impedance tests were separately fabricated by silver painting a circular area (diameter = 7 mm) on both sides of the nanocomposite films. Impedance tests to determine the dielectric constant and capacitance were performed using an impedance analyser (Agilent 4294A Precision) in the frequency range of 40 Hz to 1 kHz. The impedance values obtained from the tests were used to calculate the capacitance, C and the dielectric constant, ε_r, of the nanocomposites using the following formulae:[76]

$$C = -\frac{1}{\omega}\left[\frac{Z_I}{Z_I^2+Z_R^2}\right], \tag{4.3}$$

where Z_R and Z_I are real and imaginary parts of the impedance (Ω) and ω is frequency (rad s^{-1}).

The dielectric constant ε_r was evaluated from the definition of capacitance:

$$C = \varepsilon_0 \varepsilon_r \frac{A}{d}, \tag{4.4}$$

where ε_0 is the relative permittivity of free space (8.854×10^{-12} F m^{-1}), A is the area (m^2), and d (m) is the thickness of the sensor.

Table 4.1 and 4.2 show the variation of capacitance and dielectric constant values, respectively, for the nanocomposites prepared by three different approaches with the nanoparticle content at 45 Hz. Each value is an average of three samples. Ferroelectric properties decreased for both the extrusion and ball-mill mixed nanocomposites after 10 wt.% particle addition. However, the ferroelectric properties continued to increase for the sonicated nanocomposite sensors. Ball-milled nanocomposites exhibited highest ferroelectric properties.

Table 4-1: Variation of capacitance (pF) with nanoparticle loading in PVDF prepared by ball-milling, extrusion and sonication approaches at 45 Hz

Sensor type	$BaTiO_3$ content (wt.%)			
	0	5	10	15
PVDF	24			
Ball-milled		401	68	53
Extruded		379	77	140
Ultrasonicated		344	27	329

Table 4-2: Variation of dielectric constant with nanoparticle loading in PVDF prepared by ball-milling, extrusion and sonication approaches at 45 Hz

Sensor type	$BaTiO_3$ content (wt.%)			
	0	5	10	15
PVDF	9			
Ball-milled		171	210	76
Extruded		20	11	10
Ultrasonicated		16	36	88

4.13 Process viscosity characterization of PVDF nanocomposites prepared by ball-milling

To calculate the apparent viscosity of the solutions, shear stress τ_w was calculated from the applied pressures (neglecting the capillary flow effects as L/D > 50 [38]) with the formula [33],

$$\tau_w = \Delta P . \frac{D}{4L} \tag{4.5}$$

where, ΔP is the difference between the applied pressure and atmospheric pressure.

The Newtonian shear rate is then given by

$$\gamma'_{Newt} = \frac{4Q}{\pi(\frac{D}{2})^3} \tag{4.6}$$

where, Q is the volumetric flow rate. To obtain the actual shear rate at the point of extrusion, we use Rabinowitch-Mooney correction parameter n defined by,

$$n = \frac{d \log(\tau_w)}{d \log(\gamma'_{Newt})} \tag{4.7}$$

which is obtained from the slope of the log-log plot of shear stress versus Newtonian shear rate. Then the shear rate is calculated by,

$$\gamma' = \gamma'_{Newt} \frac{3n+1}{4n} \tag{4.8}$$

Finally, the apparent viscosity η_{app} is calculated as,

$$\eta_{app} = \frac{\tau_w}{\gamma'} \tag{4.9}$$

4.14 3D sensor testing

The 3D contact sensor was compared with a film sensor with the same electroded surface area as that of the cylindrical sensor. The test consisted of gently touching each sensor 3 times. The output voltages are presented in Figure 4.15. Where the film sensor generated a maximum voltage output of around -0.7 volts on touching (0.64 V on releasing), the 3D sensor produced up to 7.4 V (-1.7 V on releasing).

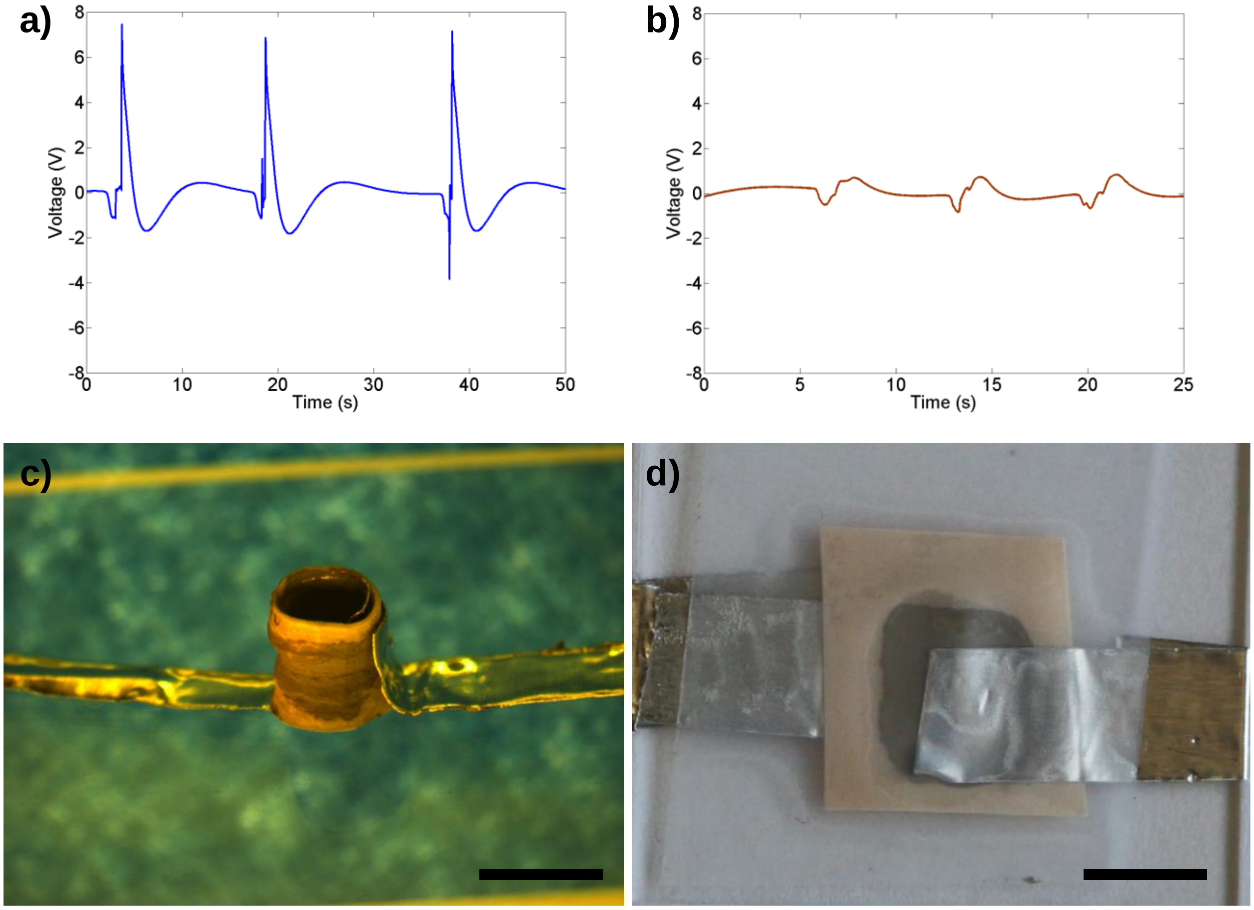

Figure 4.15: Sensor output voltages upon 3 consecutive taps: (a) 3D sensor; (b) film sensor. Pictures of the sensors (c) 3D sensor (scale bar = 3 mm) and (d) film sensor (scale bar = 5 mm)

The following schematic (Figure 4.16) explains the working of the cylindrical sensor. As the cylindrical sensor is touched with a finger, the compression of the sensor creates a potential difference (depicted by the voltage peak in the positive direction). When the current starts flowing across the circuit the voltage decreases as seen by the decaying signal.[21, 77] Once the finger is removed, the stress acting on the sensor is released causing the electron flow in the opposite direction. This is seen as the negative part of the signal. Due to the non-uniformity in the touch and release forces, the signal is asymmetric, similar to that found in the literature.[21, 22, 78] The frequency is the same as that of the touching. The voltage output generated by the sensor is a consequence of a combination of various piezoelectric modes as opposed to just the single mode in the case of film or fiber-based sensors.

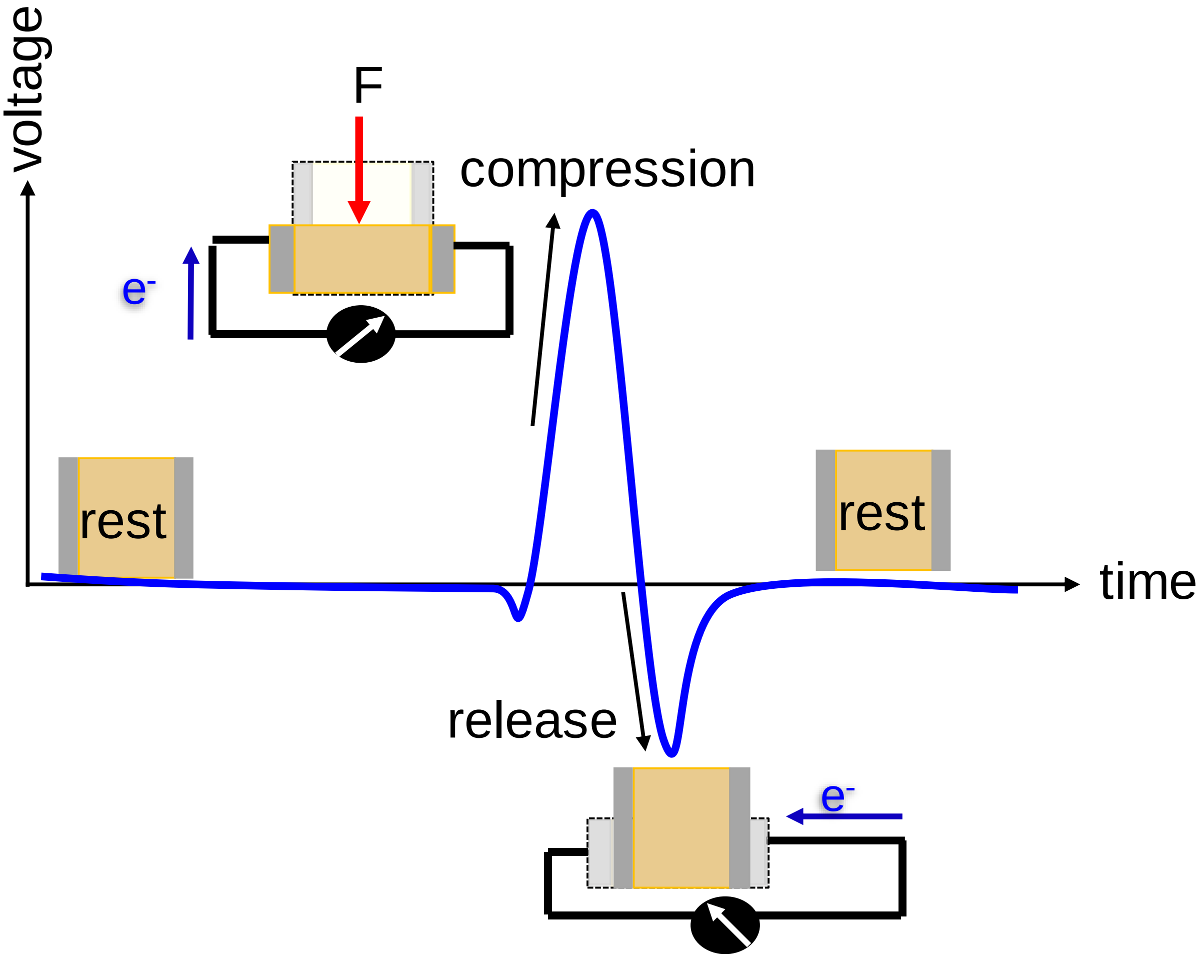

Figure 4.16: Schematic explaining the working of the sensor

References:

[1] C. T. Pan, Y. M. Hwang, L. Lin, and Y. C. Chen, *Design and Fabrication of Self-Powered Micro-Harvesters: Rotating and Vibrated Micro-Power Systems*: Wiley, 2014.

[2] J. B. Lando, H. G. Olf, and A. Peterlin, "Nuclear magnetic resonance and x-ray determination of the structure of poly(vinylidene fluoride)," *Journal of Polymer Science Part A-1: Polymer Chemistry,* vol. 4, pp. 941-951, 1966.

[3] K. Seok Ju, P. Youn Jung, J. Sung, P. S. Jo, P. Cheolmin, K. J. Kim, *et al.*, "Spin cast ferroelectric beta poly(vinylidene fluoride) thin films via rapid thermal annealing," *Applied Physics Letters,* vol. 92, pp. 012921-012921-3, 2008.

[4] P. Sajkiewicz, A. Wasiak, and Z. Gocłowski, "Phase transitions during stretching of poly(vinylidene fluoride)," *European Polymer Journal,* vol. 35, pp. 423-429, 3// 1999.

[5] V. Sencadas, R. Gregorio, and S. Lanceros-Méndez, "α to β Phase Transformation and Microestructural Changes of PVDF Films Induced by Uniaxial Stretch," *Journal of Macromolecular Science, Part B: Physics,* vol. 48, pp. 514-525, 2009/05/21 2009.

[6] Y. Y. Zhang, S. L. Jiang, Y. Yu, G. Xiong, Q. F. Zhang, and G. Z. Guang, "Phase transformation mechanisms and piezoelectric properties of poly(vinylidene fluoride)/montmorillonite composite," *Journal of Applied Polymer Science,* vol. 123, pp. 2595-2600, 2012.

[7] G. Neumann, E. Bihler, G. Eberle, and W. Eisenmenger, "Polarization distribution in PVDF obtained by poling under constant current condition," in *Electrical Insulation and Dielectric Phenomena, 1990. Annual Report., Conference on*, 1990, pp. 96-101.

[8] "Poling and characterization of piezoelectric polymer fibers for use in textile sensors," *Sensors and Actuators A: Physical,* vol. 201, pp. 477–486, 2013.

[9] S. Bodkhe, P. S. M. Rajesh, S. Kamle, and V. Verma, "Beta-phase enhancement in polyvinylidene fluoride through filler addition: comparing cellulose with carbon nanotubes and clay," *Journal of Polymer Research,* vol. 21, pp. 1-11, 2014/04/16 2014.

[10] P. S. M. Rajesh, S. Bodkhe, S. Kamle, and V. Verma, "Enhancing beta-phase in PVDF through physicochemical modification of cellulose," *Electronic Materials Letters,* vol. 10, pp. 315-319, 2014/01/01 2014.

[11] W. Huang, K. Edenzon, L. Fernandez, S. Razmpour, J. Woodburn, and P. Cebe, "Nanocomposites of poly(vinylidene fluoride) with multiwalled carbon nanotubes," *Journal of Applied Polymer Science,* vol. 115, pp. 3238-3248, 2010.

[12] Z. H. Liu, C. T. Pan, L. W. Lin, and H. W. Lai, "Piezoelectric properties of PVDF/MWCNT nanofiber using near-field electrospinning," *Sensors and Actuators A: Physical,* vol. 193, pp. 13-24, 4/15/ 2013.

[13] D. R. Dillon, K. K. Tenneti, C. Y. Li, F. K. Ko, I. Sics, and B. S. Hsiao, "On the structure and morphology of polyvinylidene fluoride–nanoclay nanocomposites," *Polymer,* vol. 47, pp. 1678-1688, 2/22/ 2006.

[14] J. S. Andrew and D. R. Clarke, "Enhanced Ferroelectric Phase Content of Polyvinylidene Difluoride Fibers with the Addition of Magnetic Nanoparticles," *Langmuir,* vol. 24, pp. 8435-8438, 2008/08/01 2008.

[15] X. Jing, X. Shen, H. Song, and F. Song, "Magnetic and dielectric properties of barium ferrite fibers/poly(vinylidene fluoride) composite films," *Journal of Polymer Research,* vol. 18, pp. 2017-2021, 2011/11/01 2011.

[16] X. Ni, F. Wang, A. Lin, Q. Xu, Z. Yang, and Y. Qin, "Flexible Nanogenerator Based on Single BaTiO3 Nanowire," *Science of Advanced Materials,* vol. 5, pp. 1781-1787, // 2013.

[17] M. Yuan, L. Cheng, Q. Xu, W. Wu, S. Bai, L. Gu, *et al.*, "Biocompatible Nanogenerators through High Piezoelectric Coefficient 0.5Ba(Zr0.2Ti0.8)O3-0.5(Ba0.7Ca0.3)TiO3 Nanowires for In-Vivo Applications," *Advanced Materials,* vol. 26, pp. 7432-7437, 2014.

[18] T. G. Mofokeng, "Preparation and properties of PVDF based BaTiO3 containing nanocomposites," MASTER OF SCIENCE (M.Sc.), Department of Chemistry, University of Free State (Qwaqwa Campus), 2014.

[19] H.-J. Ye, W.-Z. Shao, and L. Zhen, "Tetradecylphosphonic acid modified BaTiO3 nanoparticles and its nanocomposite," *Colloids and Surfaces A: Physicochemical and Engineering Aspects,* vol. 427, pp. 19-25, 6/20/ 2013.

[20] X. Luo, L. Chen, X. Chen, and Q. Huang, "Preparation and Electromechanical Properties of PVDF Matrix Piezoelectric Composites Containing Highly Oriented BaTiO3 Whiskers," *J. Mater. Sci. Technol.,* vol. 20, pp. 441-444 2004-07-28 2004.

[21] Y. Zhao, Q. Liao, G. Zhang, Z. Zhang, Q. Liang, X. Liao, *et al.*, "High output piezoelectric nanocomposite generators composed of oriented BaTiO3 NPs@PVDF," *Nano Energy,* vol. 11, pp. 719-727, 1// 2015.

[22] J. Nunes-Pereira, V. Sencadas, V. Correia, V. F. Cardoso, W. Han, J. G. Rocha, *et al.*, "Energy harvesting performance of BaTiO3/poly(vinylidene fluoride–trifluoroethylene) spin coated nanocomposites," *Composites Part B: Engineering,* vol. 72, pp. 130-136, 4// 2015.

[23] U. Valiyaneerilakkal and S. Varghese, "Poly (vinylidene fluoride-trifluoroethylene)/barium titanate nanocomposite for ferroelectric nonvolatile memory devices," *AIP Advances,* vol. 3, p. 042131, 2013.

[24] M. Rajib, M. Arif Ishtiaque Shuvo, H. Karim, D. Delfin, S. Afrin, and Y. Lin, "Temperature influence on dielectric energy storage of nanocomposites," *Ceramics International,* vol. 41, pp. 1807-1813, 1// 2015.

[25] L. Zhang, D. Xiao, and J. Ma, "Dielectric Properties of PVDF/Ag/BaTiO3 Composites," *Ferroelectrics,* vol. 455, pp. 77-82, 2013/01/01 2013.

[26] D.-H. Lee, J.-H. Lee, D.-W. Kim, B.-K. Kim, and H.-J. Je, "Enhanced dielectric constant of polymer-matrix composites using nano-BaTiO3 agglomerates," *Journal of the Ceramic Society of Japan,* vol. 118, pp. 62-65, 2010.

[27] F. Yiin-Kuen, H. Hsi-Chun, W. Bo-Sheng, and L. Shan-Chien, "All-fiber transparent piezoelectric harvester with a cooperatively enhanced structure," *Nanotechnology,* vol. 27, p. 435403, 2016.

[28] C. Lee and J. A. Tarbutton, "Electric Poling-assisted Additive Manufacturing Process for Lead-free Piezoelectric Device Fabrication," *Procedia Manufacturing,* vol. 1, pp. 320-326, 2015/01/01 2015.

[29] K. Kim, W. Zhu, X. Qu, C. Aaronson, W. R. McCall, S. Chen, *et al.*, "3D Optical Printing of Piezoelectric Nanoparticle–Polymer Composite Materials," *ACS Nano,* vol. 8, pp. 9799-9806, 2014/10/28 2014.

[30] G. Luo, K. S. Teh, Y. Liu, X. Zang, Z. Wen, and L. Lin, "Direct-Write, Self-Aligned Electrospinning on Paper for Controllable Fabrication of Three-Dimensional Structures," *ACS Applied Materials & Interfaces,* vol. 7, pp. 27765-27770, 2015/12/23 2015.

[31] J. Pu, X. Yan, Y. Jiang, C. Chang, and L. Lin, "Piezoelectric actuation of direct-write electrospun fibers," *Sensors and Actuators A: Physical,* vol. 164, pp. 131-136, 11// 2010.

[32] S. Z. Guo, F. Gosselin, N. Guerin, A. M. Lanouette, M. C. Heuzey, and D. Therriault, "Solvent-cast three-dimensional printing of multifunctional microsystems," *Small,* vol. 9, pp. 4118-22, Dec 20 2013.

[33] S.-Z. Guo, M.-C. Heuzey, and D. Therriault, "Properties of Polylactide Inks for Solvent-Cast Printing of Three-Dimensional Freeform Microstructures," *Langmuir,* vol. 30, pp. 1142-1150, 2014/02/04 2014.

[34] A. Aesar, "A13547 N,N-Dimethylformamide, 99%," A. A. (R), Ed., ed, 2017.

[35] M. Benz, W. B. Euler, and O. J. Gregory, "The Role of Solution Phase Water on the Deposition of Thin Films of Poly(vinylidene fluoride)," *Macromolecules,* vol. 35, pp. 2682-2688, 2002/03/01 2002.

[36] *Poly(vinylidene fluoride)*.

[37] M. D. John, "Elements of Rheology," in *Polymer Processing Instabilities,* ed: CRC Press, 2004, pp. 13-42.

[38] J. Bruneaux, D. Therriault, and M.-C. Heuzey, "Micro-extrusion of organic inks for direct-write assembly," *Journal of Micromechanics and Microengineering,* vol. 18, p. 11, 7 October 2008 2008.

[39] G. A. Kontos, A. L. Soulintzis, P. K. Karahaliou, G. C. Psarras, S. N. Georga, C. A. Krontiras*, et al.*, "Electrical relaxation dynamics in TiO2 – polymer matrix composites," *Express polymer letters,* vol. 1, pp. 781-789, 2007.

[40] M. Roy, J. K. Nelson, R. K. MacCrone, L. S. Schadler, C. W. Reed, and R. Keefe, "Polymer nanocomposite dielectrics-the role of the interface," *IEEE Transactions on Dielectrics and Electrical Insulation,* vol. 12, pp. 629-643, 2005.

[41] C. Zhang, Q. Chi, J. Dong, Y. Cui, X. Wang, L. Liu*, et al.*, "Enhanced dielectric properties of poly(vinylidene fluoride) composites filled with nano iron oxide-deposited barium titanate hybrid particles," *Scientific Reports,* vol. 6, p. 33508, 09/16/online 2016.

[42] S. Bodkhe, F. P. Gosselin, and D. Therriault, "Three-dimensional printing of polyvinylidene fluoride nanocomposites," in *20th International Conference on Composite Materials*, Copenhagen, Denmark, 2015, p. 9.

[43] P. Martins, A. C. Lopes, and S. Lanceros-Mendez, "Electroactive phases of poly(vinylidene fluoride): Determination, processing and applications," *Progress in Polymer Science*, vol. 39, pp. 683–706, 2014.

[44] S. Huang, W. A. Yee, W. C. Tjiu, Y. Liu, M. Kotaki, Y. C. F. Boey, *et al.*, "Electrospinning of Polyvinylidene Difluoride with Carbon Nanotubes: Synergistic Effects of Extensional Force and Interfacial Interaction on Crystalline Structures," *Langmuir*, vol. 24, pp. 13621-13626, 2008/12/02 2008.

[45] S. Yu, W. Zheng, W. Yu, Y. Zhang, Q. Jiang, and Z. Zhao, "Formation Mechanism of β-Phase in PVDF/CNT Composite Prepared by the Sonication Method," *Macromolecules*, vol. 42, pp. 8870-8874, 2009/11/24 2009.

[46] D. Shah, P. Maiti, E. Gunn, D. F. Schmidt, D. D. Jiang, C. A. Batt, *et al.*, "Dramatic Enhancements in Toughness of Polyvinylidene Fluoride Nanocomposites via Nanoclay-Directed Crystal Structure and Morphology," *Advanced Materials*, vol. 16, pp. 1173-1177, 2004.

[47] P. Dineva, D. Gross, R. Müller, and T. Rangelov, "Piezoelectric Materials," in *Dynamic Fracture of Piezoelectric Materials: Solution of Time-Harmonic Problems via BIEM*, ed Cham: Springer International Publishing, 2014, pp. 7-32.

[48] Y. Niu, K. Yu, Y. Bai, and H. Wang, "Enhanced dielectric performance of BaTiO3/PVDF composites prepared by modified process for energy storage applications," *IEEE Transactions on Ultrasonics, Ferroelectrics, and Frequency Control*, vol. 62, pp. 108-115, 2015.

[49] S. Nayak, B. Sahoo, T. K. Chaki, and D. Khastgir, "Facile preparation of uniform barium titanate (BaTiO3) multipods with high permittivity: impedance and temperature dependent dielectric behavior," *RSC Advances*, vol. 4, pp. 1212-1224, 2014.

[50] Y. Yamashita, M. Tada, M. Kakihana, M. Osada, and K. Yoshida, "Synthesis of RuO2-loaded BaTinO2n + 1 (n = 1, 2 and 5) using a polymerizable complex method and its photocatalytic activity for the decomposition of water," *Journal of Materials Chemistry*, vol. 12, pp. 1782-1786, 2002.

[51] V. K. Thakur, J. Yan, M.-F. Lin, C. Zhi, D. Golberg, Y. Bando, *et al.*, "Novel polymer nanocomposites from bioinspired green aqueous functionalization of BNNTs," *Polymer Chemistry*, vol. 3, pp. 962-969, 2012.

[52] M. S. Gaur, P. Singh, A. Ali, and R. Singh, "Thermally stimulated discharge current (TSDC) characteristics in β-phase PVDF–BaTiO3 nanocomposites," *Journal of Thermal Analysis and Calorimetry,* vol. 117, pp. 1407-1417, 2014/09/01 2014.

[53] K. P. Pramoda, A. Mohamed, I. Yee Phang, and T. Liu, "Crystal transformation and thermomechanical properties of poly(vinylidene fluoride)/clay nanocomposites," *Polymer International,* vol. 54, pp. 226-232, 2005.

[54] M.-F. Lin and P. S. Lee, "Formation of PVDF-g-HEMA/BaTiO3 nanocomposites via in situ nanoparticle synthesis for high performance capacitor applications," *Journal of Materials Chemistry A,* vol. 1, pp. 14455-14459, 2013.

[55] F. A. Sánchez, M. Redondo, and J. González-Benito, "Influence of BaTiO3 submicrometric particles on the structure, morphology, and crystallization behavior of poly(vinylidene fluoride)," *Journal of Applied Polymer Science,* vol. 132, pp. 41497(1-10), 2015.

[56] D. Fu and M. Itoh, *Role of Ca off-Centering in Tuning Ferroelectric Phase Transitions in Ba(Zr,Ti)O3System*, 2015.

[57] S. P. Division, "Piezo Film Sensors Technical Manual," Measurement Specialties, Inc, Norristown, PA 1999.

[58] W. C. Gan and W. H. A. Majid, "Effect of TiO 2 on enhanced pyroelectric activity of PVDF composite," *Smart Materials and Structures,* vol. 23, p. 045026, 2014.

[59] B. Ploss, W.-Y. Ng, H. L.-W. Chan, B. Ploss, and C.-L. Choy, "Poling study of PZT/P(VDF–TrFE) composites," *Composites Science and Technology,* vol. 61, pp. 957-962, 5// 2001.

[60] J. Sirohi and I. Chopra, "Fundamental understanding of piezoelectric strain sensors," 1999, pp. 528-542.

[61] V. P. Pavlović, V. B. Pavlović, B. Vlahović, D. K. Božanić, J. D. Pajović, R. Dojčilović, *et al.*, "Structural properties of composites of polyvinylidene fluoride and mechanically activated BaTiO 3 particles," *Physica Scripta,* vol. 2013, p. 014006, 2013.

[62] V. P. Pavlović, D. Popović, J. Krstić, J. Dojčilović, B. Babić, and V. B. Pavlović, "Influence of mechanical activation on the structure of ultrafine BaTiO3 powders," *Journal of Alloys and Compounds,* vol. 486, pp. 633-639, 11/3/ 2009.

[63] S. F. Mendes, C. M. Costa, C. Caparros, V. Sencadas, and S. Lanceros-Méndez, "Effect of filler size and concentration on the structure and properties of poly(vinylidene fluoride)/BaTiO3 nanocomposites," *Journal of Materials Science,* vol. 47, pp. 1378-1388, 2012.

[64] J. Nunes-Pereira, V. Sencadas, V. Correia, J. G. Rocha, and S. Lanceros-Méndez, "Energy harvesting performance of piezoelectric electrospun polymer fibers and polymer/ceramic composites," *Sensors and Actuators A: Physical,* vol. 196, pp. 55-62, 7/1/ 2013.

[65] D. A. Kraft. (13 January 2017). *Polymer Orientation*. Available: http://www.che.hw.ac.uk/teaching/B11MS1/Material/Processing/Orient.htm

[66] J. Yao, C. Bastiaansen, and T. Peijs, "High Strength and High Modulus Electrospun Nanofibers," *Fibers,* vol. 2, p. 158, 2014.

[67] P. J. Carreau, D. De Kee, and R. P. Chhabra, *Rheology of Polymeric Systems: Principles and Applications*: Hanser Publishers, 1997.

[68] B. G. Compton and J. A. Lewis, "3D-Printing of Lightweight Cellular Composites," *Advanced Materials,* vol. 26, pp. 5930-5935, 2014.

[69] D. M. Correia, C. Ribeiro, V. Sencadas, L. Vikingsson, M. Oliver Gasch, J. L. Gómez Ribelles, *et al.*, "Strategies for the development of three dimensional scaffolds from piezoelectric poly(vinylidene fluoride)," *Materials & Design,* vol. 92, pp. 674-681, 2/15/ 2016.

[70] Y. Xu, *Ferroelectric materials and their applications*: Elsevier, 2013.

[71] A. C. Wirtz, C. Hofmann, and E. J. J. Groenen, "Stretched Polyethylene Films Probed by Single Molecules," *ChemPhysChem,* vol. 12, pp. 1519-1528, 2011.

[72] "IEEE Standard on Piezoelectricity," *ANSI/IEEE Std 176-1987,* p. 0_1, 1988.

[73] Alamusi, J. Xue, L. Wu, N. Hu, J. Qiu, C. Chang, *et al.*, "Evaluation of piezoelectric property of reduced graphene oxide (rGO)-poly(vinylidene fluoride) nanocomposites," *Nanoscale,* vol. 4, pp. 7250-7255, 2012.

[74] L. Lee, S.-J. Park, and S. Kim, "Effect of nano-sized barium titanate addition on PEO/PVDF blend-based composite polymer electrolytes," *Solid State Ionics,* vol. 234, pp. 19-24, 3/7/ 2013.

[75] J. R. Gregorio and M. Cestari, "Effect of crystallization temperature on the crystalline phase content and morphology of poly(vinylidene fluoride)," *Journal of Polymer Science Part B: Polymer Physics,* vol. 32, pp. 859-870, 1994.

[76] V. V. Brus, "On impedance spectroscopy analysis of nonideal heterojunctions," *Semiconductor Science and Technology,* vol. 27, p. 035024, 2012.

[77] J.-I. Park, G.-Y. Lee, J. Yang, C.-S. Kim, and S.-H. Ahn, "Flexible ceramic-elastomer composite piezoelectric energy harvester fabricated by additive manufacturing," *Journal of Composite Materials,* April 6, 2015 2015.

[78] D. Chen, T. Sharma, and J. X. J. Zhang, "Mesoporous surface control of PVDF thin films for enhanced piezoelectric energy generation," *Sensors and Actuators A: Physical,* vol. 216, pp. 196-201, 9/1/ 2014.

CHAPTER 5 ARTICLE 2: IN-SITU POLING-ASSISTED 3D PRINTING OF PIEZOELECTRIC PVDF NANOCOMPOSITE SENSORS FOR GAIT ANALYSIS

Sampada Bodkhe, P S M Rajesh, Frederick P. Gosselin, and Daniel Therriault*

Submitted to Journal of Materials Chemistry A, 8th Novembre 2017.

Abstract

Given the ever-increasing demand for customization and miniaturization, in-situ three-dimensional (3D) printing of piezoelectric polymers comes as an efficient means to cater to smart structures via multi-material printing. The processability of piezoelectric polymer polyvinylidene fluoride (PVDF) and the superior piezoelectric properties of barium titanate ($BaTiO_3$) make their nanocomposites an ideal recipe for printing customized active sensors. Combining the fabrication and high voltage poling steps shrinks the manufacturing time and increases the scope for on-demand application. To realize such an improvement, we investigate the 3D printing of PVDF and PVDF-$BaTiO_3$ nanocomposites by simultaneously applying an electric field to achieve in-situ poling. A remarkable 300% improvement in polarization was achieved, via 10 wt.% filler addition and applying an electric field of 1 MV m^{-1}, over printed unpoled neat PVDF. We also present studies on the role of nanoparticle addition, and applied electric field on the piezoelectric properties of PVDF. Ultimately, we demonstrate the application of the in-situ poling process in the form of sensors printed directly on a shoe insole for gait-analysis. The sensors fabricated in this work effectively distinguished between walking and stamping both as a portable in-shoe sensor as well as sensors attached to the ground.

5.1 Introduction

The most piezoelectric polymer polyvinylidene fluoride (PVDF), and its nanocomposites are being applied towards actuation, energy harvesting,[1] energy storage,[2] and sensing.[3] Traditionally, PVDF-based structures were fabricated in the form of fibers or films using extrusion,[4] melt spinning,[5] spin coating,[6] solution casting[7] and electrospinning.[8] Last few years have seen a strong impetus in creating three-dimensional (3D) structures with PVDF as it: (i) promotes flexibility in shape, (ii) boosts the piezoelectric coupling factor by increasing the extractable strain in the structure,[9] and (iii) aids in fabricating on-demand and customized structures.

3D printing of PVDF and its nanocomposites has been attempted by various techniques.[10-12] Of these near-field electrospinning (NFES)[10, 13] and solvent evaporation-assisted 3D printing (SEA-3DP)[11, 14] have been successful in creating multi-layered[10] self-supported[11], conformal,[14] and freestanding structures.[14] Another technique involves integrated 3D printing via fused deposition modelling and corona poling. The technique as compared to NFES and SEA-3DP is time consuming as it involves printing of a layer followed by poling of the entire layer in a point-by-point fashion following the print line.[15] Where NFES involves application of large electric fields during the deposition of PVDF-based solutions to attain the piezoelectric polarization, SEA-3DP relies on the interaction between barium titanate nanoparticles ($BaTiO_3$ NPs) and PVDF, and dipole alignment via high shear forces during high pressure extrusion. In SEA-3DP, a highly volatile solution of the piezoelectric nanocomposite (NC) is extruded and deposited with the help of a robotic deposition system to form the required shape. SEA-3DP has shown to result in piezoelectric properties (d_{31} = 18 pC N^{-1}) comparable to commercial (Measurement Specialties) poled PVDF films (d_{31} = 23 pC N^{-1}).[16] However, it is compelling to investigate the effect of simultaneous application of electric field during printing of PVDF and NC. Moreover, printing of piezoelectric PVDF has so far been shown only on flat surfaces.

Here, for the first time we show the 3D conformal printing of piezoelectric PVDF on a curved surface with in-situ poling for enhanced performance. We present a detailed investigation of the effect of NP addition and electric field on the β-phase and piezoelectric properties of PVDF. The content of β-phase is characterized via X-ray diffraction (XRD), and Fourier transform infrared spectroscopy (FTIR). We designed a drop-weight test to determine the piezoelectric properties of the films. Finally, we present the application in the form ready-to-use sensors on a shoe insole for gait analysis. The sensors printed on a shoe insole at fore and hind foot locations were tested to distinguish between walking and stamping, when the insole was worn in a shoe as well as when the insole was fixed to the ground.

5.2 Experimental

Materials

PVDF (M_w~534,000), dimethyl sulfoxide (DMSO), and silver conductive paste (micro-particles dispersed in α-terpineol) were purchased from Sigma Aldrich®. Solvents N, N-dimethyl formamide (DMF) and acetone were obtained from Alfa Aesar and BDH, respectively. Barium titanate NPs ($BaTiO_3$; 99.9% purity, mean diameter ~100 nm) were procured from Nanostructured & Amorphous materials Inc.

Ink Preparation

The solvent system consisted of a mixture of DMF and acetone.[17] Amongst the solvents used for PVDF, DMF is the least hazardous and possesses the lowest boiling point of ~153 °C,[18] while acetone is an anti-solvent with a low evaporation point (~56 °C). An optimized ratio of 40% DMF and 60% acetone in the solvent system was used.[19] A contribution of 65 g L^{-1} dimethyl sulfoxide (DMSO) aided in initiating β-phase.[20] The required mass of PVDF was sonicated in the solvent mixture for 20 min to obtain a clear PVDF solution. To form the nanocomposite, a process explained in the previous work [11] was used where 10 wt. % of $BaTiO_3$ NPs were incorporated into PVDF via ball-milling with the solvents for 20 min.

SEA-3D Printing

PVDF and its nanocomposite solutions (referred to as ‘inks’ hereafter) were poured into 3 mL syringe barrels. The syringe barrels were placed into a pneumatically operated dispensing system (HP-7X, EFD) to apply precise pressures for printing. The dispensing system was held by a robotic-arm (I&J2200-4, I&J Fisnar Inc.), controlled by a commercial software (JR Points for Dispensing, Janome Sewing Machine) that further enabled the deposition of the inks on a movable flat stage. The design to be printed was uploaded into the software in the form of a series of X, Y and Z coordinates.

The in-situ poling set-up (Figure 5.1) consisted of laboratory DC (direct current) power sources to apply the required electric field between a metallic printing nozzle and a metallic tape (aluminum or copper, 3M Canada) attached to the substrate. Single-sided aluminum tape was used to print freestanding films while sensors were printed on double-sided copper tape. Based on the electric field values, two DC power sources were employed: Gw Instek, GPS 3303 for electric fields up to 0.3 MV m^{-1} and the Fisher Scientific, FB 3000 for 1 MV m^{-1}. We fabricated a total of 8 types of films with 4 different poling voltages: 0, 0.1, 0.3 and 1 MV m^{-1}. The labelling of these films consists of the poling voltage in MV m^{-1} followed by letters: P for neat PVDF and NC for the nanocomposite. For example 0.3P stands for a PVDF film fabricated with 0.3 MV m^{-1} poling voltage. Films for XRD, FTIR spectroscopy, and piezoelectric tests were fabricated with 0.2 g mL^{-1} of PVDF and the NC solutions by keeping the printing parameters constant: nozzle diameter = 100 µm nozzle, extrusion pressure ~1 MPa, and stage velocity = 20 mm s^{-1}.

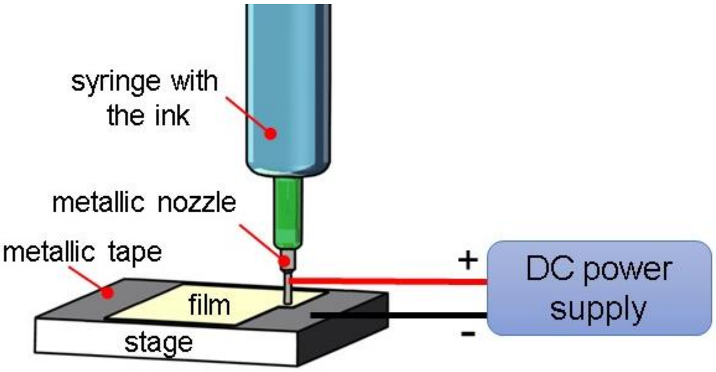

Figure 5.1: Schematic of in-situ poling set-up for SEA-3DP

We printed 3D structures using both PVDF and nanocomposite inks with a concentration of 0.25 g mL^{-1}. For conformal printing, copper (Cu) tape was stuck on a convex hemispherical surface as the bottom electrode and a NC filament was printed on the tape from the lower end of the hemisphere to its apex with an electric field of 0.3 MV m^{-1}.

Characterization

A Philips X'pert diffractometer was used to obtain the diffraction spectra between 16 to 28° at a rate of 0.4 °min^{-1} with a copper target (K_α radiation) at 50 kV and 40 mA. A FT–IR spectrometer (Perkin Elmer, Spectrum 65) was used to obtain the absorption spectra of PVDF and its nanocomposite films in the range of 500 – 4000 cm^{-1}. Each sample was scanned 32 times with a resolution of 4 cm^{-1}. Optical microscopy (BX-61 Olympus; Image-Pro plus V5 an image processing software from Media Cybernetics) was used to study the morphology of the 3D printed structures. Sensors were fabricated from the printed films by painting silver in a circular area (diameter ~7 mm) on both sides of the films. An LCR (inductance-capacitance-resistance) meter (Wavetek Metermen, LCR55) was used to measure the capacitance of the films.

Foot insole tests

Sensors (30 × 30 mm^2) were printed on a foot insole (Bayer Inc., Dr. Scholl's) at the metatarsal and heel region using the NC ink (Figure 5.7). The detailed step-by-step sensor fabrication is shown in Figure S5.1. A double-sided Cu tape placed on the insole formed the bottom electrode. The sensors were then printed (~1 MPa, 20 mm s^{-1} and 100 μm nozzle diameter) on the Cu tape with an electric field of 0.3 MV m^{-1}. After printing the sensors, silver was painted on the top layer of the sensor to form the second electrode. Leads were connected to both the bottom and the top electrodes using Cu tape. Tests were carried out by stamping the foot on the ground, and walking: with the insole worn in a shoe and insole placed directly on the ground. The subject weight was approximately 450 N (45 kg).

5.3 Results and Discussions

X-ray Diffraction

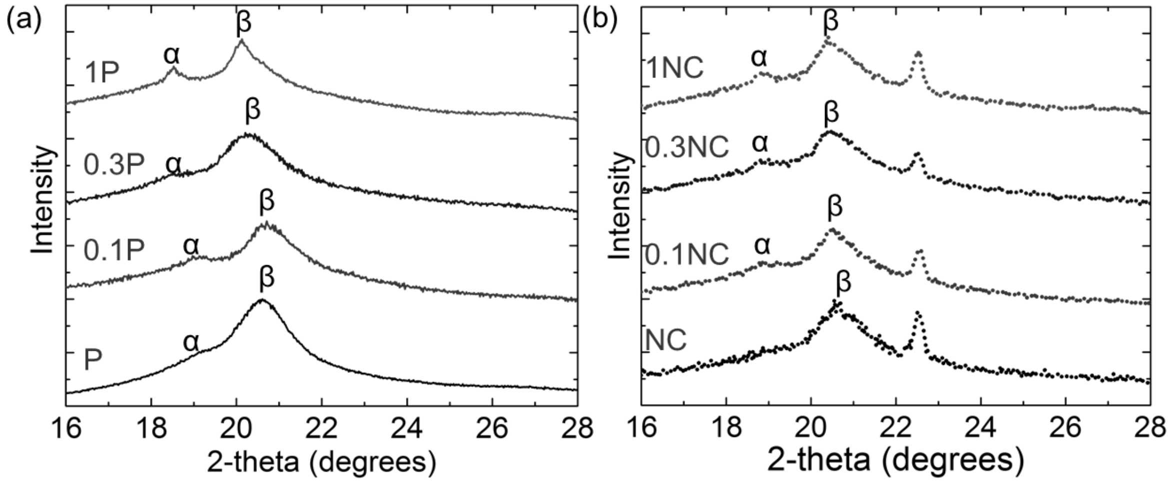

Figure 5.2: X-ray diffractograms of (a) P and (b) NC films fabricated with an electric field of 0, 0.1, 0.3 and 1 MV m^{-1}

Of all the polymorphs of PVDF, the α and δ polymorph possess a trans-gauche (TGTG') configuration, while the β and ϒ are found in all-trans (TTTT) planar zig-zag form.[21] Except the α-phase, in which PVDF commonly crystallizes upon solidification, all others are unstable in nature. The unstable all-trans β-phase is fundamental for pyro, piezo and ferroelectric properties in PVDF. XRD identifies various crystalline phases of PVDF. Peaks corresponding to α-phase are found at 2-theta values of 17.7, 18.4, 19.9 and 26.56° while that of γ-phase are at 20.04 and 26.8°.[22, 23] The β-phase is characterized by a well-defined peak at 20.26°,[22, 23] peak-broadening at 20.1° and diminishing of α-peaks at 18.4 and 26.7°.[24] Figure 5.2a shows the XRD patterns of the PVDF films fabricated with different electric fields used for poling. The β-peak at 20.1° has considerably broadened in case of the films prepared with the application of electric field. The α-peak at 18.4° is present in all the films, but is less pronounced in PVDF fabricated without any electric field. The same trend is observed for the NC films (Figure 5.2b); the film printed without any electric field features a broad β-peak whereas all other films possess an α-peak at 18.4°. The peak at 22.15° is the characteristic peak of $BaTiO_3$ NPs.[25] It should be noted that no peaks other than those corresponding to α and β-phases were observed in our work. The XRD results reveal that the addition of NPs to PVDF resulted in the disappearance of the α-phase. Moreover, surprisingly application of the electric field led to the formation of α-phase in all the films.

Fourier transform infrared spectroscopy - Photo acoustic spectroscopy (FTIR-PAS)

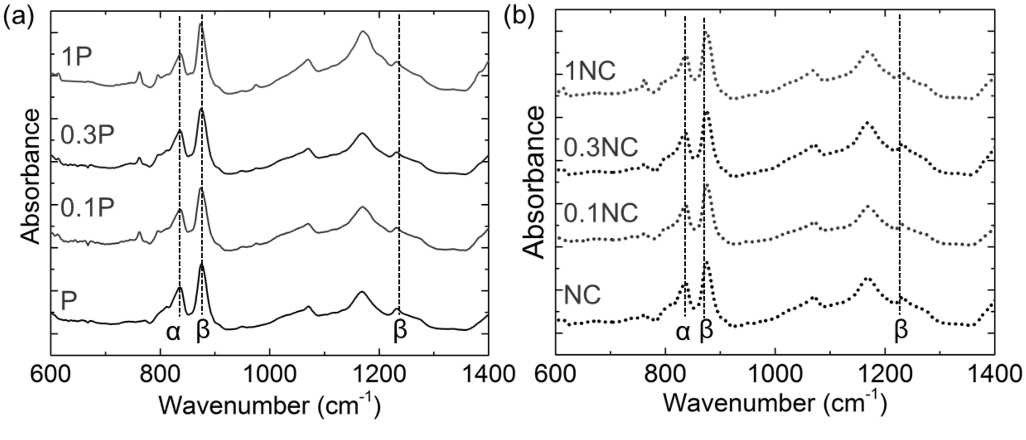

Figure 5.3: FTIR spectra of (a) P and (b) NC films fabricated with an electric field of 0, 0.1, 0.3 and 1 MV m^{-1}

To determine how the appearance of α-phase in the films fabricated via the application of electric field affected the overall β-phase content in PVDF we carried out FTIR analysis on the films. The characteristic absorption bands for α-phase are close to 490, 530, 615, 766, 855 and 974 cm^{-1}.[26] Though absorption bands at 510/512, 840/833 cm^{-1} for β and γ-phase, respectively, lie very close to each other, the band at 1279 cm^{-1} are only present in the case of β-phase.[23, 26] Figure 5.3 presents the FTIR spectra for all the films fabricated in this work. The peaks corresponding to the α-phase in PVDF seem to be present in all the films except those fabricated without the application of an external electric field. In addition, all the films possess the peak at 1279 cm^{-1} confirming the absence of any γ-phase. Hence, the FTIR analysis conforms the conclusions from the XRD that α-phase appears with the application of electric field.

Given that no third phase was present in the films, the relative amount of β-phase amongst α and β-phases of PVDF is calculated with the help of the Beer-Lambert law, which relates the absorption to the concentration of the species. The modified Beer-Lambert law for obtaining the fraction of β-phase (F_β) is given by the equation below:[27]

$$F_\beta = \frac{A_\beta}{1.26A_\alpha + A_\beta} \tag{5.1}$$

where, A_α and A_β are the absorption fractions of α and β-phases at 763 cm^{-1} and 840 cm^{-1}, respectively, and 1.26 is the ratio of absorption coefficients 7.7×10^4 and 6.1×10^4 $cm^2\,mol^{-1}$ of β and α-phases, respectively. The F_β calculated using Equation 5.1 for all the films is presented in Figure 5.4. The average values of the F_β in the films is found to be 71% ±5 %. Thus, poling voltages did not have any substantial influence on the overall β-phase fractions.[28] As there is no prominent difference between the content of β-phase, the piezoelectric properties in PVDF or

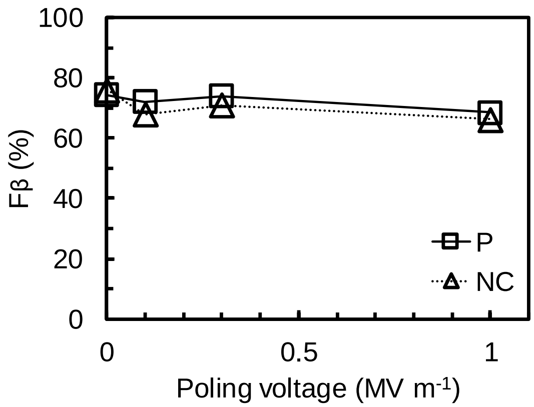

Figure 5.4: Fraction of β-phase in various films calculated using Beer-Lambert Law

NC would then be dominated by the amount of β-phase that is oriented, i.e., the net dipole moment in the material.[29-31]

Piezoelectric Characterization

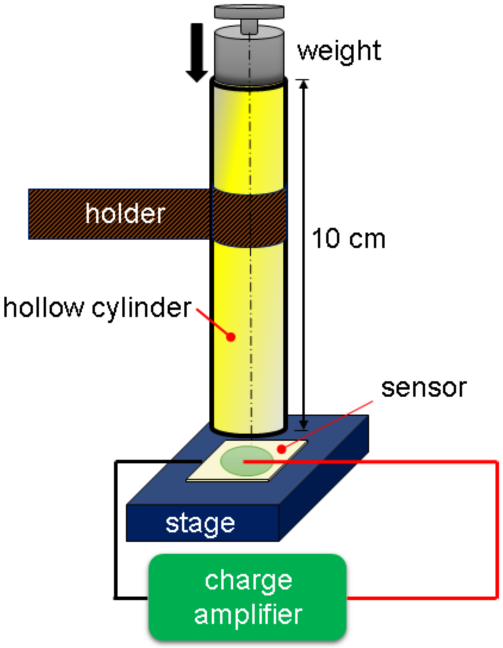

Figure 5.5: Schematic of drop-weight test setup for piezoelectric characterization of the sensors

To experimentally compare the extent of net dipole moment in the materials, we designed a piezoelectric drop-weight test. The test method consisted of impacting each sensor with a 10 g calibration weight from a height of 10 cm as shown in the schematic in Figure 5.5. The weight was dropped through a hollow cylinder so that the sensor was always impacted with the same force and energy. The inner diameter of the cylinder had a small tolerance with respect to the outer diameter of the weight to avoid any friction between the two surfaces during the fall. The piezoelectric charge output from the sensors upon the impact was converted into voltage through a charge amplifier (MEAS specialties) and was recorded using LabVIEW 2014.

The voltage, V (V) obtained from the sensors was converted in to charge, q (C) and then polarization, P (C m^{-2}) by using the following equations:

$$q = C\,V \tag{5.2}$$

$$P = q/A \tag{5.3}$$

where, *A* is the electrode area in m^2, and *C* is the capacitance (F) measured by the LCR meter.

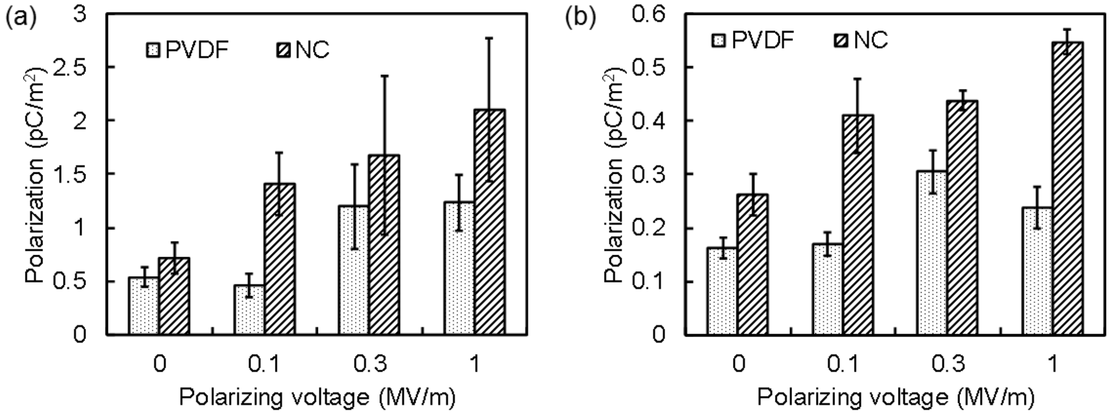

Figure 5.6: Piezoelectric outputs of P and NC sensors fabricated with electric fields 0, 0.1, 0.3 and 1 MV m^{-1}. (a) Average of 5 different samples, and (b) average of a single sample tested 5 times

Figure 5.6a presents the averaged piezoelectric outputs in terms of polarization for five different sensors for each type. It can be seen that addition of $BaTiO_3$ NPs led to increased polarization in the sensors. Polarization significantly increased with applied electric field. Filler addition and an electric field of 1 MV m^{-1} lead to an increase of ~300% over printed unpoled PVDF. High values of error are attributed to decrease in the properties of the films due to local heating at higher fields during the printing process. To ascertain the repeatability in the sensors we dropped the weight 5 times consecutively on the same sensor. The results from this test can be seen in Figure 5.6b. The highest percentage error in this case was 16%.

This remarkable increase in dipole orientation due to in-situ poling shows that it is not just the fraction of β-phase that dictates the piezoelectric properties, but also the orientation of the available β-phase.[32, 33] It should thus be noted that the application of an electric field did significantly augment the piezoelectric properties in the films irrespective of the content of β-phase available. Although the films fabricated from the NC at 1 MV m^{-1} exhibited the highest piezoelectric properties,[33] frequent breakdown of the films during the printing process leading to large variability in the properties restricts their utility. Thus, all the applications in this work were carried out with the NC films fabricated at 0.3 MV m^{-1}.

Gait Monitoring Sensor

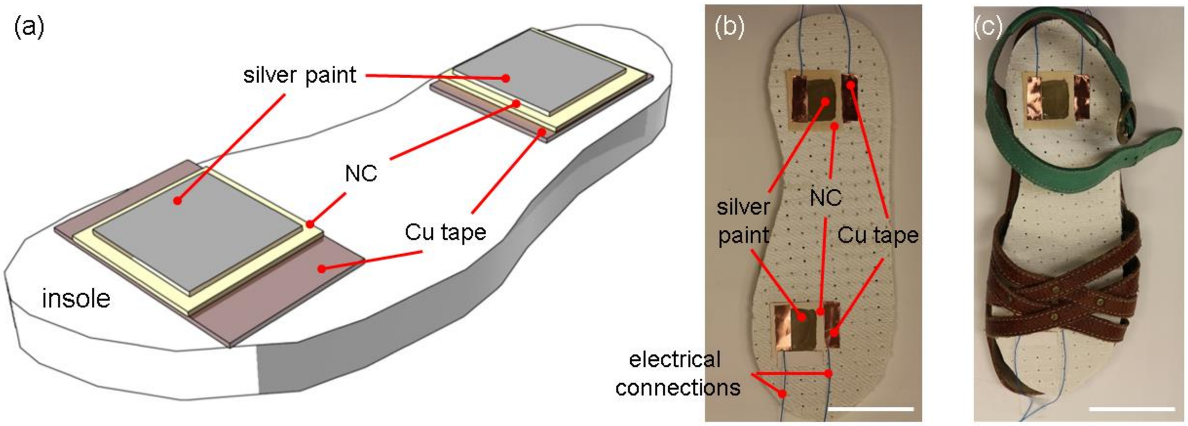

Figure 5.7: (a) Schematic of the sensors printed on a shoe insole (not to scale), (b) Photograph of the sensors printed on the shoe insole and (c) the shoe insole placed into a shoe

Gait analysis is mostly carried out in two ways: (i) when the subject walks on a sensor that is fixed to the ground,[34, 35] and (ii) when the sensor is placed inside the subject's shoe. [3, 36, 37] Piezoelectric sensors were printed on a shoe insole at the fore foot and hind foot locations as seen in Figure 5.7. Figure 5.7a shows a schematic of the sensor to reveal the components clearly. Figure 5.7.b is a photograph of the actual insole with the sensors and the electrical connections. Figure 5.7c shows the insole placed in an open shoe that was worn by the subject during the following tests. Experiments were conducted in two ways: (i) by placing the insole in the subject's shoe and (ii) testing barefoot when the insole was fixed to the ground. Figure 5.8 presents the signals of the fore and the hind sensors when the insole was worn in the shoe. During a normal walking motion (seen from insets in Figure 5.8a), the hind foot lifts first, leaving the fore foot still in contact with the floor showing a small peak in the fore foot voltage. The voltage goes close to zero as the entire foot is lifted. In the next cycle the fore foot makes the initial contact with the floor, and then the hind foot lands on the floor.[38] Thus, the voltage response (Figure 5.8a and 5.8c) from the fore foot sensor shows a larger sharp peak while touching the ground and a smaller peak upon release. The larger negative peak occurs when the shoe hits the ground whereas the smaller negative peak is the response from the pressure between the foot and

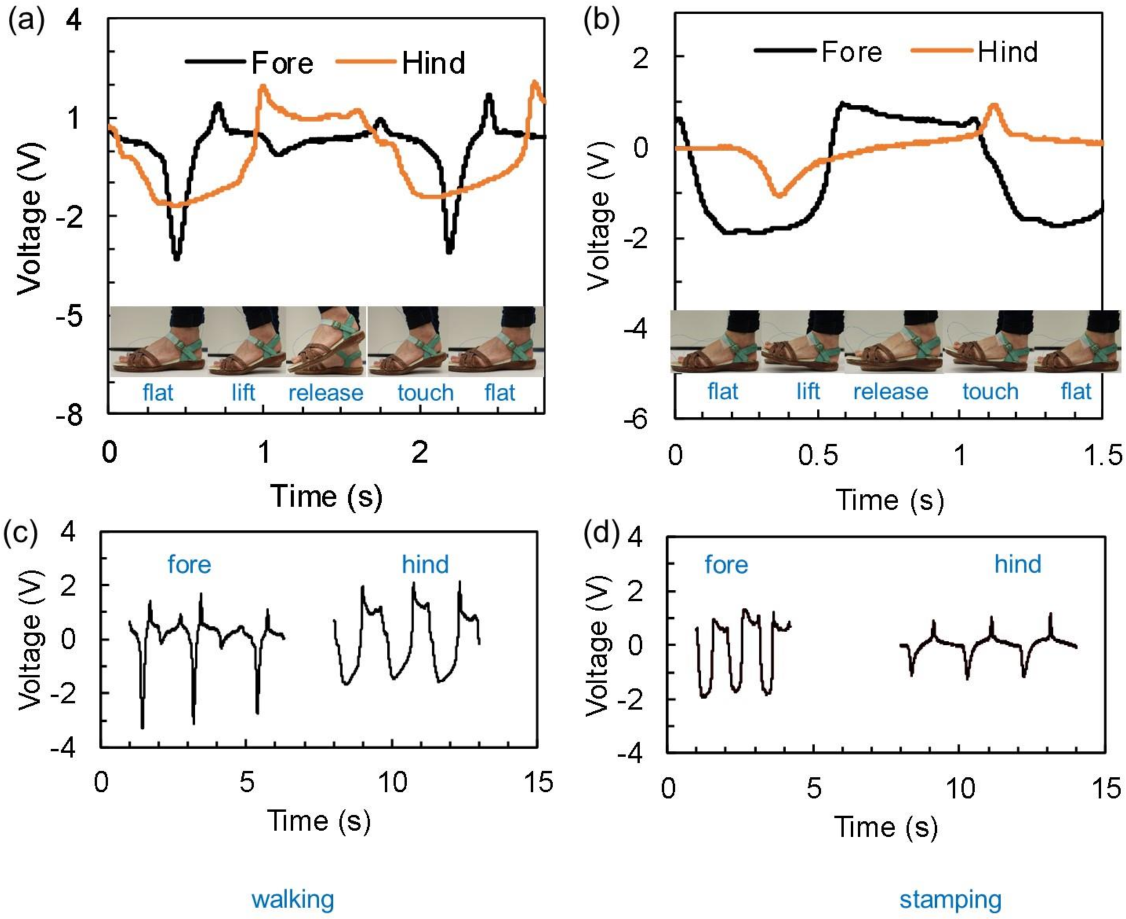

Figure 5.8: Piezoelectric voltage output from the sensor when the insole was worn in the shoe. Single cycle output while (a) walking and (b) stamping. Insets shows the photographs of the movements. Output from the sensor for three consecutive cycles while (c) walking and (d) stamping. Piezoelectric voltage output from the sensor when the insole was worn in the shoe. Single cycle output while (a) walking and (b) stamping. Insets shows the photographs of the movements. Output from the sensor for three consecutive cycles while (c) walking and (d) stamping

the shoe during the swing movement upon the foot’s removal. The broader and flatter response from the hind foot when the foot is on the ground shows the portion where the hind foot provides stability during locomotion. As opposed to walking, stamping (Figure 5.8b) involved the application of the force more at the hind foot location (sharp peaks in the voltage response) as compared to the fore foot as explained by the curves and images in Figure 5.8b and d, respectively. Here, the response from the hind foot is lower in magnitude but sharper than that from the fore foot.

Section 5.7 in SI shows the voltage response from the sensors when the insole was fixed to the ground as a floor-based gait sensor.[39] The voltage responses are much higher in magnitude in this case as compared with those when the insole was worn in the shoe. This could be because the ground reaction forces acting on the foot are much reduced when the insole is in the shoe due to the cushioning effect of the shoe padding. For the same reason the response directions could be reversed in case of the hind foot sensor. Thus, depending on the type of the response and its magnitude, the sensors fabricated in this work can be applied for gait monitoring. Gait sensors made from piezoelectric materials act as active sensors, not requiring any external power sources for operation as compared to their present resistive counterparts. [3, 37, 40].

3D Printing of Structures

3D printing of polymer solutions strongly depends on the solution viscosity. We carried out a comprehensive characterization of the rheological behavior of PVDF and the NC solution [11] for solvent-evaporation based printing methods (details and test results in SI). The viscosity study helped establish a guideline in terms of solution concentrations required to print certain structures. It was found that the concentration of 0.2 g mL^{-1} is most suitable to form void free thin films while certain concentrations below this threshold are too runny to print. As the concentration is increased beyond 0.25 g mL^{-1}, multi-layered structures can be fabricated from both PVDF and its NC inks. Figure 5.9 shows two types of 40-layered structures fabricated using both the PVDF and its NC inks (Figure 5.9 a, b, d and e). Figure 5.9c and 5.9f are self-supporting 3D scaffolds with distinct adjacent layers. The PVDF scaffold was printed with 0.275 g mL^{-1} solution while NC scaffold was printed with 0.3 g mL^{-1} solution. It is because the addition of NP to PVDF resulted in a decrease in the mass of the polymer in the solution, retarding the evaporation of the solvents. Both the polymer and its nanocomposite can thus be used to fabricate piezoelectric 3D structures.

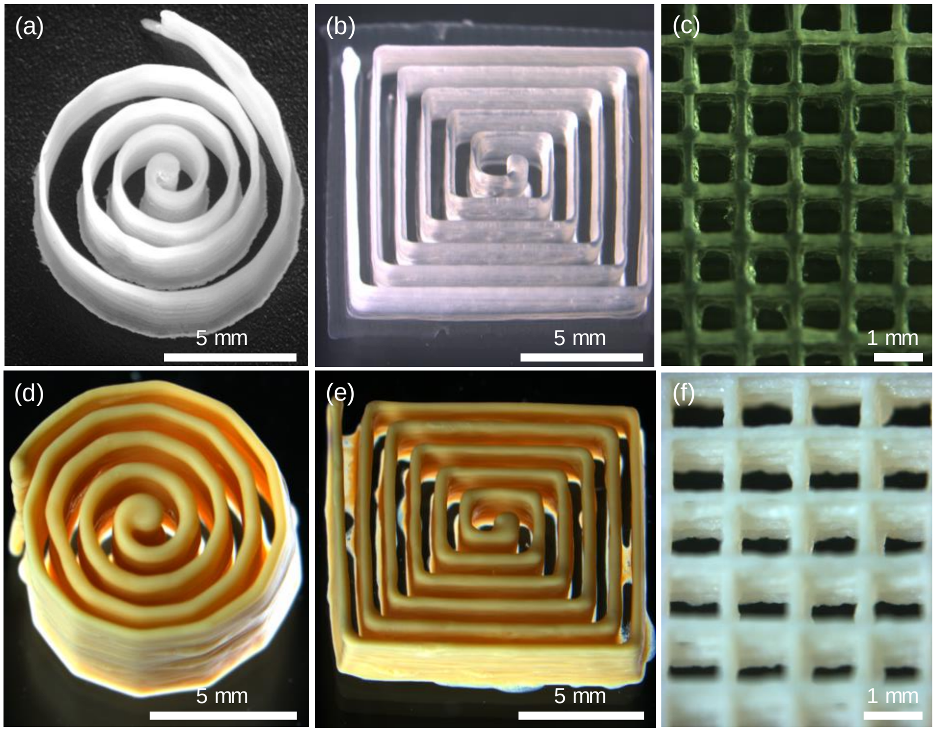

Figure 5.9: Optical images of 3D structures fabricated with P (a) a 40 layer circular spiral (0.25 g mL^{-1} PVDF solution; 0.5 MPa; 1 mm s^{-1}; 100 µm); (b) a 40 layer square spiral (0.25 g mL^{-1} PVDF solution; 0.5 MPa; 1 mm s^{-1}; 100 µm); (c) a 9 layer scaffold (0.3 g mL^{-1} PVDF solution; 0.2 MPa; 3 mm s^{-1}; 150 µm). Structures fabricated with NC: (d) a 40 layer circular spiral (0.25 g mL^{-1} NC solution; 0.5 MPa; 1 mm s^{-1}; 100 µm); (e) a 40 layer square spiral (0.25 g mL^{-1} NC solution; 0.5 MPa; 1 mm s^{-1}; 100 µm); (f) a 9 layer scaffold (0.3 g mL^{-1} NC solution; 1.3 MPa; 13 mm s^{-1}; 250 µm)

Conformal Sensors

The ability to fabricate conformal sensors is further demonstrated in Figure 5.10a. Here, a sensor is printed on a hemisphere (diameter = 30 mm). When gently pressed with the finger as shown in Figure 5.10b, the sensor generated voltages up to 7 V (Figure 5.10c, peak to peak ~8V). The voltage peaked on touching the sensor. Upon removal of the force the charges started flowing in the negative direction. This is the first working example of conformally printed piezoelectric sensors.

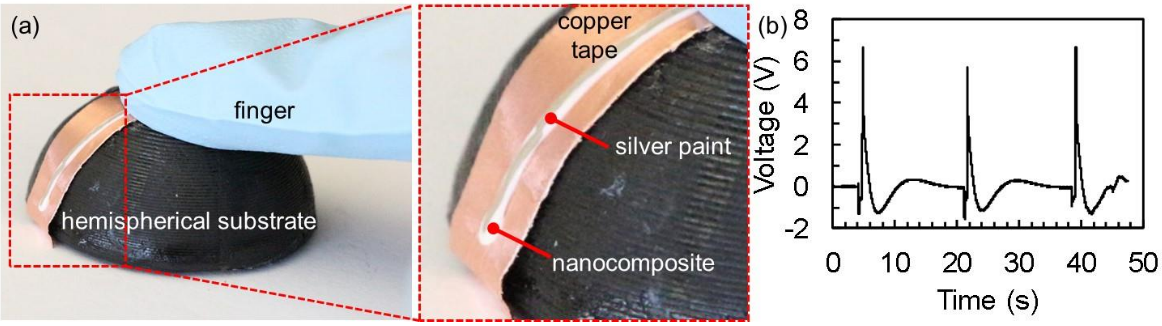

Figure 5.10: (a) Optical images of a conformal sensor fabricated with the NC pressed by an index finger. (0.2 g mL^{-1} PVDF solution; 0.15 MPa; 2 mm s^{-1}; 100 µm). (b) Voltage output of the sensor when pressed with the finger 3 times

5.4 Conclusions

A simultaneous 3D printing and electrical poling process was demonstrated for PVDF and its nanocomposite containing 10 wt. % of $BatiO_3$ NPs with electric fields up to $1MV^{-1}$. This combination produced a 300% increase in polarization in the poled nanocomposite over unpoled PVDF. The fraction of β-phase in poled nanocomposites of PVDF remained close to 71 %, indicating that the remarkable increase in polarization mainly stems from the poling-aligned PVDF chains. Process-related viscosity behavior of the PVDF solution showed that the printable concentrations range from 0.2 to 0.3 g mL^{-1}. Different 3D structures, both self-supported and conformal were printed to demonstrate the flexibility and scope of the printing method. Gait-monitoring sensors were printed on a shoe insole and tested while walking and stamping. Sensors on a shoe insole can be a very convenient option for the user as the same insole could be switched between various shoes,[37] and used to collect data for a longer duration whereas the platform sensors could be used in a test facility for multiple users. The sensors effectively differentiated between walking and stamping for both the front foot and hind foot locations.

5.5 Acknowledgements

The authors acknowledge the financial support from NSERC #RGPIN3212568-2013 (Natural Sciences and Engineering Research Council of Canada) and Canada Research Chair #CRC950-216943.

5.6 Printing sensors on shoe insole

Figure 5.11 shows the process of sensor fabrication and instrumentation on the shoe insole.

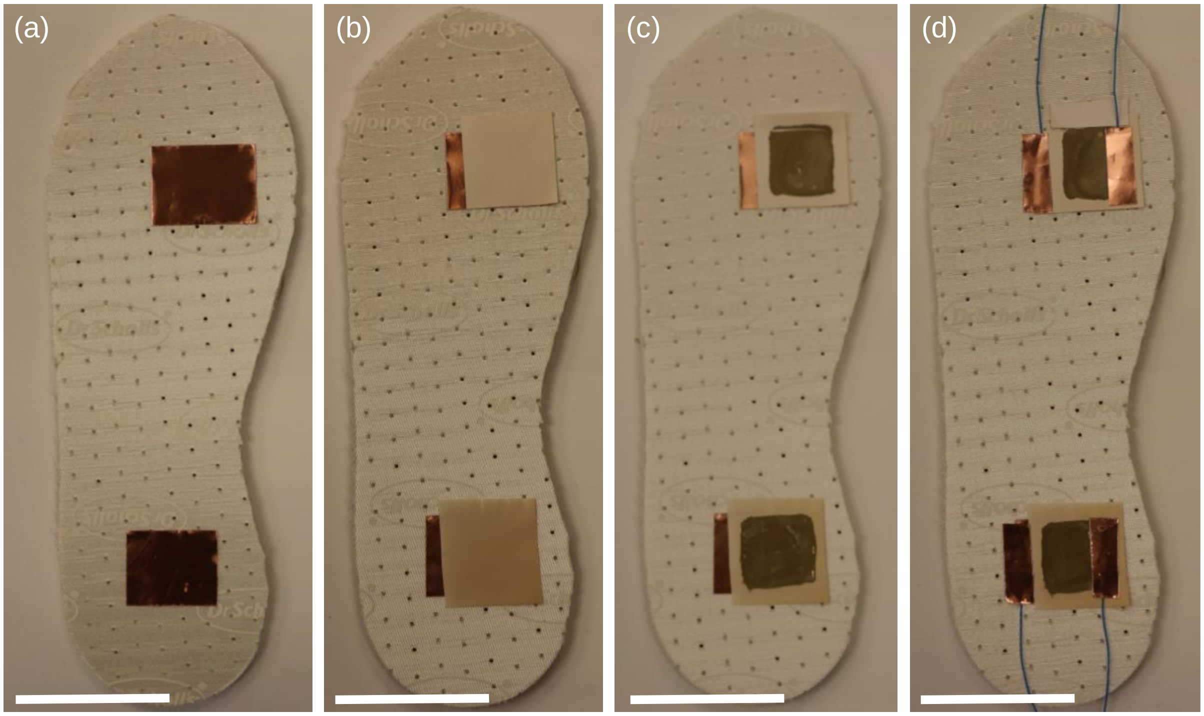

Figure 5.11: Sensor fabrication on the insole: (a) Cu tape attached at metatarsal and heel regions on the insole to act as lower electrodes, (b) NC printed with an electric field of 0.3 MV m-1, (c) silver electrodes painted on the sensors as top electrodes, and (d) wires connected to the top and bottom electrodes using Cu tape for data acquisition (scale bar = 5 cm)

5.7 Tests with shoe insole fixed to the ground

Figure 5.12a and 5.12b explain the voltage response with the positions of the foot on the sensor while walking and stamping, respectively for one complete cycle. Figure 5.12c and 5.12d provide the voltage response for 3 complete cycles. The out-of-phase response in these set of tests can be attributed to the fact that as the sensor is placed on the ground the landing of the fore and the hind foot on the sensors are not very well synchronized.

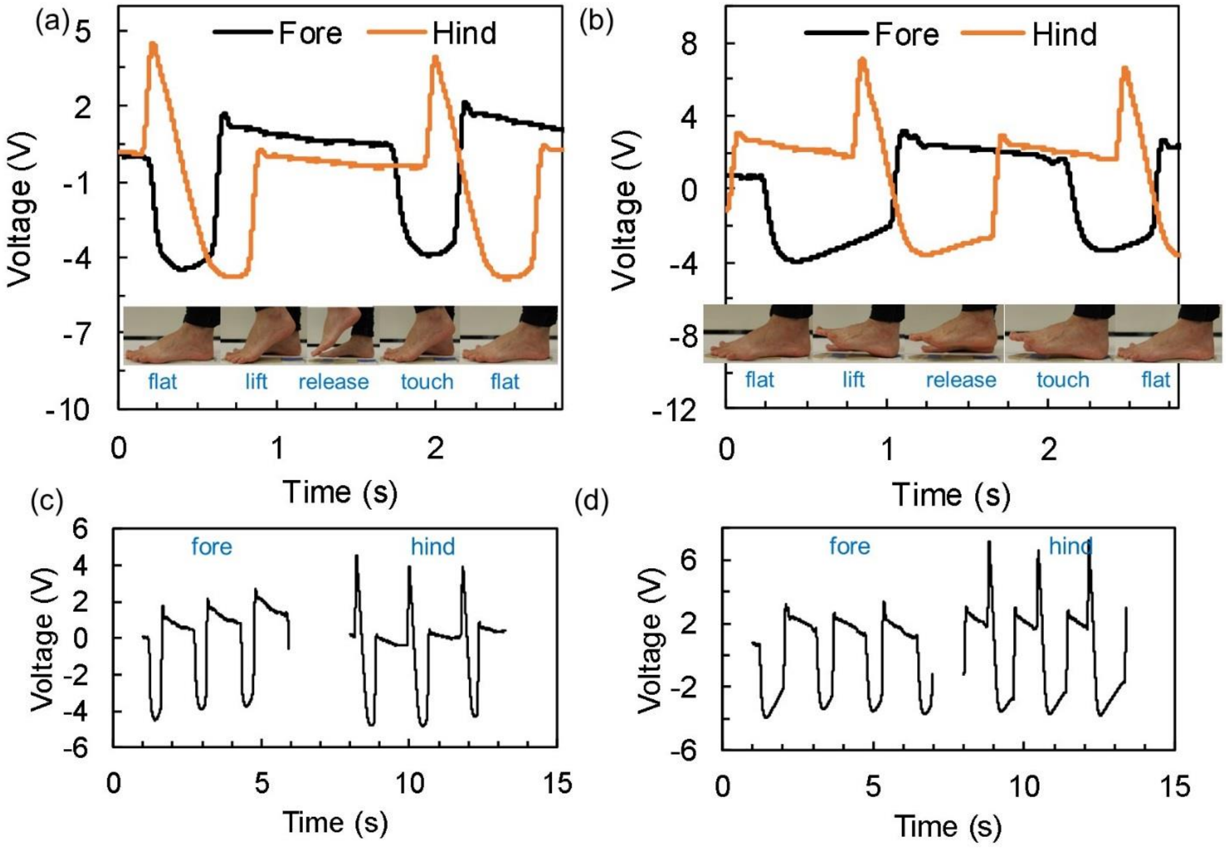

Figure 5.12: Piezoelectric voltage output from the sensor when the insole was fixed to the ground. Single cycle output from the sensor while (a) walking and (b) stamping. Insets shows the photographs of the movements. Output from the sensor for three consecutive cycles while (c) walking and (d) stamping

5.8 Process viscosity characterization of PVDF nanocomposites prepared by ball-milling

It is essential to study the rheological characteristics of a solution, as it determines the behavior of the solution under applied shear during extrusion-based printing. This helps the user to establish a printing regime depending on the application. Various concentrations of PVDF in DMF/acetone mixture: 0.15 – 0.3 g mL^{-1} (keeping the DMSO constant) were studied for their printability.

The effect of shear stress (extrusion pressure) and shear rate (printing speed) on the apparent viscosity of six different concentrations (0.15–0.3 g mL^{-1}) of PVDF in solvent mixture were studied via capillary flow analysis as reported in Guo et al.[41] Polymer filaments, 60 mm in length were deposited using a 100 μm diameter nozzle at different extrusion pressures (moving platform velocity = 0.5 mm s^{-1}) with the PVDF solutions. Five fibers were printed at each pressure for every solution. A weighing scale (GH200, A&D) was used to determine the mass of the fibers after complete evaporation of the solvents (after 24 h).

To calculate the apparent viscosity of the solutions, shear stress τ_w was calculated from the applied pressures (neglecting the capillary effects as L/D > 50) [42] with the formula,[41]

$$\tau_w = \Delta P.\frac{D}{4L} \tag{5.4}$$

where, ΔP is the difference between the applied pressure and atmospheric pressure.

The Newtonian shear rate is then given by

$$\gamma'_{Newt} = \frac{4Q}{\pi(\frac{D}{2})^3} \tag{5.5}$$

where, *Q* is the volumetric flow rate. To obtain the actual shear rate at the point of extrusion, we use Rabinowitch-Mooney correction parameter *n* defined by,

$$n = \frac{d\log(\tau_w)}{d\log(\gamma'_{Newt})} \tag{5.6}$$

which is obtained from the slope of the log-log plot of shear stress versus Newtonian shear rate. Then the shear rate is calculated by,

$$\gamma' = \gamma'_{Newt}\frac{3n+1}{4n} \tag{5.7}$$

Finally, the apparent viscosity η_{app} is calculated as,

$$\eta_{app} = \frac{\tau_w}{\gamma'} \tag{5.8}$$

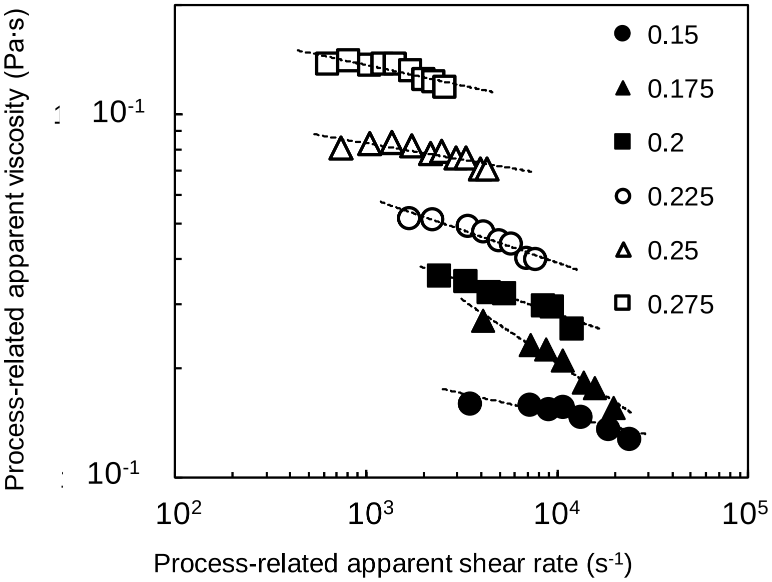

Figure 5.13: Process-related apparent viscosity versus process-related apparent shear rate curves of 0.150 to 0.275 g mL-1 PVDF solutions

The values of process-related viscosity as a function of process-related shear rate for the PVDF solutions can be seen in Figure 5.13. All the inks exhibit a shear-thinning behavior, characterized by a decrease in viscosity with applied shear stress, essential for extrusion based printing. This property aids a high viscosity solution to pass through a thin-long nozzle and then regain its viscosity as the shear stress is relieved as soon as the material exits the nozzle. The increased viscosity helps in shape retention post-extrusion. Figure S5.3 shows that the PVDF solutions tend to move closer to a Newtonian behavior as the concentration of PVDF is increased in the solvent-system. This restricts the printable concentrations to 0.25 g mL^{-1}. The process-related viscosity behavior for the nanocomposite was reported in other work.[11]

Reference:

[1] C. Wan and C. R. Bowen, "Multiscale-structuring of polyvinylidene fluoride for energy harvesting: the impact of molecular-, micro- and macro-structure," *Journal of Materials Chemistry A*, vol. 5, pp. 3091-3128, 2017.

[2] L. Xie, X. Huang, K. Yang, S. Li, and P. Jiang, ""Grafting to" route to PVDF-HFP-GMA/BaTiO3 nanocomposites with high dielectric constant and high thermal

conductivity for energy storage and thermal management applications," *Journal of Materials Chemistry A,* vol. 2, pp. 5244-5251, 2014.

[3] Y. Li, Y. A. Samad, and K. Liao, "From cotton to wearable pressure sensor," *Journal of Materials Chemistry A,* vol. 3, pp. 2181-2187, 2015.

[4] P. C. A. Ferreira, H. Carvalho, J. M. Nobrega, V. Sencadas and a. S. Lanceros-Mendez, "Extrusion of poly(vinylidene fluoride) filaments: Effect of the processing conditions and conductive inner core on the electroactive phase content and mechanical properties," *Journal of Polymer Research,* vol. 18, p. 8, 2011.

[5] A. Lund and B. Hagström, "Melt spinning of poly(vinylidene fluoride) fibers and the influence of spinning parameters on β-phase crystallinity," *Journal of Applied Polymer Science,* vol. 116, pp. 2685-2693, 2010.

[6] K. Seok Ju, P. Youn Jung, J. Sung, P. S. Jo, P. Cheolmin, K. J. Kim*, et al.,* "Spin cast ferroelectric beta poly(vinylidene fluoride) thin films via rapid thermal annealing," *Applied Physics Letters,* vol. 92, pp. 012921-012921-3, 2008.

[7] J. C. C. Ferreira, T. S. Monteiro, A. C. Lopes, C. M. Costa, M. M. Silva, A. V. Machado, *et al.,* "Variation of the physicochemical and morphological characteristics of solvent casted poly(vinylidene fluoride) along its binary phase diagram with dimethylformamide," *Journal of Non-Crystalline Solids,* vol. 412, pp. 16-23, 3/15/ 2015.

[8] C. Seoul, Y.-T. Kim, and C.-K. Baek, "Electrospinning of poly(vinylidene fluoride)/dimethylformamide solutions with carbon nanotubes," *Journal of Polymer Science Part B: Polymer Physics,* vol. 41, pp. 1572-1577, 2003.

[9] F. Yiin-Kuen, H. Hsi-Chun, W. Bo-Sheng, and L. Shan-Chien, "All-fiber transparent piezoelectric harvester with a cooperatively enhanced structure," *Nanotechnology,* vol. 27, p. 435403, 2016.

[10] G. Luo, K. S. Teh, Y. Liu, X. Zang, Z. Wen, and L. Lin, "Direct-Write, Self-Aligned Electrospinning on Paper for Controllable Fabrication of Three-Dimensional Structures," *ACS Applied Materials & Interfaces,* vol. 7, pp. 27765-27770, 2015/12/23 2015.

[11] S. Bodkhe, G. Turcot, F. P. Gosselin, and D. Therriault, "One-Step Solvent Evaporation-Assisted 3D Printing of Piezoelectric PVDF Nanocomposite Structures," *Acs Applied Materials & Interfaces,* vol. 9, pp. 20833-20842, Jun 21 2017.

[12] C. Lee and J. A. Tarbutton, "Electric poling-assisted additive manufacturing process for PVDF polymer-based piezoelectric device applications," *Smart Materials and Structures*, vol. 23, p. 095044, 2014.

[13] C.-T. Pan, C.-K. Yen, H.-C. Wu, L. Lin, Y.-S. Lu, J. C.-C. Huang, *et al.*, "Significant piezoelectric and energy harvesting enhancement of poly(vinylidene fluoride)/polypeptide fiber composites prepared through near-field electrospinning," *Journal of Materials Chemistry A*, vol. 3, pp. 6835-6843, 2015.

[14] S. Bodkhe, C. Noonan, F. P. Gosselin, and D. Therriault, "Coextrusion of multifunctional smart sensors," *Submitted to Nature Materials*, 2017.

[15] K. Hoejin, T. Fernando, W. Yanyu, V. Dino, L. Yirong, and T. Tzu-Liang, "Integrated 3D printing and corona poling process of PVDF piezoelectric films for pressure sensor application," *Smart Materials and Structures,* vol. 26, p. 085027, 2017.

[16] S. P. Division, "Piezo Film Sensors Technical Manual," Measurement Specialties, Inc, Norristown, PA 1999.

[17] S. Koombhongse, W. Liu, and D. H. Reneker, "Flat polymer ribbons and other shapes by electrospinning," *Journal of Polymer Science Part B: Polymer Physics,* vol. 39, pp. 2598-2606, 2001.

[18] A. Aesar, "A13547 N,N-Dimethylformamide, 99%," A. A. (R), Ed., ed, 2017.

[19] S. Bodkhe, F. P. Gosselin, and D. Therriault, "Three-dimensional printing of polyvinylidene fluoride nanocomposites," in *20th International Conference on Composite Materials*, Copenhagen, Denmark, 2015, p. 9.

[20] M. Benz, W. B. Euler, and O. J. Gregory, "The Role of Solution Phase Water on the Deposition of Thin Films of Poly(vinylidene fluoride)," *Macromolecules,* vol. 35, pp. 2682-2688, 2002/03/01 2002.

[21] G. M. Sessler, "Piezoelectricity in polyvinylidenefluoride," *The Journal of the Acoustical Society of America,* vol. 70, pp. 1596-1608, 1981.

[22] D. M. Esterly and B. J. Love, "Phase transformation to β-poly(vinylidene fluoride) by milling," *Journal of Polymer Science Part B: Polymer Physics,* vol. 42, pp. 91-97, 2004.

[23] R. Gregorio, "Determination of the α, β, and γ crystalline phases of poly(vinylidene fluoride) films prepared at different conditions," *Journal of Applied Polymer Science,* vol. 100, pp. 3272-3279, 2006.

[24] G. Mago, D. M. Kalyon, and F. T. Fisher, "Membranes of Polyvinylidene Fluoride and PVDF Nanocomposites with Carbon Nanotubes via Immersion Precipitation," *Journal of Nanomaterials,* vol. 2008, 2008.

[25] S. Nayak, B. Sahoo, T. K. Chaki, and D. Khastgir, "Facile preparation of uniform barium titanate (BaTiO3) multipods with high permittivity: impedance and temperature dependent dielectric behavior," *RSC Advances,* vol. 4, pp. 1212-1224, 2014.

[26] T. Boccaccio, A. Bottino, G. Capannelli, and P. Piaggio, "Characterization of PVDF membranes by vibrational spectroscopy," *Journal of Membrane Science,* vol. 210, pp. 315-329, 12/15/ 2002.

[27] J. R. Gregorio and M. Cestari, "Effect of crystallization temperature on the crystalline phase content and morphology of poly(vinylidene fluoride)," *Journal of Polymer Science Part B: Polymer Physics,* vol. 32, pp. 859-870, 1994.

[28] K. M. Suresha, B. John, W. Konrad, and S. Boris, "Effect of poling time and grid voltage on phase transition and piezoelectricity of poly(vinyledene fluoride) thin films using corona poling," *Journal of Physics D: Applied Physics,* vol. 46, p. 285305, 2013.

[29] Y. Xi, H. Fan, W. Li, and X. Niu, "Effect of corona poling on structure evolutions of α-phase and β-phase PVDF films," in *5th International Symposium on Advanced Optical Manufacturing and Testing Technologies*, 2010, p. 6.

[30] J. P. Luongo, "Far-infrared spectra of piezoelectric polyvinylidene fluoride," *Journal of Polymer Science Part A-2: Polymer Physics*, vol. 10, pp. 1119-1123, 1972.

[31] G. Neumann, E. Bihler, G. Eberle, and W. Eisenmenger, "Polarization distribution in PVDF obtained by poling under constant current condition," in *Electrical Insulation and Dielectric Phenomena, 1990. Annual Report., Conference on*, 1990, pp. 96-101.

[32] Y. Huan, Y. Liu, and Y. Yang, "Simultaneous stretching and static electric field poling of poly(vinylidene fluoride-hexafluoropropylene) copolymer films," *Polymer Engineering & Science,* vol. 47, pp. 1630-1633, 2007.

[33] D. Geiss, R. Danz, A. Janke, and W. Kunstler, "Field induced structure transition in poly (vinylidene fluoride)," in *5th International Symposium on Electrets (ISE 5),* 1985.

[34] T. Keatsamarn and C. Pintavirooj, "Foot plantar pressure measurement system using optical sensor," in *9th Biomedical Engineering International Conference* 2016.

[35] B. A. MacWilliams and P. F. Armstrong, "Clinical applications of plantar pressure measurement in pediatric orthopedics," in *Pediatric Gait: A New Millennium in Clinical Care and Motion Analysis Technology* Chicago, IL, USA, USA, 2000.

[36] A. H. Abdul Razak, A. Zayegh, R. K. Begg, and Y. Wahab, "Foot Plantar Pressure Measurement System: A Review," *Sensors,* vol. 12, p. 9884, 2012.

[37] J. J. Wertsch, J. G. Webster, and W. J. Tompkins, "A portable insole plantar pressure measurement system," *Journal of Rehabilitation Research and Development,* vol. 29, pp. 13-18 1992.

[38] D.-H. Lim, W.-S. Kim, H.-J. Kim, and C.-S. Han, "Development of real-time gait phase detection system for a lower extremity exoskeleton robot," *International Journal of Precision Engineering and Manufacturing,* vol. 18, pp. 681-687, 2017.

[39] R. W. Soames, "Foot pressure patterns during gait," *Medical Engineering and Physics,* vol. 7, pp. 120-126.

[40] G. A, "Pressure-sensing devices for assessment of soft tissue loading under bony prominences: Technological concepts and clinical utilization," *Wounds,* vol. 19, pp. 350–362, 2007.

[41] S.-Z. Guo, M.-C. Heuzey, and D. Therriault, "Properties of Polylactide Inks for Solvent-Cast Printing of Three-Dimensional Freeform Microstructures," *Langmuir,* vol. 30, pp. 1142-1150, 2014/02/04 2014.

[42] J. Bruneaux, D. Therriault, and M.-C. Heuzey, "Micro-extrusion of organic inks for direct-write assembly," *Journal of Micromechanics and Microengineering,* vol. 18, p. 11, 7 October 2008 2008.

CHAPTER 6 ARTICLE 3: COEXTRUSION OF MULTIFUNCTIONAL SMART SENSORS

Sampada Bodkhe, Clara Noonan, Frederick P. Gosselin, and Daniel Therriault*

Submitted to Nature Materials, 8th Novembre 2017.

Abstract

Three-dimensional (3D) printing of a piezoelectric sensor conventionally involves: fabrication of the sensor followed by electrode deposition and electrical poling. Here, we report a novel approach to simultaneously fabricate a piezoelectric sensor with its two silver electrodes in a single step, using a piezoelectric nanocomposite ink, formulated and processed to work without the need for poling. We then employ solvent evaporation-assisted 3D printing to coextrude ready-to-use conformal sensors, self-supported vertical pillars, and spanning filaments. We present applications as aero-elastic sensors and smart active thread for wearables. We print sensors directly on fused deposition modelling printed miniature wings to monitor aero-elastic stability. In another application, we use the coextruded filament in the form of a piezoelectric thread as wearable sensors for knee-joint and respiration monitoring. The self-powered piezoelectric sensing elements are an attractive alternative for customized, multi-material applications where each watt and each gram counts such as wearables, and micro-drones.

6.1 Main text

Piezoelectric sensors generate electric signals linearly proportional to mechanical deformation. Their advantages of larger band-width, low-response time, and low operational costs[1] present applications in wearable electronics, structural health monitoring, vibration control, prosthetics, acoustics, tissue engineering, and energy harvesting. Ceramics have dominated the piezoelectric market for decades due to the inefficiency of the piezoelectric polymers. Biocompatible, compliant, conformal and tough piezoelectric ceramic composites with polymers now overcome the limitations of brittle and rigid ceramics.[2-6] However, things have not changed much in the form in which sensors continue to be fabricated: fibers [7, 8] or films.[6, 9] The sensors are then either bonded,[10, 11] or strapped [12] at the sensing locations increasing non-conformability with the substrate, thus leading to inconsistent and erroneous results. Furthermore, electrodes to collect the generated charges are typically coated,[13] screen-printed,[11] or deposited [14] which is multi-stepped, time-consuming, and arduous for miniature slender structures. Conventional piezoelectric sensor fabrication processes entail additional poling steps, and often necessitate clean-room environment, which form a bottleneck in an industry setting. It is thus exigent to devise a process adept to industrial production. We proffer an unprecedented technique to three-dimensionally (3D) print flexible piezoelectric sensors with two co-fabricated electrodes in a single step quintessential for integrated and complex shaped sensors and present their applications on two fronts: wearable electronics and aero-elastic monitoring.

Wearable sensors are increasingly sought after over conventional ambulatory diagnostics for monitoring vital signs in military, sports, and rehabilitation prosthetics owing to their foremost advantage of real-time unobtrusive electrophysiological analysis combined with low cost (over 10 times lower), portability, and versatility.[15, 16] Present day wearable sensors rely on resistive[17-20] or capacitive[21, 22] technology operating with bulky batteries that need to be frequently recharged and replaced, whereas piezoelectric sensors serve as self-powered alternatives.[2, 6, 23] The components – electronics and multi-functional materials (material–making the clothing intelligent), are either embedded or woven in the fabric or directly embedded into the fibers themselves.[24] To apply the piezoelectric fiber into smart textiles, its diameter needs to match that of the fabric's thread. Unlike the metallic resistive sensors, the piezoelectric sensor requires two electrodes to collect and transport the generated charges. However, coating, and depositing electrodes form additional processing steps.

Remote monitoring is imperative to extract information about the environment, flight conditions and structural damage to complement the performance of air-vehicles and automobile. The weight and aerodynamics are paramount to the structures, along with mechanical durability and smooth functioning in isolated locations inaccessible to power.[25, 26] 3D printing of piezoelectric materials serves as an apt tool to co-integrate sensors directly on the surface or embed them inside the parts to be monitored.

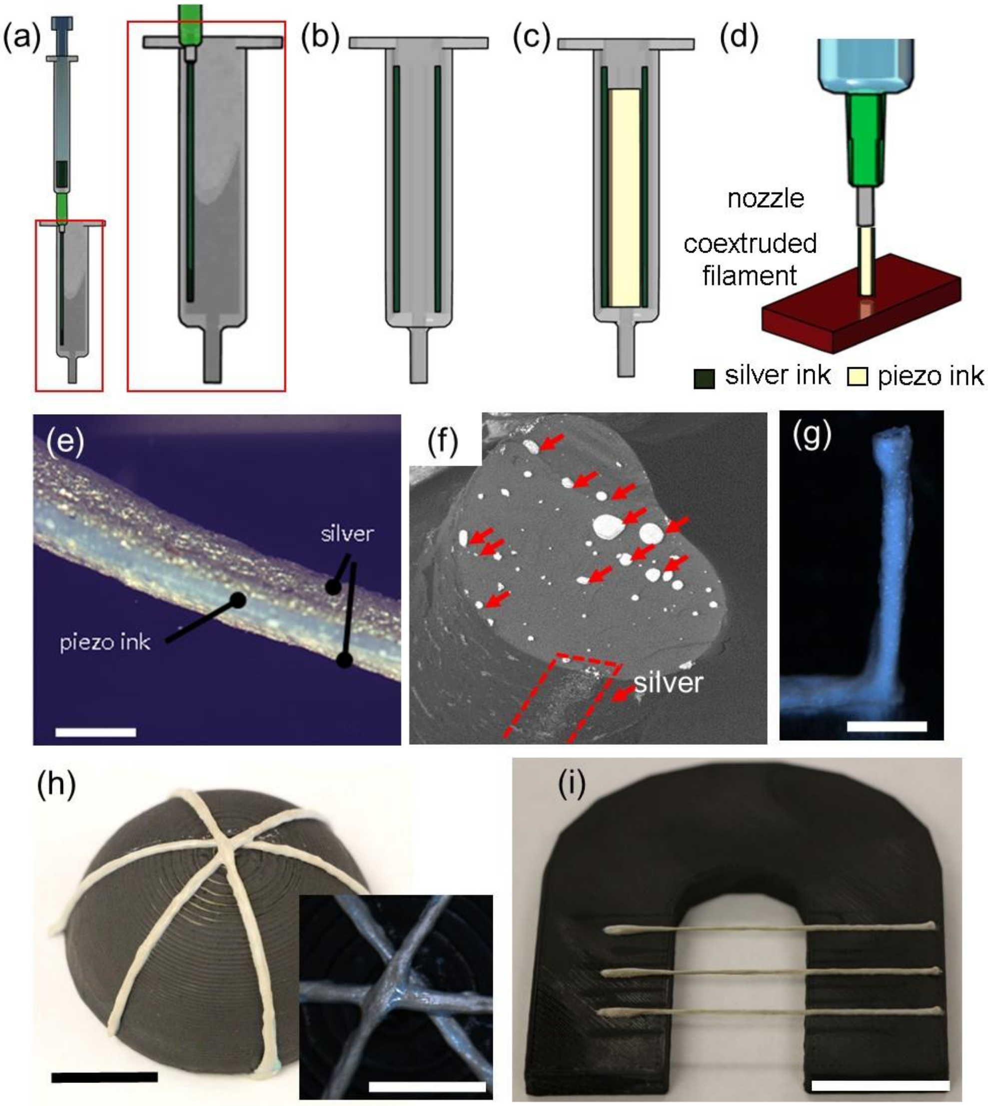

Figure 6.1: Schematic of the coextrusion process. a) cut-section of the syringe showing the painting of a silver filament on the wall; b) painting a second silver filament 180° apart along the circumference of the syringe; c) filling the syringe with the piezoelectric ink; d) coextruding the two inks from the syringe; e) microscopic image of the piezoelectric thread (scale bar = 500 µm); f) SEM image of the cold fractured cross-section of the coextruded filament (scale bar = 100 µm), major NP agglomerates are indicated with red arrows, and the silver electrode is highlighted with a red border; g) microscopic image of coextruded vertical pillar (scale bar = 2 mm); h) photograph of coextruded conformal sensors printed on a hemisphere (scale bar = 5 mm), inset: microscopic image of the top view of the hemisphere (scale bar = 5 mm); and i) coextruded spanning filaments (scale bar = 20 mm). (Printing parameters: nozzle diameter 840 µm, extrusion pressure = 0.04 – 0.2 MPa, speed = 2 – 20mm s^{-1})

In this paper, we report one-step fabrication of self-powered piezoelectric sensors with coextruded electrodes on 3D printed wings and as active threads directly woven into intelligent apparels. We investigate the physical properties affecting the printability.

We have recently demonstrated successful 3D printing of a piezoelectric nanocomposite ink with 10 wt.% barium titanate nanoparticles ($BaTiO_3$ NPs) in polyvinylidene fluoride (PVDF) matrix.[27] The as-fabricated 3D structures possessed a d_{31} constant of ~18 pC N^{-1} without any poling. In this work, we first insert a commercial silver ink (MG – 842) along the edges of a syringe (3 mL) using a clinical syringe-needle system (1 mL) to form thin lines of silver on the walls (see Figure 6.1a and b). We then quickly pour a solution of PVDF/ $BaTiO_3$ nanocomposite into the syringe (see Figure 6.1c) to minimize the drying of the silver ink. The process (see Figure 6.1d, Supplementary Movie 1) described in [27] is used to print piezoelectric structures: a filament (see Figure 6.1e and f), a vertical pillar with aspect ratio of 15 (see Figure 6.1g), conformal features on a hemisphere (see Figure 1h) and filaments (print diameter = 0.84 mm) with 20 mm spanning distances (see Figure 6.1i). The SEM image of the cross-section reveals that the silver electrodes were formed on a small region on the outer surface of the filament (EDS details in SI).

For coextrusion without mixing or diffusion of one ink into the other, and to allow continuous extrusion of the two inks at any pressure, the two fluids should have similar rheological behavior.[28] Further, shear thinning behavior in both the inks is significant to attain shape fidelity post-extrusion.[29] Though the viscosities of the two materials vary at the given shear rates (see Figure 6.2a), the curves for the two materials have similar slopes and comparable power law indices, *n*. Rheometer tests on the piezo and silver inks provide the power law indices as 0.77 and 0.79, respectively. Interlayer stability and layer uniformity, i.e., equal flow velocities for both the inks are achievable only when the outer layer has a lower viscosity.[30] It is desirable to extrude the material system at low flow-rates to be in the laminar flow regime, thus avoiding any turbulent mixing of the two materials. The rate of evaporation of the solvents (see Figure 6.2b) in the two inks dominates the shape of the cross-section of the printed filament or structure. Though the evaporation rates are similar at the onset of printing, in the final structure the piezoelectric ink shrinks the most (more than twice) as compared to the silver ink owing to the presence of a significant amount of solvents. We believe that this turns the expected circular cross-section closer to an ellipse (see Figure 1g). Rapid solvent evaporation renders the sensors

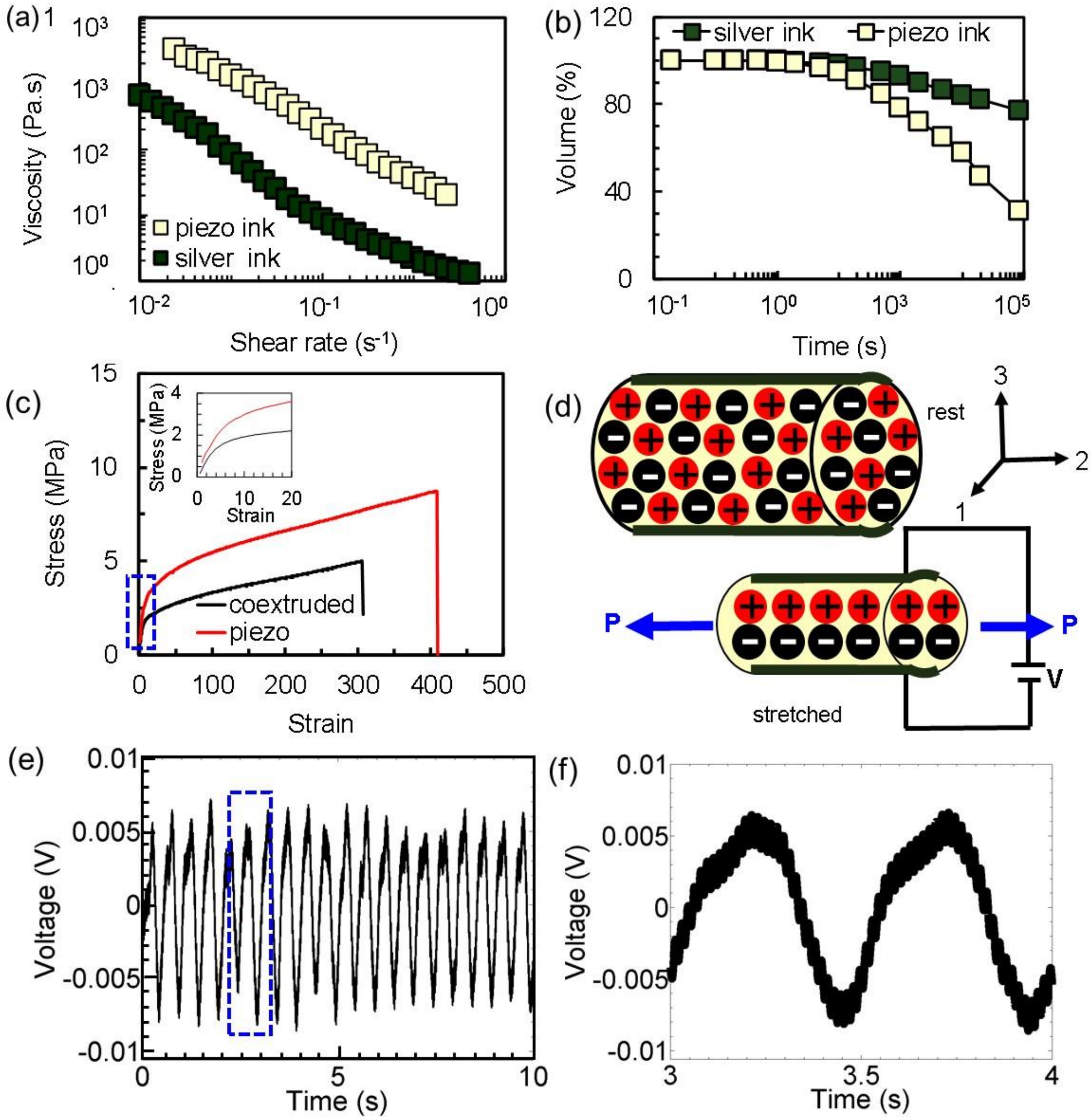

Figure 6.2: a) Log-log plots of viscosity versus shear rate, and b) volumetric shrinkage during the solvent evaporation of piezoelectric and silver inks; c) representative tensile stress versus strain curves of the coextruded and piezoelectric filaments, inset: zoomed in view of the elastic region; d) schematic showing the piezoelectric phenomenon in the thread upon stretching in the longitudinal direction; e) a part of a representative response of one of the threads at 1% applied strain at 2 Hz; f) single cycle voltage output as a function of time during the dynamic piezoelectric test of the thread (zoomed in view of the region in the blue box from 2e)

ready to use right after extrusion. This technique fabricates sensors with feature sizes: 250 µm – 1.5 mm, without intermixing the piezoelectric and the electrode materials.

Keeping silver to a minimum avoids its detrimental effect on the mechanical properties of the fiber. This was confirmed via mechanical tests. The coextruded filament exhibits a decrease in tensile strength (see Figure 6.2c for the stress -strain curve) from 8.1 MPa ± 0.9 MPa to 5.6 MPa ± 0.5 MPa (average of 5 values) and strain at break from 422 % ± 24 % to 296 % ± 20 % as compared with the extruded piezoelectric filament with similar dimensions. The Young’s modulus of the piezoelectric filament is 19.8 MPa ± 2.9 MPa and the one for the coextruded filament is 20.0 MPa ± 3.0 MPa. Both filaments present moduli, implying that electrodes do not significantly affect the compliance of the thread. This low value of elastic modulus results in increased mechanical sensitivity.[9]

Piezoelectric materials are shown to measure the strain up to 1.2 % [9] and most human activities fall in the low frequency range of 0.25 – 2 Hz.[13] We tested the piezoelectric thread under cyclic tensile loading with 1 % strain at a frequency of 2 Hz using a dynamic mechanical analyzer. Figure 6.2e is a representative curve of the piezoelectric output from the sensor with respect to time. As the fiber is stretched along its length, charges are generated across its thickness (see schematic in Figure 6.2d). Figure 6.2f is an enlarged view of the piezoelectric response and the output signal clearly resembles the input sine wave.

To demonstrate the 3D printability of the current system, a aero-elasticity monitoring sensor in the shape of a typical strain gauge was printed on top of a fused deposition modeling (FDM)-printed on a beam shaped-like an insect wing (see Figure 6.3a). We assessed the sensitivity of the sensor to: (i) the magnitude and frequency of the applied forces, (ii) mechanical obstructions, and (iii) any changes in the surrounding wind flow, by mounting the wing on an electromagnetic shaker (see Supplementary Figure 6.6) and exciting it at various forcing frequencies and amplitudes. Figure 6.3b confirms that there was no shorting between the electrodes at the turns and corners of the sensor. The response of the sensor (see Figure 6.3c) to the applied sinusoidal mechanical input (4 Hz) to the shaker was mostly linear as expected of piezoelectric materials. The sensor further reproduced the sinusoidal input very well for all the frequencies tested between 0.2 Hz and 15 Hz; a few of them are presented in Figure 6.3d. We then applied a sinusoidal input of 1 Hz to the wing (see Figure 6.3e and 6.3f). The response in the absence of any external perturbations is a regular sine curve. The sensor picked up physical obstructions (see Figure 6.3e) and flow perturbations (see Figure 6.3f) to the wing as seen by the disturbances in the electrical output signal establishing its applicability for monitoring the aero-elastic behavior of the wing.

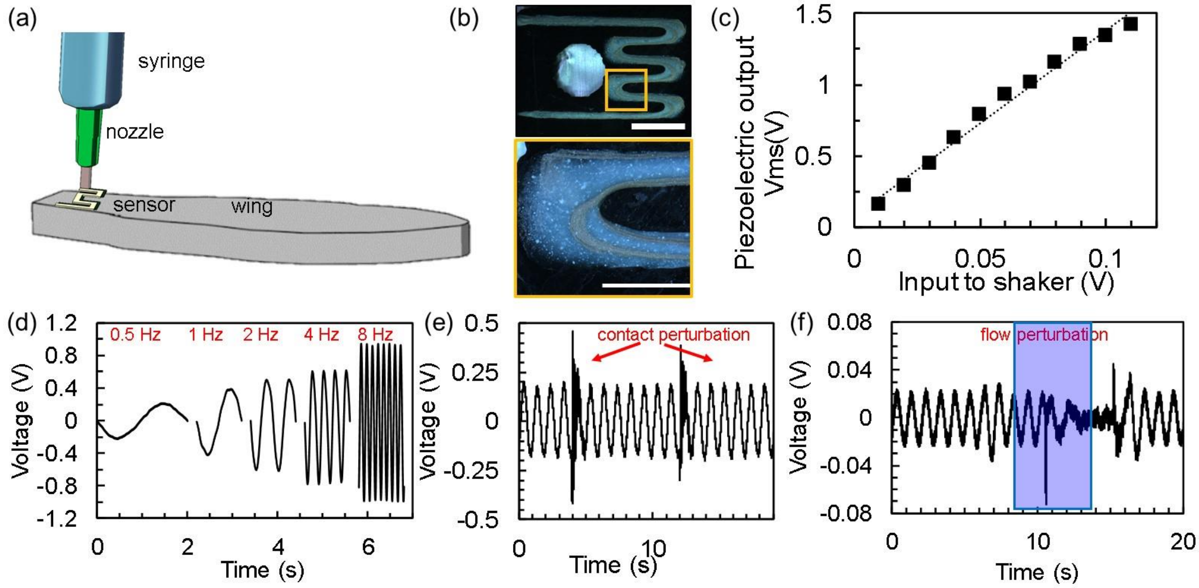

Figure 6.3: a) Schematic of one step sensor being 3D printed on a FDM printed wing; b) microscopic image of the sensor on the wing (top) and enlarged view of the sensor showing the piezoelectric material (white) and two silver electrodes; c) piezoelectric voltage (RMS) output from the sensor as a function of voltage input to an electromagnetic shaker (frequency = 4 Hz), d) output voltage responses for 0.5, 1, 2, 4 and 8 Hz input frequencies to the wing with an input amplitude of 0.05 V to the shaker; variation in the response of the sensor when disturbed e) mechanically and f) aerodynamically (shaker input frequency = 1 Hz; amplitude = 0.05 V)

We wove the extruded flexible piezoelectric thread into garments to form self-powered miniature wearable sensors for smart textiles. We wove the sensors into a knee-stabilizer (see Figure 6.4a) that offered extensive contact with the joints aiding firm movements. A single unpoled filament sewn into the knee support detected and distinguished joint movements. We studied the response of the sensor during dynamic activities while cycling (Figure 6.4b) which is a combination of the continuous form of the two static motions described in SI (see Section 6.6 in Supplementary

Information). The voltage response curve is a resultant of the affect of the motion of all the parts: hip, knee and ankle.[31] The origin of the system is taken when the leg is fully stretched. The superposed red curve over the pictures corresponds to the ankle-motion in Cartesian coordinates. A and B are the points at which the thigh forms a right angle with the calf. The first positive peak in the piezoelectric response curve (Figure 6.4c) corresponds to the bending of the leg behind the knee making a right angle. The negative peak occurs when the leg comes in the forward position and the thigh is parallel to the ground making the second right angle. Our sensor accurately detected the cycling frequency and the response is in complete accordance with the angular velocity (see Figure 6.4c). The small lag seen in the signals is mostly due to the lower sampling frequency of the video recording (59.9 fps) as compared with the voltage acquisition (2000 Hz). The noisy peaks in the voltage signal can be attributed to wrinkling of the filaments which are not

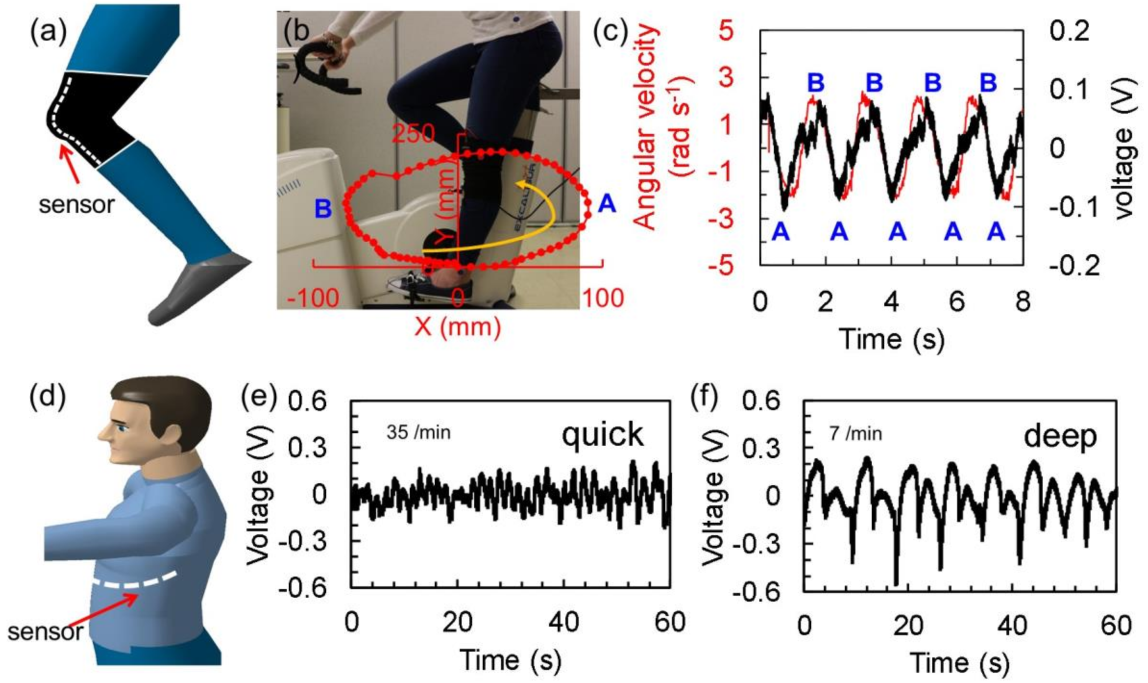

Figure 6.4: a) Schematic depicting the sensor sewn on a knee-stabilizer; b) photograph of the cycling test: red plot shows the path of the ankle during cycling as extracted from the video frames and the yellow arrow shows the cycling direction; c) plot of angular velocity obtained from the recorded video and voltage output of the sensor during cycling; d) schematic of the piezo thread woven into a T-shirt; breathing sensor output during e) shallow/quick breathing, and f) deep/slow breathing for 1 min

well supported as compared to those printed directly on the wings. The variation of maximum voltage in each cycle with the cycling rate (Supplementary Figure 6.7) for two different set of tests (Figure 6.4c and another cycle not shown here) ascertains that higher the cycling speed larger will be the voltage obtained from the sensor.

After studying the sensors for large-scale motion, we studied their sensitivity to detect small-scale motion as in respiration. Respiration is a physiological phenomenon involving the expansion of the chest cavity during inhalation, and its contraction during exhalation forming one respiration cycle. For normal breathing at rest, the respiration rate is around 12-20 cycles per min[32]. A sensor sewn into a t-shirt on the side of the thorax, normal to the axillary lines (see Figure 6.4d), tracked the breathing rhythm of the wearer. During breathing tests the amplitude of the voltage response from the sensor (see Figure 6.4e and f) corresponded to the breathing volume while the frequency to the respiration rate. The breathing sensor y measured respiration rates very well (see Supplementary Table 6.1 and 6.2). The sensor aided in differentiating between the types of breathing (see Figure 6.4e and 6.4f): slow or fast, and shallow or deep based on the frequency and amplitude of the voltage, respectively.

In conclusion, we demonstrated a novel technique to form ready to use piezoelectric sensors with their electrodes in a single step. Our piezoelectric sensors successfully detect the frequency and the generated voltage is linearly proportional to the applied strain. Sensors determining the speed of the motion and distinguishing one movement from the other when directly woven into the clothing are convenient and comfortable to wear and wash without adversely affect the skin. Additional piezoelectric filaments embedded in the textiles could act as a power source to the attached electronics [9] avoiding batteries and entangling wires.[13] Our technique demonstrates the feasibility of a multi-material printing approach where the structure and the sensor could be printed in a single facility at the same time. 3D printability of these sensors would allow conformability to various automobile and aerospace components for structural health monitoring. The process promises potential towards a series of other set of materials and applications that benefit from coextrusion.[33]

6.2 Methods

Materials: Preparation of PVDF/$BaTiO_3$ nanocomposite: A mixture of 0.31 g of $BaTiO_3$ nanoparticles (10 wt.%, 99.9 % purity, 100 nm; Nanostructured & Amorphous materials Inc.) and 3.1 g of PVDF (Sigma Aldrich) was ball-milled (1080 cycles per min; SPEX SamplePrep™ 8000 Series Mixer/Mill™) with 4 mL dimethyl formamide (DMF, Alfa Aesar), 6 mL acetone (BDH) and 0.6 mL (DMSO, Sigma Aldrich) for 20 min. Silver print conductive liquid paint (0.2 Ohm x mil resistivity; MG Chemicals) formed the electrodes.

Printing: The piezoelectric and the silver inks were loaded into 3 mL syringe barrels (see Figure 6.1a-d). The syringe barrels were then placed into a pneumatically operated dispensing system (HP-7X, EFD) to apply precise pressures (0.1 – 4.0 MPa) to coextrude the filaments through tapered nozzles (diameter, d = 410 µm – 1.6 mm). Piezoelectric threads were coextruded using a 840 µm nozzle at about 0.1– 0.15 MPa extrusion pressures (P). Structure geometries in the form of Cartesian coordinates and print speeds were transferred to a robotic dispensing system (I&J2200-4, I&J Fisnar Inc.) via an interfacing software (JR points for dispensing, Janome Sewing Machine). We used a 840 µm nozzle to print all the structures. Vertical pillars and seal whiskers were printed at P = 0.04 MPa and gradually increasing stage speeds (v) from 2 – 4 mm s^{-1}. Piezoelectric strain sensors were printed on FDM (FDM details in SI) printed wings with P = 0.08 – 0.12 MPa and v = 35 mm s^{-1}. Conformal sensors were printed with P = 60 kPa and v = 10 mm $s^{-1}$and spanning filaments with P = 150 kPa and v = 20 mm s^{-1}.

Characterization: A rotational rheometer (Anton Parr, Physica MCR 501) provided the variation of viscosity versus shear rate for both the piezoelectric and silver inks. We used a rough concentric cylindrical geometry (CC 55) with a shear ramp rate of 0.1 s^{-1}. Oil poured on the top of the inks during the tests prevented solvent evaporation. Solvent evaporation tests were conducted by printing 10 mm long filaments with the inks (d = 840 µm; P = 40 kPa; v = 1 mm s^{-1}). A balance (Gh-200, A & D) integrated with a recording software (RsCom Version 5.11, A &D Company, limited) was used to monitor the weight of the filaments for 6 h (sampling frequency = 5 Hz). Final weight of the filaments post complete evaporation of the solvents was recorded after 24 h. The results (Figure 6.2b) are the average of volumetric shrinkage in three samples for each ink. Optical microscopy (BX-61 Olympus; Image-Pro plus V5 an image processing software from Media Cybernetics) permitted the measurement of the thickness and morphology of the filaments and 3D printed structures. A field emission scanning electron microscope (FE-SEM; JEOL JSM-7600TFE) with a low angle back-scattered electron detector obtained high contrast images of the coextruded filament cross-section. Uniaxial tensile tests (Insight electromechanical testing machine), performed at a strain rate = 48 mm min^{-1} with distance between the grips = 20 mm using a 5 N load cell according to ASTM D3822 standard evaluated the Young's moduli, strength and strain at break of the filaments. The reported values are an average of five successful samples (diameter ~500 µm) tested until failure. To determine the piezoelectric properties, we measured the piezoelectric response from the filaments (distance between the grips = 12-15 mm, 3 samples) using a dynamic mechanical analyzer (DMA Q800, TA Instruments) in multi-strain mode (1 % strain, 2 Hz; preload of 0.1 N) for 5 min each.

Data acquisition: For all the sensors, we attached copper tape (3M Canada) at the ends of the piezoelectric thread to form an interface for charge collection. Charges collected from the sensors were converted into readable voltages using a charge amplifier (Measurement Specialties) with an NI-9239 data acquisition system attached to a USB carrier NI-9162 (National Instruments) and recorded using a LabVIEW interface.

Sensor for aero-elastic monitoring: Sensors were coextruded and 3D printed with electrodes on top of a FDM printed insect wing in the shape of a strain gauge (Figure 4a). We screwed the wing on an electromagnetic shaker (The Mode Shop Inc. Model K2007E01). A waveform generator (TE GAM, Model 2720), excited the shaker with input voltage (0.02 to 0.12 V) in the frequency range (0.2 to 20 Hz). A copper mesh covered the entire test set up for electro-magnetic shielding. Mechanical perturbations to the wing were made by hitting it with a slender object. Gusts were simulated using a hair dryer (Revlon, Ionic ceramic), at its highest speed, held vertically above the wing.

Wearable sensors: Piezoelectric filaments were woven into a clinical elastic knee stabilizer (see Figure 6.3a) (Formedica®). A commercial freeware, Kinovea (0.8.15), extracted motion data from the recorded videos (60 fps; Canon EOS Rebel T4i) for comparison with the response from our piezoelectric sensors during the static tests. In case of cycling, Image J was used to track the motion and determine the angular frequency. Motion extraction details are provided in the SI. Cycling tests were performed on a clinical bike (Sport Excaliber, Lode BV Medical Technology) at a mechanical power of 80 W. To monitor respiration, we wove the thread into a tight t-shirt on the left side of the thoracic cavity, parallel to the ribs (see Figure 6.4d). Conducting threads embroidered into the t-shirt formed the electrical connections from the sensor to avoid any noise from moving wires. We tested for two breathing types at rest: quick/shallow and slow/deep.

6.3 Acknowledgements

The authors acknowledge the financial support from NSERC (Natural Sciences and Engineering Research Council of Canada, #RGPIN312568-2013) and Canada Research Chair (#CRC950-216943). The authors thank Prof. Jonathan Tremblay, Kinesiology department, University of Montreal, for the access to the research bike and breathing monitoring equipment and Mr. Nicolas Leduc-Savard for assistance with the logistics. The authors also thank Ms. Isabelle Nowlan, and the Laboratory for Acoustics and Vibration Analysis and the Laboratory for Electrical Energy at Polytechnique Montreal for the electromechanical shaker and the function generator, respectively.

6.4 SEM

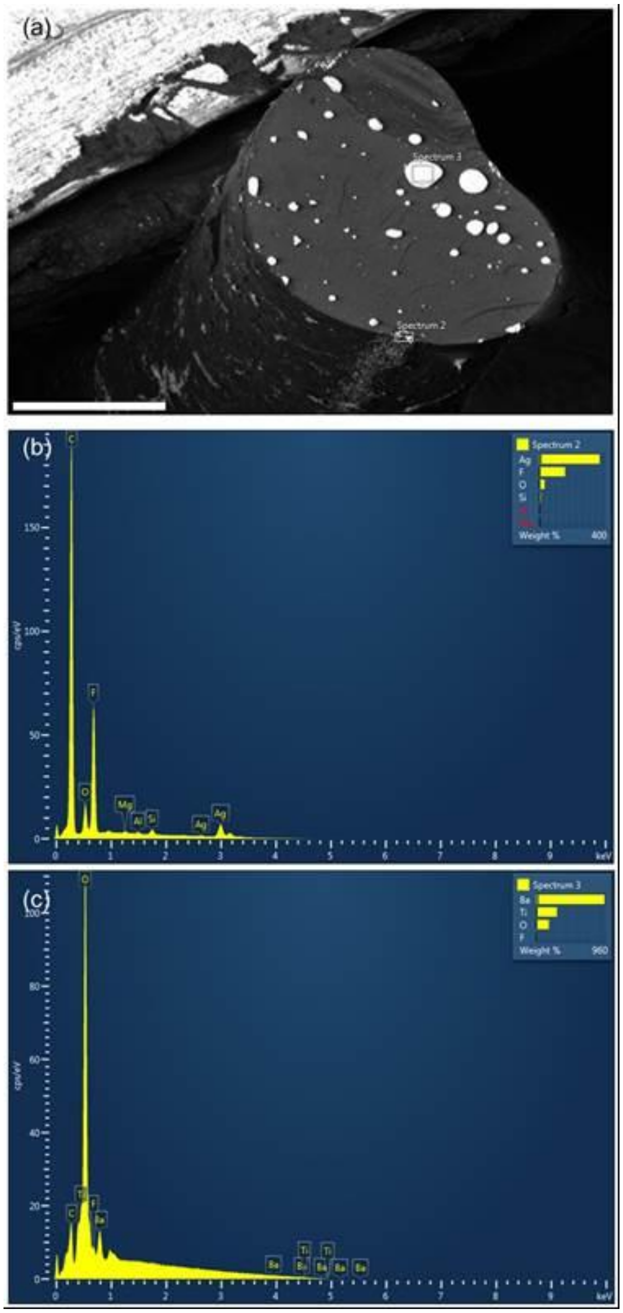

Figure 6.5: (a) SEM image of the cold fractured cross-section of the coextruded filament (scale bar = 250 µm); energy-dispersive spectroscopy (EDS) results for the regions selected in ‘a’: (b) silver region, and (c) $BaTiO_3$ agglomerates

6.5 Vibration tests for the aero-elasticity monitoring sensor

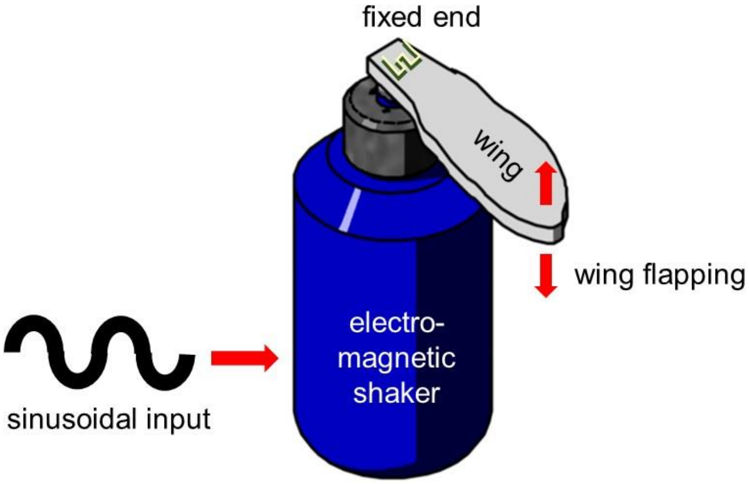

Figure 6.6: Schematic of the FDM printed wing mounted on an electromagnetic shaker and subjected to sinusoidal mechanical input

6.6 Static motion analysis tests

Preliminary tests with the knee-movement sensors involved the wearer raising and lowering the lower limb (from the knee to the foot) both upon sitting and while standing (see Supplementary Figure 6.6a and b). Each exercise was filmed and then, analyzed using Kinovea (0.8.25 x 64) to monitor the movement of the ankle. The software included a motion tracker, that allowed the user to select a specific point in the video and monitor its movement along X and Y axes. The X and Y coordinates could be used to calculate the R values for each movement, R being the displacement of the ankle from the origin (the point at which the leg was at rest). Supplementary Figure 6.6c and d show the comparison of R values of the ankle with the voltage response form the piezoelectric thread for the two tests. The piezoelectric signal of the instrumented knee stabilizer measured as the wearer raised the leg compared well with visual recordings analysed using Kinovea software.

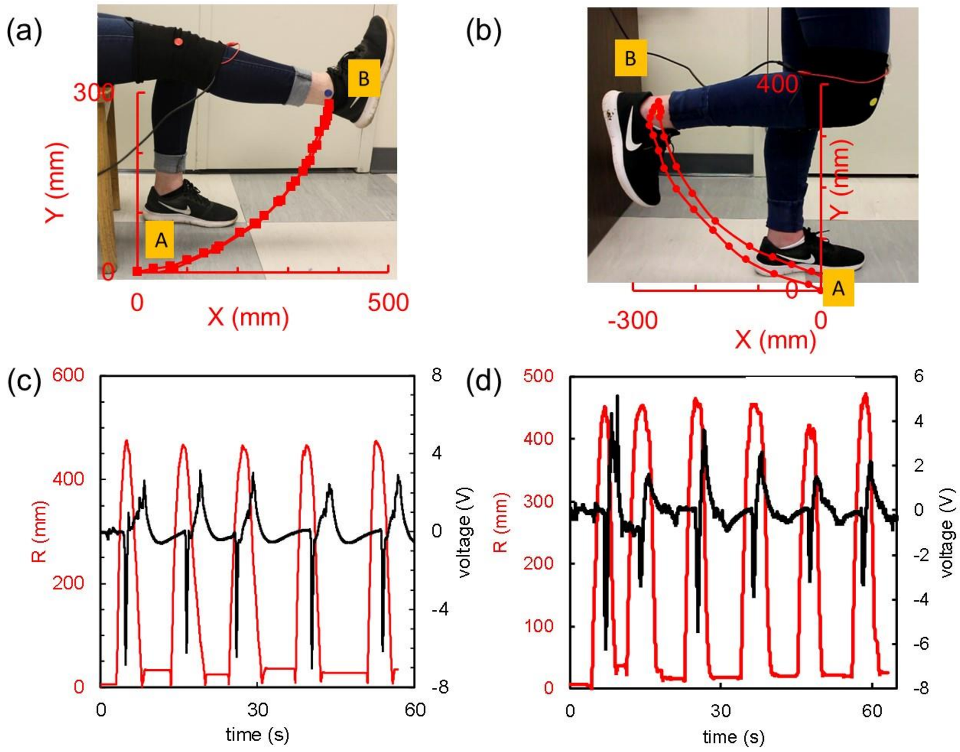

Figure 6.7: Simple leg raising tests (a) sitting and (b) standing. Red plots show the movement of the ankle from its initial to final position. Correlation between the output voltage versus ankle displacement (R) for five consecutive cycles (c) sitting and (d) standing

For the cycling tests, the interior angle at the knee was obtained using Image J (win64), calculated for each frame (processed using MATLAB) from the recorded video (60 fps).

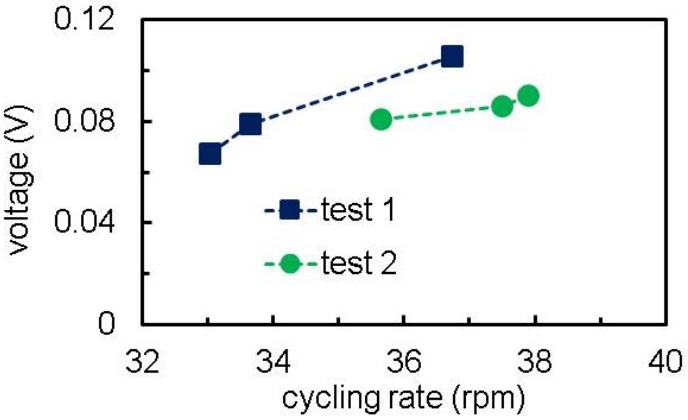

Figure 6.8: Peak voltage output per cycle as a function of cycling rate for 2 separate tests

6.7 Respiration Monitoring

Table 6-1: Number of breaths per minute for quick breathing

Time [min]	Counted	Measured by the sensor
1	30	27
2	25	26
3	31	29
4	34	33
5	31	28

Table 6-2: Number of breaths per minute for deep breathing

Time [min]	Counted	Measured by the sensor
1	6	6
2	7	7
3	7	7
4	6	7
5	7	7

6.8 FDM printed structures

We designed a hemisphere, a U-shaped structure for printing the spanning filaments in Catia V5. We obtained the cicada wing image from stillblog.net. We acquired the geometry of the image using Sketch Tracer tool in Catia V5. We then converted all the part files into .stl files. We used Leapfrog FDM printer to print all the above parts with PLA.

References:

[1] H. Gullapalli, V. S. M. Vemuru, A. Kumar, A. Botello-Mendez, R. Vajtai, M. Terrones, *et al.*, "Flexible Piezoelectric ZnO–Paper Nanocomposite Strain Sensor," *Small,* vol. 6, pp. 1641-1646, 2010.

[2] D. Y. Park, D. J. Joe, D. H. Kim, H. Park, J. H. Han, C. K. Jeong, *et al.*, "Self-Powered Real-Time Arterial Pulse Monitoring Using Ultrathin Epidermal Piezoelectric Sensors," *Advanced Materials,* pp. 1702308-n/a.

[3] L. Persano, C. Dagdeviren, C. Maruccio, L. De Lorenzis, and D. Pisignano, "Cooperativity in the Enhanced Piezoelectric Response of Polymer Nanowires," *Advanced Materials,* vol. 26, pp. 7574-7580, 2014.

[4] D. Ponnamma, M. M. Chamakh, K. Deshmukh, M. Basheer Ahamed, A. Erturk, P. Sharma, *et al.*, "Ceramic-Based Polymer Nanocomposites as Piezoelectric Materials," in *Smart Polymer Nanocomposites: Energy Harvesting, Self-Healing and Shape Memory Applications*, D. Ponnamma, K. K. Sadasivuni, J.-J. Cabibihan, and M. A.-A. Al-Maadeed, Eds., ed Cham: Springer International Publishing, 2017, pp. 77-93.

[5] H. Wu, Y. Huang, F. Xu, Y. Duan, and Z. Yin, "Energy Harvesters for Wearable and Stretchable Electronics: From Flexibility to Stretchability," *Advanced Materials,* vol. 28, pp. 9881-9919, 2016.

[6] C. Dagdeviren, Y. Shi, P. Joe, R. Ghaffari, G. Balooch, K. Usgaonkar, *et al.*, "Conformal piezoelectric systems for clinical and experimental characterization of soft tissue biomechanics," *Nature Materials,* vol. 14, p. 728, 05/18/online 2015.

[7] J. Chang, M. Dommer, C. Chang, and L. Lin, "Piezoelectric nanofibers for energy scavenging applications," *Nano Energy,* vol. 1, pp. 356-371, 5// 2012.

[8] C.-T. Pan, C.-K. Yen, H.-C. Wu, L. Lin, Y.-S. Lu, J. C.-C. Huang, *et al.*, "Significant piezoelectric and energy harvesting enhancement of poly(vinylidene fluoride)/polypeptide

fiber composites prepared through near-field electrospinning," *Journal of Materials Chemistry A*, vol. 3, pp. 6835-6843, 2015.

[9] T. Q. Trung and N.-E. Lee, "Flexible and Stretchable Physical Sensor Integrated Platforms for Wearable Human-Activity Monitoringand Personal Healthcare," *Advanced Materials*, vol. 28, pp. 4338-4372, 2016.

[10] Q. Sun, W. Seung, B. J. Kim, S. Seo, S.-W. Kim, and J. H. Cho, "Active Matrix Electronic Skin Strain Sensor Based on Piezopotential-Powered Graphene Transistors," *Advanced Materials*, vol. 27, pp. 3411-3417, 2015.

[11] S. Y. Chung, S. Kim, J.-H. Lee, K. Kim, S.-W. Kim, C.-Y. Kang, *et al.*, "All-Solution-Processed Flexible Thin Film Piezoelectric Nanogenerator," *Advanced Materials*, vol. 24, pp. 6022-6027, 2012.

[12] D. Aidin and V. Jérémie, "Flexible piezoelectric energy harvesting from jaw movements," *Smart Materials and Structures*, vol. 23, p. 105020, 2014.

[13] M. Lee, C.-Y. Chen, S. Wang, S. N. Cha, Y. J. Park, J. M. Kim, *et al.*, "A Hybrid Piezoelectric Structure for Wearable Nanogenerators," *Advanced Materials*, vol. 24, pp. 1759-1764, 2012.

[14] F. Li, W. Liu, C. Stefanini, X. Fu, and P. Dario, "A Novel Bioinspired PVDF Micro/Nano Hair Receptor for a Robot Sensing System," *Sensors*, vol. 10, p. 994, 2010.

[15] S. Chen, J. Lach, B. Lo, and G. Z. Yang, "Toward Pervasive Gait Analysis With Wearable Sensors: A Systematic Review," *IEEE Journal of Biomedical and Health Informatics*, vol. 20, pp. 1521-1537, 2016.

[16] V. Koncar, "1 - Introduction to smart textiles and their applications," in *Smart Textiles and their Applications*, ed Oxford: Woodhead Publishing, 2016, pp. 1-8.

[17] L. Beker, A. Benet, A. T. Meybodi, B. Eovino, A. P. Pisano, and L. Lin, "Energy harvesting from cerebrospinal fluid pressure fluctuations for self-powered neural implants," *Biomedical Microdevices*, vol. 19, p. 32, 2017.

[18] G. Y. Bae, S. W. Pak, D. Kim, G. Lee, D. H. Kim, Y. Chung, *et al.*, "Linearly and Highly Pressure-Sensitive Electronic Skin Based on a Bioinspired Hierarchical Structural Array," *Advanced Materials*, vol. 28, pp. 5300-5306, 2016.

[19] F. Lorussi, W. Rocchia, E. P. Scilingo, A. Tognetti, and D. D. Rossi, "Wearable, redundant fabric-based sensor arrays for reconstruction of body segment posture," *IEEE Sensors Journal,* vol. 4, pp. 807-818, 2004.

[20] C. Mattmann, F. Clemens, and G. Tröster, "Sensor for Measuring Strain in Textile," *Sensors,* vol. 8, p. 3719, 2008.

[21] J.-Y. Sun, C. Keplinger, G. M. Whitesides, and Z. Suo, "Ionic skin," *Advanced Materials,* vol. 26, pp. 7608-7614, 2014.

[22] R. Li, Y. Si, Z. Zhu, Y. Guo, Y. Zhang, N. Pan, *et al.*, "Supercapacitive Iontronic Nanofabric Sensing," *Advanced Materials*, pp. 1700253-n/a.

[23] Y.-K. Fuh, P.-C. Chen, Z.-M. Huang, and H.-C. Ho, "Self-powered sensing elements based on direct-write, highly flexible piezoelectric polymeric nano/microfibers," *Nano Energy,* vol. 11, pp. 671-677, 2015/01/01/ 2015.

[24] M. Stoppa and A. Chiolerio, "Wearable Electronics and Smart Textiles: A Critical Review," *Sensors,* vol. 14, p. 11957, 2014.

[25] K.-I. Park, J. H. Son, G.-T. Hwang, C. K. Jeong, J. Ryu, M. Koo*, et al.*, "Highly-Efficient, Flexible Piezoelectric PZT Thin Film Nanogenerator on Plastic Substrates," *Advanced Materials,* vol. 26, pp. 2514-2520, 2014.

[26] K.-I. Park, M. Lee, Y. Liu, S. Moon, G.-T. Hwang, G. Zhu, *et al.*, "Flexible Nanocomposite Generator Made of BaTiO3 Nanoparticles and Graphitic Carbons," *Advanced Materials,* vol. 24, pp. 2999-3004, 2012.

[27] S. Bodkhe, G. Turcot, F. P. Gosselin, and D. Therriault, "One-Step Solvent Evaporation-Assisted 3D Printing of Piezoelectric PVDF Nanocomposite Structures," *Acs Applied Materials & Interfaces,* vol. 9, pp. 20833-20842, Jun 21 2017.

[28] J. P. Chown and J. M. Healey, "Gel toothpastes," ed: Google Patents, 1976.

[29] D. Therriault, R. F. Shepherd, S. R. White, and J. A. Lewis, "Fugitive Inks for Direct-Write Assembly of Three-Dimensional Microvascular Networks," *Advanced Materials,* vol. 17, pp. 395-399, 2005.

[30] J. Dooley, "Determining the Processability of Multilayer Coextruded Structures," in *PLACE Conference*, St. Louis, MO, 2007.

[31] (12th September). *Q4E Case Study 6 – Cycle Ergometer*. Available: http://www.quintic.com/education/case_studies/cycle_ergometer.html

[32] K. Subrata Kumar, K. Shinya, and S. Minoru, "A Wearable Capacitive Sensor for Monitoring Human Respiratory Rate," *Japanese Journal of Applied Physics*, vol. 52, p. 04CL05, 2013.

[33] P. Mistry, A. Aied, M. Alexander, K. Shakesheff, A. Bennett, and J. Yang, "Bioprinting Using Mechanically Robust Core–Shell Cell-Laden Hydrogel Strands," *Macromolecular Bioscience*, vol. 17, pp. 1600472-n/a, 2017.

CHAPTER 7 GENERAL DISCUSSION

Additive manufacturing (AM) has come a long way, from being just a rapid prototyping technique to one of the mainstream manufacturing options. Today, we find the applications of 3D printing in almost all fields: aerospace, automobile, biomedicine, sports, electronics, prostheses and many more. As 3D printing can fabricate a component with any form and shape, there is a growing demand to add functionality to the printed structures. It is thus imperative to develop more and more functional materials for the 3D printing industry. There is a great impetus to introduce conductive, magnetic, thermal, piezoelectric, biocompatible properties into printing materials, and can be realized via appropriate nanoparticle addition.

3D printing provides the freedom in structural optimization that has otherwise been difficult with conventional fabrication techniques, thus reducing the number of parts and assembly requirements. Feasibility of multi-material 3D printing then combines structural materials with functional materials to result in smart structures.

Piezoelectric sensors are known for their self-powering properties. Governed by linear electromechanical conversion and high operational bandwidth, piezoelectric materials serve well as integrated sensors and can be used in remote locations as they do not rely on batteries for their functioning. Furthermore, piezoelectric polymers not only overcome the limitations of brittle ceramics but their nanocomposites fair comparatively well in the piezoelectric properties with their ceramic counterparts in sensing applications.

The hybridization of multi-material 3D printing with piezoelectric nanocomposites would result in a whole new demographic of smart structures. Integrated sensors could be applied for real-time monitoring of prosthetics, and biomedical devices. The aerospace, automotive and robotics industry could benefit from customized and embedded sensors by saving on interface materials and wiring.

3D printing of piezoelectric materials has so far been carried out by DW of ceramics, FDM and NFES of PVDF and SLA printing of photocurable polymers containing piezoelectric nanoparticles. Amongst these, NFES and SLA provide very high resolutions. NFES further results in multi-layer structures. But all these techniques entail a high voltage poling step, sometimes at elevated temperatures, to orient the internal dipoles to result in enhanced piezoelectric properties. This becomes a hindrance in multi-material printing, where the substrate or surrounding materials properties could be adversely affected by the high electric fields or high temperatures. The formation of electrodes on these 3D printed piezoelectric surfaces also adds up to the complexity of the fabrication process.

The goal of this thesis was to develop a single step process to form 3D piezoelectric sensors with inherent piezoelectric properties and electrodes thereby overcoming the challenges of poling and electrode deposition. A nanocomposite of PVDF with barium titanate ($BaTiO_3$) nanoparticles was developed to achieve the desired ink with DMF and acetone for the solvent evaporation-assisted 3D printing process. Acetone was preferred over more volatile solvents like chloroform or tetrahydrofuran, because of the latter's toxicity. Rapidly evaporating solvents provided the rigidity for shape retention. 3D printing as well as addition of NPs resulted in increased β-phase content in PVDF. DSC results also confirmed that the crystallinity in the 3D printed films was around 40% and was unaffected with the applied pressures. Rigorous optimization of the nanoparticle concentration in the polymer matrix, as well as mixing methods resulted in a piezoelectric material that when extruded at high pressures of around 1 MPa resulted in a d_{31} constant of 18 pC N^{-1}. This value is comparable to the commercially available poled PVDF films (23 pC N^{-1}). This shear stress induced mechanical orientation of the polymeric dipoles as opposed to electrical orientation is innately compatible with the multi-material printing process. The sensors are functional up to a temperature of 60 °C and within a strain of 5%.

Wherever possible, the piezoelectric performance of the sensors could be augmented via application of electric fields simultaneously while printing. It was found that the piezoelectric polarization improved 300% upon addition of nanoparticles to PVDF and application of an electric field of 1 MV m^{-1} during printing. The improvement upon the application of 1 MV m^{-1} electric field to the nanocomposite improved the polarization by 200%. Electrically poled sensors were also fabricated on shoe-insoles for gait monitoring.

Formation of electrodes simultaneously with the piezoelectric material further reduces the number of steps in the fabrication process. Such a fabrication of the sensor "package" was achieved by coextruding silver paint with the piezoelectric ink. This hybrid material system prints freeforms to spanning filaments, on flat as well as curved surfaces.

The coextruded filaments could directly be used in the form of thread-like sensors for wearable electronics. The sensors were applied to measure respiration and joint-movements. The ability to add functionality to a single filament over an entire fabric helps selectively place the filaments at the location of interest. The filaments produced in this work can endure machine wash. Additional filaments can always be woven to harness energy from the bodily motions to power the auxiliary electronics. Development in the wireless electronics towards data acquisition, storage and transmission would render the entire process compact and portable. The active sensors with fewer components could be integrated into new or existing technologies, moving closer to a battery-free, low-maintenance world. The silver to nanocomposite adhesion further depends on the applied strain, number of cycles performed and the storage conditions of the sensors.

Sensors could be directly printed on the surfaces to be sensed or embedded inside various components. Integrated sensors were fabricated on miniature wings to monitor their aero-elastic performance during flapping. The sensors developed in this work basically function in tension and compression modes. Efforts were made to design whisker-like sensors for flow monitoring. The limitation of size not only complicated the fabrication but also resulted in much lower sensitivity. Once these limitations are overcome with improved design configurations, potential applications can be envisioned in air and water-borne unmanned vehicles as well as robotics.

The developed material system, integrated electrode fabrication process (i.e., co-extrusion) and in-situ poling functionality is easily adaptable to any multi-material printing system. The work serves as an essential tool where customization is of prime interest as well as part type to number is ratio is very small, for example sensors for medical prostheses.

CHAPTER 8 CONCLUSION AND RECOMMENDATIONS

8.1 Conclusions

Solvent evaporation-assisted 3D printing was applied to fabricate piezoelectric structures of PVDF and its nanocomposites containing barium titanate nanoparticles ($BaTiO_3$ NPs). The effects of PVDF concentration, nanofiller type, nanofiller concentration, mixing techniques, printing parameters (applied pressure, and moving stage velocities) on printability as well as piezoelectricity in PVDF were studied. Applications in the form of sensors for contact detection, aero-elasticity, and wearable physiological monitoring are presented. Below are the conclusions drawn from this thesis work:

PVDF solutions in a solvent mixture of acetone and dimethyl formamide (0.15 – 0.275 g mL^{-1}) were studied for their printability. It was found that the piezoelectric β-phase increased with extrusion pressures until 1 MPa. Beyond this limit there was no change in the relative content of β-phase in the printed films.

Fillers like multi-walled carbon nanotubes (MWCNTs) and $BaTiO_3$ NPs were investigated for improving the intrinsic piezoelectric properties in PVDF. Ultra-low density of MWCNTs limited the amount (15 wt.%) in which they could be added, contrastingly the high density of $BaTiO_3$ NPs allowed to add up to 60 wt.% fillers to PVDF. $BaTiO_3$ NPs weight percentages from 1 to 60 % (1, 2, 3, 4, 5, 10, 15, 20, 40 and 60) were investigated. Addition and blending of $BaTiO_3$ NPs into the PVDF solution was carried out by three mixing techniques: ball-milling, extrusion, and sonication. It was found that ball-milling of $BaTiO_3$ NPs with PVDF solution resulted in mechanical activation of the nanoparticles creating active binding sites on their surfaces for the polymer chains of PVDF to attach. Extrusion of this solution at high shear stresses (extrusion pressure ~1 MPa) resulted in mechanical orientation of the dipoles perpendicular to the print directions. This also resulted in the formation of β-phase, the most polar phase of PVDF. The reversion of β-phase into more thermodynamically stable α-phase was in turn arrested by the micron-sized agglomerates of the nanoparticles uniformly distributed in the PVDF matrix. 10 wt.% $BaTiO_3$ NPs resulted in the highest piezoelectric constant as deduced from indigenously designed piezoelectric tests. A d_{31} constant of 18 pC N^{-1} was obtained for the nanocomposites of PVDF with 10 wt.% $BaTiO_3$ NPs prepared via ball-milling. The addition of $BaTiO_3$ NPs resulted in only the enhancement of β-phase in PVDF but did not provide any additional benefit from the piezoelectricity of the NPs because the d_{31} constant of the NPs possess opposite sign as compared to that of PVDF. Moreover, being a ceramic piezoelectric material, the achievement of its piezoelectric behavior necessitates the use of electrical poling, which we wanted to circumvent in this technique. A concentration of 0.2 g mL^{-1} was found to be appropriate to make continuous films, 0.25 g mL^{-1} for fabricating 2.5D layer-by-layer structures and 0.3 g mL^{-1} for fabricating self-supported scaffolds. The feasibility of forming ready-to-use sensors was demonstrated via a 70-layer cylindrical contact sensor detecting finger taps. The electrodes until this step were hand-painted on the sensors.

The effect of applying an electrical voltage while printing the sensors was studied by applying electric fields (0.1 – 1 MV m^{-1}) between the metallic nozzle and a metallic substrate. It was found that poling voltages significantly increased the piezoelectric properties. Applications of this technique were presented in the form of sensors printed on a shoe insole. The sensors well distinguished between walking and stamping motions.

Coextrusion printing was first developed for organic inks. It was then applied to nanocomposites of PVDF with multi-walled carbon nanotubes and the piezoelectric inks. The necessity to increase the MWCNT concentration to achieve the required conductivity resulted in increased viscosity of the inks and finally in highly brittle printed structures. This material system was thus abandoned.

The fabrication process was upgraded into a single-step process by coextruding silver ink along with the piezoelectric nanocomposite during the printing process itself. It was observed that uniform and continuous coating of silver on the edges of the nanocomposite was obtained only when the viscosity of silver was lower than that of the nanocomposite. Another important aspect to be considered was that the two inks possessed a similar rheological behavior. Freestanding pillars, conformal structures and spanning filaments were fabricated from the above mentioned process. Applications of these sensors in monitoring aero-elasticity and as wearable sensors were presented. The sensors when printed on model wings (printed by FDM) captured very well the changes in frequency, input forces, any flow or mechanical perturbations. Wearable sensors were formed by collecting the extruded filaments. The filaments were then woven into joint stabilizers and t-shirts to monitor joints and respiration, respectively. The sensors clearly differentiated between various motions as well as types of breathing.

The processes for the fabrication of one-step piezoelectric sensors developed in this work provides a means to fabricate integrated or embedded, customized sensors for applications in domains ranging from aerospace to healthcare. This process, having reduced the fabrication steps to a minimum, can be easily adapted to industry-scale manufacturing.

8.2 Recommendations

Recommendations for future work are presented below:

1) The effect of other printing parameters such as nozzle diameter, size of the printed part on the piezoelectric properties of the sensors should be evaluated.
2) Other fillers like TiO_2 could be incorporated into PVDF to study their effect on the piezoelectric properties of PVDF via the processes developed in this work.
3) The following parameters should be investigated in detail: accuracy, precision, specific resolution, drift, repeatability as well as reproducibility of the sensors fabricated via the techniques developed in this work.
4) Deconvolution analysis can be performed on the XRD patterns obtained for various films fabricated in this work in order to measure the fraction of each phase.
5) Preparing a piezoelectric material whose piezoelectric properties are not affected by the extrusion temperatures could be developed to adapt the same system to FDM technology.
6) Modeling and simulation using tools like ANSYS or COMSOL should be carried out to develop a platform in which a 3D piezoelectric structure can be designed pertinent to varied applications.
7) Poling-assisted printing should be attempted with the coextrusion system as well applied to the FDM processs to increase the electromechanical conversion efficiency of the printed 3D sensors. Effect of voltages higher than 1 MV m^{-1} on the piezoelectric properties should be studied to further improve the alignment of β-chains.

8) Sensors considered in this work were mostly applied in tension/compression modes. Designs catering to bending and shear deformations should be considered as well.
9) The optimum conductivity required for the charge collectors coextruded with the piezoelectric material must be determined. This should be followed by the optimization of the electrode size with respect to the piezoelectric structure to develop a mass as well as cost efficient design.
10) The amount of power consumed by the electronics used for charge to voltage conversion as well as transmission of the collected charges should be carried out and compared with the power requirements of the resistive and capacitive sensors.
11) 3D printing of other advanced smart materials for example, thermoelectric, triboelectric etc. should be attempted.

BIBLIOGRAPHY

[1] F. N. Gallego-Perez D, Higuita-Castro N, Hansford DJ, "Versatile methods for the fabrication of polyvinylidene fluoride microstructures," *Biomed Microdevices,* vol. 12, p. 9, 2010 Dec 2010.

[2] V. F. a. R. Cardoso, José Gerardo V. Rocha and Soares, Filomena O. and Minas, Graça Maria Henriques and Lanceros-Mendez, Senentxu, "Ultrasonic Transducer Based on β-PVDF for Fluidic Microagitation in a Lab-on-a-Chip Device," *Advances in Science and Technology,* vol. 57, pp. 99-104, 2008.

[3] J. T. Chaitanya Chandrana , Tao Pan, Shuvo Roy and Aaron Fleischman, "Design and Analysis of MEMS Based PVDF Ultrasonic Transducers for Vascular Imaging," *sensors,* vol. 2010, pp. 8740-8750, 21 September 2010 2010.

[4] P. Curie and J. Curie, "Dévelopment, par pression, de l'électricité polaire dans les cristaux hémiè-dres à faces inclinées," *C. R. Acad. Sci,* vol. 91, pp. 294-295, 1880.

[5] H. Kawai, "The Piezoelectricity of Poly (vinylidene Fluoride)," *Japanese Journal of Applied Physics,* vol. 8, p. 2, 1969.

[6] J. Pu, X. Yan, Y. Jiang, C. Chang, and L. Lin, "Piezoelectric actuation of direct-write electrospun fibers," *Sensors and Actuators A: Physical,* vol. 164, pp. 131-136, 11// 2010.

[7] "IEEE Standard on Piezoelectricity," *ANSI/IEEE Std 176-1987,* p. 0_1, 1988.

[8] J. Sirohi and I. Chopra, "Fundamental understanding of piezoelectric strain sensors," 1999, pp. 528-542.

[9] J. B. Lando and W. W. Doll, "The polymorphism of poly(vinylidene fluoride). I. The effect of head-to-head structure," *Journal of Macromolecular Science, Part B,* vol. 2, pp. 205-218, 1968/06/01 1968.

[10] G. M. Sessler, "Piezoelectricity in polyvinylidenefluoride," *The Journal of the Acoustical Society of America,* vol. 70, pp. 1596-1608, 1981.

[11] Y. U. N. Ye, Y. Jiang, Z. Wu, and H. Zeng, "Phase transitions of poly(vinylidine fluoride) under electric fields " *Integrated Ferroelectrics,* vol. 80, pp. 245-251, 2006/11/01 2006.

[12] M. Y. L. Chung, D. C., "Electrical Properties of Polyvinylidene Fluoride Films Prepared by the High Electric Field Applying Method," *Journal of the Korean Physical Society,* vol. 38, p. 6, 2001.

[13] K. Seok Ju, P. Youn Jung, J. Sung, P. S. Jo, P. Cheolmin, K. J. Kim, *et al.*, "Spin cast ferroelectric beta poly(vinylidene fluoride) thin films via rapid thermal annealing," *Applied Physics Letters,* vol. 92, pp. 012921-012921-3, 2008.

[14] S. A. Theron, E. Zussman, and A. L. Yarin, "Experimental investigation of the governing parameters in the electrospinning of polymer solutions," *Polymer,* vol. 45, pp. 2017-2030, 3// 2004.

[15] W. A. Yee, M. Kotaki, Y. Liu, and X. Lu, "Morphology, polymorphism behavior and molecular orientation of electrospun poly(vinylidene fluoride) fibers," *Polymer,* vol. 48, pp. 512-521, 1/12/ 2007.

[16] Y. Liu, J. Yu, X. Wang, and X. Chen, "Effects of Drawing Temperature on Phase Transition in Poly(Vinylidene Fluoride) Films," *Ferroelectrics,* vol. 273, pp. 3-8, 2002/01/01 2002.

[17] A. Omar, "Processing, morphology and product parameters of PVDF filaments for biomedical applications " Masterarbeit, Fakultät für Maschinenwesen, Rheinisch - Westfälische Technische Hochschule, Aachen, 2008.

[18] N. K. Kim, R. J. T. Lin, S. Fakirov, K. Aw, and D. Bhattacharyya, "Nanofibrillar Poly(vinylidene fluoride): Preparation and Functional Properties," *International Journal of Polymeric Materials and Polymeric Biomaterials,* vol. 63, pp. 23-32, 2014/01/04 2013.

[19] Q.-Y. Peng, P.-H. Cong, X.-J. Liu, T.-X. Liu, S. Huang, and T.-S. Li, "The preparation of PVDF/clay nanocomposites and the investigation of their tribological properties," *Wear,* vol. 266, pp. 713-720, 3/25/ 2009.

[20] J. Wang, D. Wu, X. Li, and M. Zhang, "Rheological and electrical properties of carbon black-based poly(vinylidene fluoride) composites," *Polymer Engineering & Science,* vol. 53, pp. 2541-2548, 2013.

[21] W. Yu, Z. Zhao, W. Zheng, Y. Song, B. Li, B. Long, *et al.*, "Structural characteristics of poly(vinylidene fluoride)/clay nanocomposites," *Materials Letters,* vol. 62, pp. 747-750, 2/29/ 2008.

[22] P. C. A. Ferreira, H. Carvalho, J. M. Nobrega, V. Sencadas and a. S. Lanceros-Mendez, "Extrusion of poly(vinylidene fluoride) filaments: Effect of the processing conditions and conductive inner core on the electroactive phase content and mechanical properties," *Journal of Polymer Research*, vol. 18, p. 8, 2011.

[23] A. FORMHALS, "PROCESS AND APPARATUS FOR PREPARING ARTIFICIAL THREADS," Germany Patent, October 2, I934, 1934.

[24] A. Frenot and I. S. Chronakis, "Polymer nanofibers assembled by electrospinning," *Current Opinion in Colloid & Interface Science,* vol. 8, pp. 64-75, 3// 2003.

[25] S.-S. Choi, Y. S. Lee, C. W. Joo, S. G. Lee, J. K. Park, and K.-S. Han, "Electrospun PVDF nanofiber web as polymer electrolyte or separator," *Electrochimica Acta,* vol. 50, pp. 339-343, 11/30/ 2004.

[26] A. Takeno, N. Okui, T. Kitoh, M. Muraoka, S. Umemoto, and T. Sakai, "Preparation and electrical properties of γ form poly(vinylidene fluoride) thin film by vapour deposition in the presence of an electric field," *Thin Solid Films,* vol. 202, pp. 213-220, 7/30/ 1991.

[27] J. S. Andrew and D. R. Clarke, "Enhanced Ferroelectric Phase Content of Polyvinylidene Difluoride Fibers with the Addition of Magnetic Nanoparticles," *Langmuir,* vol. 24, pp. 8435-8438, 2008/08/01 2008.

[28] L. T. CHERNEY, "Structure of Taylor cone-jets: limit of low flow rates," *Journal of Fluid Mechanics,* vol. 378, pp. 167-196, 1999.

[29] S. L. Shenoy, W. D. Bates, H. L. Frisch, and G. E. Wnek, "Role of chain entanglements on fiber formation during electrospinning of polymer solutions: good solvent, non-specific polymer–polymer interaction limit," *Polymer,* vol. 46, pp. 3372-3384, 4/25/ 2005.

[30] K. Gao, X. Hu, C. Dai, and T. Yi, "Crystal structures of electrospun PVDF membranes and its separator application for rechargeable lithium metal cells," *Materials Science and Engineering: B,* vol. 131, pp. 100-105, 7/15/ 2006.

[31] S. Koombhongse, W. Liu, and D. H. Reneker, "Flat polymer ribbons and other shapes by electrospinning," *Journal of Polymer Science Part B: Polymer Physics,* vol. 39, pp. 2598-2606, 2001.

[32] D. Sun, C. Chang, S. Li, and L. Lin, "Near-Field Electrospinning," *Nano Letters,* vol. 6, pp. 839-842, 2006/04/01 2006.

[33] Z. H. Liu, C. T. Pan, L. W. Lin, and H. W. Lai, "Piezoelectric properties of PVDF/MWCNT nanofiber using near-field electrospinning," *Sensors and Actuators A: Physical,* vol. 193, pp. 13-24, 4/15/ 2013.

[34] J. Sang-Soo, T. Sharma, L. Youngkyu, B. Gill, and J. X. Zhang, "A thin-film piezoelectric PVDF-TrFE based implantable pressure sensor using lithographic patterning," in *Micro*

Electro Mechanical Systems (MEMS), 2011 IEEE 24th International Conference on, 2011, pp. 644-647.

[35] J. Xu, M. J. Dapino, D. Gallego-Perez, and D. Hansford, "Microphone based on Polyvinylidene Fluoride (PVDF) micro-pillars and patterned electrodes," *Sensors and Actuators A: Physical,* vol. 153, pp. 24-32, 6/25/ 2009.

[36] H. Han, Y. Nakagawa, Y. Takai, K. Kikuchi, S. Tsuchitani, and Y. Kosimoto, "Microstructure fabrication on a β-phase PVDF film by wet and dry etching technology," *Journal of Micromechanics and Microengineering,* vol. 22, p. 085030, 2012.

[37] N. An, H. Liu, Y. Ding, B. Lu, and M. Zhang, "Fabrication of micro-structures on a PVDF/TiO2 nano-composite film using photocatalytic lithography," *Applied Surface Science,* vol. 258, pp. 5052-5055, 4/1/ 2012.

[38] C. Wen-Yang, C. Chun-Hsun, and L. Yu-Cheng, "A Flexible Piezoelectric Sensor for Microfluidic Applications Using Polyvinylidene Fluoride," *Sensors Journal, IEEE,* vol. 8, pp. 495-500, 2008.

[39] J. Shklovsky, L. Engel, Y. Sverdlov, Y. Shacham-Diamand, and S. Krylov, "Nano-imprinting lithography of P(VDF–TrFE–CFE) for flexible freestanding MEMS devices," *Microelectronic Engineering,* vol. 100, pp. 41-46, 12// 2012.

[40] C. Lee and J. A. Tarbutton, "Electric poling-assisted additive manufacturing process for PVDF polymer-based piezoelectric device applications," *Smart Materials and Structures,* vol. 23, p. 095044, 2014.

[41] D. M. Esterly and B. J. Love, "Phase transformation to β-poly(vinylidene fluoride) by milling," *Journal of Polymer Science Part B: Polymer Physics,* vol. 42, pp. 91-97, 2004.

[42] R. Gregorio, "Determination of the α, β, and γ crystalline phases of poly(vinylidene fluoride) films prepared at different conditions," *Journal of Applied Polymer Science,* vol. 100, pp. 3272-3279, 2006.

[43] G. Mago, D. M. Kalyon, and F. T. Fisher, "Membranes of Polyvinylidene Fluoride and PVDF Nanocomposites with Carbon Nanotubes via Immersion Precipitation," *Journal of Nanomaterials,* vol. 2008, 2008.

[44] P. Martins, A. C. Lopes, and S. Lanceros-Mendez, "Electroactive phases of poly(vinylidene fluoride): Determination, processing and applications," *Progress in Polymer Science*, vol. 39, pp. 683–706, 2014.

[45] T. Boccaccio, A. Bottino, G. Capannelli, and P. Piaggio, "Characterization of PVDF membranes by vibrational spectroscopy," *Journal of Membrane Science,* vol. 210, pp. 315-329, 12/15/ 2002.

[46] J. R. Gregorio and M. Cestari, "Effect of crystallization temperature on the crystalline phase content and morphology of poly(vinylidene fluoride)," *Journal of Polymer Science Part B: Polymer Physics,* vol. 32, pp. 859-870, 1994.

[47] "d33 piezometer," P. P. P. Systems, Ed., ed, 2004, p. 4.

[48] S. Kasap, *Principles of Electronic Materials and Devices* 3ed.: McGraw-Hill Science/Engineering/Math, 2005.

[49] A. Salimi and A. A. Yousefi, "Analysis Method: FTIR studies of β-phase crystal formation in stretched PVDF films," *Polymer Testing,* vol. 22, pp. 699-704, 9// 2003.

[50] B. Mohammadi, A. A. Yousefi, and S. M. Bellah, "Effect of tensile strain rate and elongation on crystalline structure and piezoelectric properties of PVDF thin films," *Polymer Testing,* vol. 26, pp. 42-50, 2// 2007.

[51] S. H. Lee and H. H. Cho, "Crystal structure and thermal properties of poly(vinylidene fluoride)-carbon fiber composite films with various drawing temperatures and speeds," *Fibers and Polymers,* vol. 11, pp. 1146-1151, 2010/12/01 2010.

[52] W. Huang, K. Edenzon, L. Fernandez, S. Razmpour, J. Woodburn, and P. Cebe, "Nanocomposites of poly(vinylidene fluoride) with multiwalled carbon nanotubes," *Journal of Applied Polymer Science,* vol. 115, pp. 3238-3248, 2010.

[53] D. R. Dillon, K. K. Tenneti, C. Y. Li, F. K. Ko, I. Sics, and B. S. Hsiao, "On the structure and morphology of polyvinylidene fluoride–nanoclay nanocomposites," *Polymer,* vol. 47, pp. 1678-1688, 2/22/ 2006.

[54] P. S. M. Rajesh, S. Bodkhe, S. Kamle, and V. Verma, "Enhancing beta-phase in PVDF through physicochemical modification of cellulose," *Electronic Materials Letters,* vol. 10, pp. 315-319, 2014/01/01 2014.

[55] X. Jing, X. Shen, H. Song, and F. Song, "Magnetic and dielectric properties of barium ferrite fibers/poly(vinylidene fluoride) composite films," *Journal of Polymer Research,* vol. 18, pp. 2017-2021, 2011/11/01 2011.

[56] M. El Achaby, F.-E. Arrakhiz, S. Vaudreuil, E. M. Essassi, A. Qaiss, and M. Bousmina, "Nanocomposite films of poly(vinylidene fluoride) filled with polyvinylpyrrolidone-

coated multiwalled carbon nanotubes: Enhancement of β-polymorph formation and tensile properties," *Polymer Engineering & Science,* vol. 53, pp. 34-43, 2013.

[57] P. Martins, C. M. Costa, and S. Lanceros-Mendez, "Nucleation of electroactive β-phase poly(vinilidene fluoride) with CoFe2O4 and NiFe2O4 nanofillers: a new method for the preparation of multiferroic nanocomposites," *Applied Physics A,* vol. 103, pp. 233-237, 2011/04/01 2011.

[58] V. Corral-Flores, J. J. Pérez-Herrera, E. Torres-Moye, J. Romero-García, D. Bueno-Baqués, and R. F. Ziolo, "Preparation of Electrospun Barium Titanate – Polyvinylidene Fluoride Piezoelectric Membranes," *Materials Science Forum,* vol. 644, pp. 33-37, 2010.

[59] F. Yiin-Kuen, H. Hsi-Chun, W. Bo-Sheng, and L. Shan-Chien, "All-fiber transparent piezoelectric harvester with a cooperatively enhanced structure," *Nanotechnology,* vol. 27, p. 435403, 2016.

[60] K. K. B. Hon, L. Li, and I. M. Hutchings, "Direct writing technology—Advances and developments," *CIRP Annals - Manufacturing Technology,* vol. 57, pp. 601-620, // 2008.

[61] *http://www.stratasys.com/3d-printers/technologies/fdm-technology*.

[62] J. Yan, K. Chaudhary, S. Chul Bae, J. A. Lewis, and S. Granick, "Colloidal ribbons and rings from Janus magnetic rods," *Nat Commun,* vol. 4, p. 1516, 02/26/online 2013.

[63] J. E. Smay, G. M. Gratson, R. F. Shepherd, J. Cesarano, and J. A. Lewis, "Directed Colloidal Assembly of 3D Periodic Structures," *Advanced Materials,* vol. 14, pp. 1279-1283, 2002.

[64] D. Therriault, R. F. Shepherd, S. R. White, and J. A. Lewis, "Fugitive Inks for Direct-Write Assembly of Three-Dimensional Microvascular Networks," *Advanced Materials,* vol. 17, pp. 395-399, 2005.

[65] B. Y. Ahn, D. J. Lorang, and J. A. Lewis, "Transparent conductive grids via direct writing of silver nanoparticle inks," *Nanoscale,* vol. 3, pp. 2700-2702, 2011.

[66] L. L. Lebel, B. Aissa, M. A. E. Khakani, and D. Therriault, "Ultraviolet-Assisted Direct-Write Fabrication of Carbon Nanotube/Polymer Nanocomposite Microcoils," *Advanced Materials,* vol. 22, pp. 592-596, 2010.

[67] D. Rotman. (2014) Microscale 3-D Printing. *MIT Technology Review*. Available: http://www.technologyreview.com/featuredstory/526521/microscale-3-d-printing/

[68] R. D. Farahani, L. L. Lebel, and D. Therriault, "Processing parameters investigation for the fabrication of self-supported and freeform polymeric microstructures using ultraviolet-assisted three-dimensional printing," *Journal of Micromechanics and Microengineering,* vol. 24, p. 055020, 2014.

[69] S. Z. Guo, F. Gosselin, N. Guerin, A. M. Lanouette, M. C. Heuzey, and D. Therriault, "Solvent-cast three-dimensional printing of multifunctional microsystems," *Small,* vol. 9, pp. 4118-22, Dec 20 2013.

[70] K. Kim, W. Zhu, X. Qu, C. Aaronson, W. R. McCall, S. Chen, *et al.*, "3D Optical Printing of Piezoelectric Nanoparticle–Polymer Composite Materials," *ACS Nano,* vol. 8, pp. 9799-9806, 2014/10/28 2014.

[71] X. Chen, H. Tian, X. Li, J. Shao, Y. Ding, N. An, *et al.*, "A high performance P(VDF-TrFE) nanogenerator with self-connected and vertically integrated fibers by patterned EHD pulling," *Nanoscale,* vol. 7, pp. 11536-11544, 2015.

[72] J. E. Smay, J. Cesarano, B. A. Tuttle, and J. A. Lewis, "Directed Colloidal Assembly of Linear and Annular Lead Zirconate Titanate Arrays," *Journal of the American Ceramic Society,* vol. 87, pp. 293-295, 2004.

[73] C. Lee and J. A. Tarbutton, "Electric Poling-assisted Additive Manufacturing Process for Lead-free Piezoelectric Device Fabrication," *Procedia Manufacturing,* vol. 1, pp. 320-326, 2015/01/01 2015.

[74] E. Suaste-Gómez, G. Rodríguez-Roldán, H. Reyes-Cruz, and O. Terán-Jiménez, "Developing an Ear Prosthesis Fabricated in Polyvinylidene Fluoride by a 3D Printer with Sensory Intrinsic Properties of Pressure and Temperature," *Sensors,* vol. 16, p. 332, 2016.

[75] P. R. Chalker, K. M. Berggreen, A. T. Clare, J. Singh, and C. J. Sutcliffe, "Rapid Prototyping Methodologies for Ceramic Micro Components," 2009, pp. 1-7.

[76] E. Tarasova, I. Juravleva, I. Shishkovsky, and R. Ruzhechko, "Layering laser-assisted sintering of functional graded porous PZT ceramoplasts," *Phase Transitions,* vol. 86, pp. 1121-1129, 2013/11/01 2013.

[77] C. Shuai, W. Huang, P. Feng, C. Gao, X. Shuai, T. Xiao, *et al.*, "Tailoring properties of porous Poly (vinylidene fluoride) scaffold through nano-sized 58s bioactive glass," *Journal of Biomaterials Science, Polymer Edition,* vol. 27, pp. 97-109, 2016/01/02 2016.

[78] Y. Yang, Z. Chen, X. Song, B. Zhu, T. Hsiai, P.-I. Wu, *et al.*, "Three dimensional printing of high dielectric capacitor using projection based stereolithography method," *Nano Energy,* vol. 22, pp. 414-421, 4// 2016.

[79] Z. Chen, X. Song, L. Lei, X. Chen, C. Fei, C. T. Chiu, *et al.*, "3D printing of piezoelectric element for energy focusing and ultrasonic sensing," *Nano Energy,* vol. 27, pp. 78-86, 9// 2016.

[80] S.-Z. Guo, M.-C. Heuzey, and D. Therriault, "Properties of Polylactide Inks for Solvent-Cast Printing of Three-Dimensional Freeform Microstructures," *Langmuir,* vol. 30, pp. 1142-1150, 2014/02/04 2014.

[81] C. K. M. Fung, I. Elhajj, W. J. Li, and X. Ning, "A 2-D PVDF force sensing system for micro-manipulation and micro-assembly," in *Robotics and Automation, 2002. Proceedings. ICRA '02. IEEE International Conference on*, 2002, pp. 1489-1494 vol.2.

[82] S. Faramarzi, A. Ghanbari, X. Q. Chen, and W. H. Wang, "A PVDF Based 3D Force Sensor for Micro and Nano Manipulation," in *IEEE International Conference on Control and Automation*, New Zealand,, 2009.

[83] Y. Jingang and H. Liang, "A PVDF-Based Deformation and Motion Sensor: Modeling and Experiments," *Sensors Journal, IEEE,* vol. 8, pp. 384-391, 2008.

[84] H. Sheng-Wei, W. Jui-yi, L. Hao-hsuan, W. Po-wei, E. Chen, C. Forng-chen, *et al.*, "Development of low cost PVDF pressure sensors for sensing the motion of a robot fish," in *Underwater Technology Symposium (UT), 2013 IEEE International*, 2013, pp. 1-6.

[85] K.-C. Chuang, C.-C. Ma, and H.-C. Liou, "Experimental Investigation of the Cross-Sensitivity and Size Effects of Polyvinylidene Fluoride Film Sensors on Modal Testing," *Sensors,* vol. 12, pp. 16641-16659, 2012.

[86] H. Luo and S. Hanagud, "PVDF Film Sensor and Its Applications in Damage Detection," *Journal of Aerospace Engineering,* vol. 12, pp. 23-30, 1999.

[87] S. Y, G. K, and W. A, "Title," unpublished|.

[88] C. Group. (2014, 7th March). *Intelligent Textiles*. Available: http://www.gcttg.com/en/sectors-materials/intelligent-smart-textiles

[89] M. Stoppa and A. Chiolerio, "Wearable Electronics and Smart Textiles: A Critical Review," *Sensors,* vol. 14, p. 11957, 2014.

[90] A. Brown. (2015, 7th March 2017). *The Past Ten Years in Smart Textiles – The Pros and Cons*. Available: http://www.wearable-technologies.com/2015/12/the-past-ten-years-in-smart-textiles-the-pros-and-cons/

[91] Q. Sun, W. Seung, B. J. Kim, S. Seo, S.-W. Kim, and J. H. Cho, "Active Matrix Electronic Skin Strain Sensor Based on Piezopotential-Powered Graphene Transistors," *Advanced Materials,* vol. 27, pp. 3411-3417, 2015.

[92] P. Slobodian, P. Riha, R. Benlikaya, P. Svoboda, and D. Petras, "A Flexible Multifunctional Sensor Based on Carbon Nanotube/Polyurethane Composite," *IEEE Sensors Journal,* vol. 13, pp. 4045-4048, 2013.

[93] T. Yamada, Y. Hayamizu, Y. Yamamoto, Y. Yomogida, A. Izadi-Najafabadi, D. N. Futaba*, et al.*, "A stretchable carbon nanotube strain sensor for human-motion detection," *Nat Nano,* vol. 6, pp. 296-301, 05//print 2011.

[94] E. Roh, B.-U. Hwang, D. Kim, B.-Y. Kim, and N.-E. Lee, "Stretchable, Transparent, Ultrasensitive, and Patchable Strain Sensor for Human–Machine Interfaces Comprising a Nanohybrid of Carbon Nanotubes and Conductive Elastomers," *ACS Nano,* vol. 9, pp. 6252-6261, 2015/06/23 2015.

[95] J.-H. Kong, N.-S. Jang, S.-H. Kim, and J.-M. Kim, "Simple and rapid micropatterning of conductive carbon composites and its application to elastic strain sensors," *Carbon,* vol. 77, pp. 199-207, 2014/10/01/ 2014.

[96] N. Lu, C. Lu, S. Yang, and J. Rogers, "Highly Sensitive Skin-Mountable Strain Gauges Based Entirely on Elastomers," *Advanced Functional Materials,* vol. 22, pp. 4044-4050, 2012.

[97] S.-H. Bae, Y. Lee, B. K. Sharma, H.-J. Lee, J.-H. Kim, and J.-H. Ahn, "Graphene-based transparent strain sensor," *Carbon,* vol. 51, pp. 236-242, 2013/01/01/ 2013.

[98] Y. Wang, L. Wang, T. Yang, X. Li, X. Zang, M. Zhu*, et al.*, "Wearable and Highly Sensitive Graphene Strain Sensors for Human Motion Monitoring," *Advanced Functional Materials,* vol. 24, pp. 4666-4670, 2014.

[99] C. Yan, J. Wang, W. Kang, M. Cui, X. Wang, C. Y. Foo*, et al.*, "Highly Stretchable Piezoresistive Graphene–Nanocellulose Nanopaper for Strain Sensors," *Advanced Materials,* vol. 26, pp. 2022-2027, 2014.

[100] N. Liu, G. Fang, J. Wan, H. Zhou, H. Long, and X. Zhao, "Electrospun PEDOT:PSS-PVA nanofiber based ultrahigh-strain sensors with controllable electrical conductivity," *Journal of Materials Chemistry,* vol. 21, pp. 18962-18966, 2011.

[101] M. Amjadi, A. Pichitpajongkit, S. Lee, S. Ryu, and I. Park, "Highly Stretchable and Sensitive Strain Sensor Based on Silver Nanowire–Elastomer Nanocomposite," *ACS Nano,* vol. 8, pp. 5154-5163, 2014/05/27 2014.

[102] X. Xiao, L. Yuan, J. Zhong, T. Ding, Y. Liu, Z. Cai*, et al.*, "High-Strain Sensors Based on ZnO Nanowire/Polystyrene Hybridized Flexible Films," *Advanced Materials,* vol. 23, pp. 5440-5444, 2011.

[103] J. Lee, S. Kim, J. Lee, D. Yang, B. C. Park, S. Ryu*, et al.*, "A stretchable strain sensor based on a metal nanoparticle thin film for human motion detection," *Nanoscale,* vol. 6, pp. 11932-11939, 2014.

[104] L. Cai, L. Song, P. Luan, Q. Zhang, N. Zhang, Q. Gao*, et al.*, "Super-stretchable, Transparent Carbon Nanotube-Based Capacitive Strain Sensors for Human Motion Detection," vol. 3, p. 3048, 10/25/online 2013.

[105] S. Yao and Y. Zhu, "Wearable multifunctional sensors using printed stretchable conductors made of silver nanowires," *Nanoscale,* vol. 6, pp. 2345-2352, 2014.

[106] M. Lee, C.-Y. Chen, S. Wang, S. N. Cha, Y. J. Park, J. M. Kim*, et al.*, "A Hybrid Piezoelectric Structure for Wearable Nanogenerators," *Advanced Materials,* vol. 24, pp. 1759-1764, 2012.

[107] Y.-K. Fuh, P.-C. Chen, Z.-M. Huang, and H.-C. Ho, "Self-powered sensing elements based on direct-write, highly flexible piezoelectric polymeric nano/microfibers," *Nano Energy,* vol. 11, pp. 671-677, 2015/01/01/ 2015.

[108] K. Subrata Kumar, K. Shinya, and S. Minoru, "A Wearable Capacitive Sensor for Monitoring Human Respiratory Rate," *Japanese Journal of Applied Physics,* vol. 52, p. 04CL05, 2013.

[109] K.-F. Lei, Y.-Z. Hsieh, Y.-Y. Chiu, and M.-H. Wu, "The Structure Design of Piezoelectric Poly(vinylidene Fluoride) (PVDF) Polymer-Based Sensor Patch for the Respiration Monitoring under Dynamic Walking Conditions," *Sensors,* vol. 15, p. 18801, 2015.

[110] E. Haentzsche, R. Mueller, T. Ruder, A. Nocke, and C. Cherif, "Integrative Manufacturing of Textile-Based Sensors for Spatially Resolved Structural Health Monitoring Tasks of Large-Scaled Composite Components," in *Materials Science Forum*, 2015.

[111] Y. Yu, X. Zhao, Y. Wang, and J. Ou, "A study on PVDF sensor using wireless experimental system for bridge structural local monitoring," *Telecommunication Systems,* vol. 52, pp. 2357-2366, April 01 2013.

[112] M. Kurata, X. Li, K. Fujita, L. He, and M. Yamaguchi, "PVDF piezo film as dynamic strain sensor for local damage detection of steel frame buildings," in *SPIE Smart Structures and Materials + Nondestructive Evaluation and Health Monitoring*, 2013, p. 86920F.

[113] R. Vodicka and S. C. Galea, "Use of PVDF strain sensors for health monitoring of bonded composite patches," DST1998-06 1998.

[114] E. Guzman, J. Cugnoni, T. Gmür, P. Bonhôte, and A. Schorderet, "Survivability of integrated PVDF film sensors to accelerated ageing conditions in aeronautical/aerospace structures," *Smart Materials and Structures,* vol. 22, p. 065020, 2013.

[115] L.-J. Yang, C.-K. Hsu, J.-Y. Ho, and C.-K. Feng, "Flapping wings with PVDF sensors to modify the aerodynamic forces of a micro aerial vehicle," *Sensors and Actuators A: Physical*, vol. 139, pp. 95-103, 2007/09/12/ 2007.

[116] A. Bulletti, P. Giannelli, M. Calzolai, and L. Capineri, "An Integrated Acousto/Ultrasonic Structural Health Monitoring System for Composite Pressure Vessels," *IEEE Transactions on Ultrasonics, Ferroelectrics, and Frequency Control,* vol. 63, pp. 864-873, 2016.

[117] C. Yung-Hang, W. Kan, W. Changsheng, C. Yiwen, Z. Chuck, and W. Ben, "A facile method for integrating direct-write devices into three-dimensional printed parts," *Smart Materials and Structures,* vol. 24, p. 065008, 2015.

[118] X. Yao, C. Luan, D. Zhang, L. Lan, and J. Fu, "Evaluation of carbon fiber-embedded 3D printed structures for strengthening and structural-health monitoring," *Materials & Design,* vol. 114, pp. 424-432, 2017/01/15/ 2017.

[119] M. Q. Le, F. Ganet, D. Audigier, J.-F. Capsal, and P.-J. Cottinet, "Printing of microstructure strain sensor for structural health monitoring," *Applied Physics A*, vol. 123, p. 354, April 17 2017.

[120] H. Kim and S. Priya, "Piezoelectric microgenerator - current status, challenges, and applications," in *Applications of Ferroelectrics, 2008. ISAF 2008. 17th IEEE International Symposium on the*, 2008, pp. 1-2.